UNIVERSITY OF CALIFORNIA

Santa Barbara

Using Remote Sensing to Characterize Disturbance during a Severe Drought in the Sierra Nevada

A dissertation submitted in partial satisfaction of the

requirements for the degree Doctor of Philosophy

in Geography

by

Zachary Trent Tane

Committee in charge:

Professor Dar Roberts, Chair

Professor Stuart Sweeney

Professor Richard Church

Professor Max Moritz

March 2018

The dissertation of Zachary Trent Tane is approved.

_____
Richard Church

_____
Max Moritz

_____
Stuart Sweeney

_____
Dar Roberts, Committee Chair

March 2018

Using Remote Sensing to Characterize Disturbance during a Severe Drought in the Sierra Nevada

by

Zachary Trent Tane

ACKNOWLEDGEMENTS

Alfred North Whitehead wrote, "No one who achieves success does so without the help of others." This was certainly true for my dissertation. The United States Forest Service, in particular the Region-5 Remote Sensing Lab, has been instrumental in this work. In particular, the consistent support and understanding of Carlos Ramirez was essential to this work. Nathan Amboy maintained the computers that much of this research was conducted on, as well as processed the WorldView imagery. Kirk Evans assisted with some python code that was involved in this research, as well the processing of the lidar data, in particular with using the computer program FUSION. Others at the lab who were instrumental in this research include Alexander Koltunov, Tanya Kohler, Laura Young, Rod Hart, and Shengli Huang.

JPL was also essential for this work. In particular, Rob Green, Sarah Lundeen, and all others responsible for processing and making available the AVIRIS data, without which this research could not have occurred. Natasha Stavros also provided a great deal of assistance particularly with regards to work surrounding the Rim Fire.

I would also like to thank Dr. Gregory Asner and Carnegie Science's Asner Lab for providing access to the 2015 California progressive water stress and canopy water content data.

I'm forever grateful to Dar Roberts for being my advisor and seeing me through these four and a half years of graduate school. During this time I have gone from having no idea what AVIRIS was to being able to produce this dissertation, and that would never have happened without Dar. I'm also grateful to my other committee members, Stuart Sweeney, Rick Church, and Max Moritz for supporting me in completing this dissertation. Thanks also

to my undergraduate advisor John Battles who first made me seriously consider the path of a PhD.

Other important influences include Seth Petterson, Keely Roth, Mike Alonzo, Andrew Thrope Susan Meerdink, Alana Ayasse, Sarah Shivers, Minquan Chen, Erin Wetherley, Fernanda Ribeiro, Gabriel Daldegan, and Christopher Kibler. All of whom provided friendship, assistance, and ideas. I'm appreciative of UCSB Geography Department staff, in particular the IT team headed by Dylan Parenti, for the professional and technical assistance provided. Thanks, also to Richard Ko, who performed monotonous and repetitive image analysis without complaint.

I'm forever indebted to my mother, Nancy Drake, my father, Lance Tane, and my brother, Jonah Tane, for the love, support, and making me the person I am today (for better or worse). Finally, I would like to thank Lisa Sanderson whose love helped me stay sane during the composition of this dissertation.

ZACHARY TRENT TANE

Education

Doctor of Philosophy in Geography, University of California, Santa Barbara, June 2002
Bachelor of Science in Forestry and Natural Resources, University of California, Berkeley, May 2009

Professional Employment

2014 – Present: Remote Sensing Analyst, United States Forest Service
2014 – 2018: Graduate Student Researcher, University of California, Santa Barbara
2014 – 2017: Teaching Assistant, University of California, Santa Barbara
2009 – 2014: Forester, United States Forest Service

Publications

Tane, Z., Roberts, D., Koltunov, A., Sweeney, S., & Ramirez, C. (*In press*). A Framework for Detecting Conifer Mortality across an Ecoregion using High Spatial Resolution Spaceborne Imaging Spectroscopy. Remote Sensing and the Environment.

Tane, Z., Roberts, D., Veraverbeke, S., Casas, A., Ramirez, C., & Ustin, S. (2018). Evaluating Endmember and Band Selection Techniques for Multiple Endmember Spectral Mixture Analysis using Post-Fire Imaging Spectroscopy. Remote Sensing, 10, 389.

Tuholske, C., **Tane, Z**., López-Carr, D., Roberts, D., & Cassels, S. (2017). Thirty years of land use/cover change in the Caribbean: Assessing the relationship between urbanization and mangrove loss in Roatán, Honduras. Applied Geography, 88, 84-93.

Stavros, E. N., **Tane, Z**., Kane, V. R., Veraverbeke, S., McGaughey, R. J., Lutz, J. A., ... & Schimel, D. (2016). Unprecedented remote sensing data over King and Rim megafires in the Sierra Nevada Mountains of California. Ecology, 97(11), 3244-3244.

Stavros, E. N., Abatzoglou, J., **Tane, Z**., Kane, V., Veraverbeke, S., McGaughey, B., ... & Ramirez, C. (2014). Regional likelihood of very large wildfires over the 21st century across the western United States: Motivation to study individual events like the Rim Fire, a unique opportunity with unprecedented remote sensing data. In Proc. Large Wildl. Fires Conf. RMRS-P (Vol. 73, pp. 312-313).

Conference Presentations

Tane, Z., Ramirez, C., Roberts, D., Koltunov, A., Sweeney, S. (2016) Using Multi-Temporal Imaging Spectroscopy Data to Detect Drought and Bark Beetle Related Conifer Mortality across the Central Sierra Nevada, California, USA. In, American Geophysical Union Fall Meeting. San Francisco, CA.

Heck, M. D., Roberts, D., Miller, D., **Tane, Z.** (2016) Finding Spectral Patterns in Bark Beetle Infestations in the Sierra National Forest Using Landsat and AVIRIS Imagery. In, American Geophysical Union Fall Meeting. San Francisco, CA.

Tane, Z., Ramirez, C., Roberts, D. (2015) Mutli-temporal Imaging Spectroscopy Analysis for the Identification of Coniferous Forest Mortality Related to Drought Stress in the Central Sierra Nevada, California. In, American Geophysical Union Fall Meeting. San Francisco, CA.

Tane, Z., Roberts, D., Veraverbeke, S., Casas, A., Ramirez, C. Ustin, S. (2014) Using Differenced Hypserspectral Data and Spectra Mixture Analysis to Understand Fire Effects with Rim Fire. In, HyspIRI Sceince Workshop. Pasadena, CA.

ABSTRACT

Using Remote Sensing to Characterize Disturbance during a Severe Drought in the Sierra Nevada

By Zachary Tane

Between 2012 and 2016, California experienced an extreme period of drought and high temperatures. During this period there were two particularly notable disturbances in the southern Sierra Nevada. In 2013, the first major disturbance occurred in the form of the Rim Fire. At 1,041 km^2, the Rim Fire is the largest fire ever recorded in the Sierra Nevada. Throughout the drought, but particularly in the latter years, there was also epidemic levels of tree mortality, particularly mortality tied to native bark beetles (*Dendroctonus spp.*) killing pines (*Pinus spp.*).

Using the southern Sierra Nevada as a case study, I investigated the novel insights a next-generation imaging spectroscopy satellite would be able to give in understanding fire and tree mortality globally. Specifically, I showed the potential for imaging spectroscopy based spectral mixture analysis (SMA) as an assessment of fire severity. SMA cover fractions allow for a remotely sensed fire severity metric that would be more readily compared at the global level than those currently in use, such as difference normalized burn ratio (dNBR). I also demonstrated that using the random forest machine learning algorithm, a simulated spaceborne imaging spectrometer would be able to more accurately identify the

location of red stage tree mortality compared to existing multispectral satellites such as Landsat.

In addition, remote sensing was used to gain an understanding of the impact and drivers of tree mortality. For a 2,240 ha watershed, a model of tree crown locations, with species and height identified, was created based on a combination of high spatial resolution airborne imaging spectroscopy and lidar. Then, high-resolution multispectral imagery was interpreted to determine a tree's 2016 status. In the area investigated, the net effect of the drought was to reduce the number of live conifer stems taller than 15 m at the crown level by 75%, primarily due to the death of ponderosa pine. Finally, the factors that distinguished conifers that were alive in 2016 from conifers that died between 2015 and 2016, both within the 2,240 ha watershed and across the southern Sierra Nevada were examined. Trees that survived were typically associated with being located in stands with tree species and height class heterogeneity. Stands in wetter, cooler parts of the Sierra Nevada during the drought were also more likely to survive.

TABLE OF CONTENTS

Chapter 1: Introduction

1.1. Motivation

There has been a global increase in large disturbances in temperate forested environments in the past 50 years (Millar and Stephenson, 2015). Many of these large disturbances can be tied to changing climate, either directly due to increased drought and heat (Allen et al., 2010; Choat et al., 2012), or proximately through increased fire risk (Jolly et al., 2015) and native tree-killing insects acting in novel ways (Allen et al., 2015; Anderegg et al., 2015). Forests in the western United States are no exception to these global trends. The rate of tree mortality has been found to be roughly doubling every 20 to 30 years in parts of the western United States, primarily due to climate (van Mantgem et al., 2009). The number of large fires are increasing (Dennison et al., 2014) as is fire severity (Miller and Thode, 2007). Widespread, drought-connected bark beetle (*Dendroctonus spp.*) outbreaks have also increased (Clark et al., 2016).

Between 2012 and 2016, California experienced an extreme period of drought and above average temperature, including a period between 2012 through 2014 that was likely without historical precedent in the 500-year record (Robeson, 2015). Although extreme, this drought is in line with predictions for higher temperatures and more precipitation variability in California in the next 50 to 100 years (AghaKouchak et al., 2014; Diffenbaugh et al., 2015). In the southern Sierra Nevada, two remarkable disturbances occurred during the drought. The first began on 13 August 2013 when the Rim Fire started in Stanislaus National Forest and would eventually grow to burn 1,041 km^2 of primarily forested lands. The second disturbance occurred in the latter years of the drought when trees began dying across the southern Sierra Nevada (*R5-PR-034, 2016 Aerial Survey Results: California*, 2017; Young

et al., 2017). Most density and drought-related mortality that effects ponderosa pine in the Sierra Nevada is ultimately due to successful bark beetle attack (Oliver, 1995). Since much of the tree mortality is preferentially occurring in pine (Paz-Kagan et al., 2017a), bark beetles are playing a large role in this epidemic tree mortality.

Coincident with this period of drought, several unique forms of remote sensing were being acquired in the southern Sierra Nevada. Airborne Visible / Infrared Imaging Spectrometer (AVIRIS) data were collected three times a year between 2013 and 2015 over the entire southern Sierra Nevada as part of the Hyperspectral Infrared Imager (HyspIRI) preparatory campaign (Lee et al., 2015; Thompson et al., 2015). A visible to near-infrared imaging spectrometer measures radiance at fine (< 20 nm) intervals from approximately 400 nm to 2500 nm. AVIRIS has an approximately 10 nm band width sampled by 224 channels. Although no spaceborne imaging spectrometer similar to AVIRIS currently exists, the HyspIRI preparatory campaign collected data that simulated imagery that would be acquired by the proposed HyspIRI project (Lee et al., 2015). Several other spaceborne imaging spectrometers similar to HyspIRI have also been proposed, including the Environmental Mapping and Analysis Program (EnMAP; Guanter et al. 2015) and the PRecursore IperSpettrale della Missione Applicativa (PRISMA; Stefano et al. 2013).

Over a much smaller area, also in the southern Sierra Nevada, approximately 2,240 ha of the Soaproot Saddle watershed were imaged in 2013 by a combination of high spatial resolution airborne imaging spectroscopy and lidar data as part of the National Ecological Observation Network (NEON; Kampe et al. 2013). The combination of these two remote sensing data sources has been shown to have synergistic capabilities for ecosystem analysis (Asner and Martin, 2009; Koetz et al., 2007).

It is clear that California's drought and subsequent disturbances did not happen in isolation, it is part of a global trend. The motivation of the research presented in this dissertation is to advance the science of using remote sensing for characterizing and analyzing these disturbances at large spatial scales. Although this dissertation is focused on the southern Sierra Nevada, much of the research presented in Chapters 2 and 3 focuses on developing methods that could allow for global disturbance monitoring using a spaceborne imaging spectrometer. For the analysis presented in Chapters 4 and 5, which requires fine-spatial resolution imagery that can only be acquired via aircraft, the methods are flexible enough to be implemented in a variety of forested environments. This dissertation is also motivated by the desire to present useful information to land managers. This will be accomplished both through the specific findings, as well as the processes developed in this dissertation is readily applicable to new locations and contributing to the workflow of forestry models.

1.2. Fire Terminology

To give context to the goals of this dissertation some defining of terminology is needed. The fields of fire ecology and fire-related remote sensing have not always been consistent in their use of the terminology and there is some confusion surrounding the terms fire severity, burn severity, and fire intensity. In this dissertation, I will be using the terms as defined in Lentile et al. (2006). Fire intensity is the temperature and heat released by a fire while it is burning. It is generally measured via a combination of the rate of spread and the energy flux of a fire. Fire severity is the direct effects of fire on the vegetation being burnt, for example, a tree which is directly killed by the heat released from a fire. These effects are often called first order effects (Key and Benson, 2006) and are contrasted with second-order effects that

are the indirect impacts of the fire. These can include weather and erosion after a fire, insect and pathogen attack after a fire, and post-fire plant establishment. Burn severity is the impact of the fire taking into account these second order effects. Generally, fire severity can only be measured in a short time after the fire occurs, whereas burn severity can be measured months to years after the fire.

1.3. Bark Beetle Terminology

This dissertation will follow the terminology of Wulder et al. (2006) when referring to the various stages of bark beetle attack. Before a successful attack, trees are termed healthy. After a successful attack occurs, a tree transitions to the green stage. In this stage a tree's foliage is visibly unchanged (although subtle spectral shifts do occur), however, the attack has interrupted the phloem's ability to transfer nutrients and the tree is no longer viable. The next stage is the red stage, where a tree's needles turn visibly red. In this stage, to a casual observer, the tree would now appear dead. In the final stage, gray stage, a tree's needles have mostly or entirely dropped to the ground and the only the tree's gray branches remain.

1.4. Measuring Fire Severity via Remote Sensing

There are a number of currently viable means for assessing fire severity at large scales. The most common is through the use of vegetation indices in the visible to shortwave infrared (VSWIR). From the perspective of global change monitoring, one clear advantage of indices in this part of the spectrum is they can be calculated using existing spaceborne assets that have frequent repeats times and global coverage, such as the Landsat Operational Land Imager (OLI). The normalized burn ratio (NBR), calculated from a normalized differencing of red (between approximately 630 – 670 nm with Landsat OLI) and shortwave infrared 1 (between approximately 1,570 – 1650 nm), is the most commonly used remote

sensing index associated with fire (Key and Benson, 2006). Frequently, NBR is used in a change detection context, where pre-fire and post-fire scenes are compared, including differenced NBR (dNBR) and relative dNBR (RdNBR; Miller and Thode 2007). NBR and its derivatives are popular due to their ease of calculation and relatively good correspondence to field measurements (De Santis and Chuvieco, 2009; van Wagtendonk et al., 2004; Veraverbeke and Hook, 2013). However, as I will describe in Chapter 2 in more detail, NBR based indices are not without their drawbacks. They are sensitive to local environmental factors such as soil and vegetation type and phenology. This means direct fire severity comparison between fires using NBR-based indices may not be accurate.

Other possible means for remotely sensing fire severity based on VSWIR imagery exist. One common method is the use of spectral mixture analysis (SMA, Adams et al. 1986). By separating a pixel into the relative contributions of green vegetation (GV), non-photosynthetic vegetation (NPV), soil, and char a more theoretically objective and physically meaningful estimate of severity can be made (Kokaly et al., 2007; Veraverbeke and Hook, 2013). Another possible technique for estimating fire severity is radiative transfer models (Chuvieco et al., 2006). These techniques theoretically overcome the weaknesses of NBR in terms of global comparability. However, they are both substantially more complex forms of analysis and require careful consideration of the inputs.

1.5. Measuring Bark Beetle Attack via Remote Sensing

Bark beetle mortality occurs over a large area, is generally grouped, and the spectral change between healthy trees and red stage mortality is generally large, lending itself to VSWIR remote sensing (Wulder et al., 2006). A wide variety of studies using a number of different sensors have focused on the problem of detecting bark beetle caused tree mortality

(see Senf et al. 2017 for a recent review). If monitoring methods are meant to be implementable over large spatial scales, Landsat has generally been the most popular platform (Senf et al., 2017). Analysis can either be single date or multi-date, with multi-date studies generally using annual information (Senf et al., 2017). Both methods can yield fairly high detection accuracy (Meddens et al., 2013).

Images acquired at finer spatial resolutions, obtained either though pointable spaceborne instruments or airborne platforms do not have the capability for global tree mortality monitoring that Landsat does. However, these images have abilities that Landsat and other medium spatial resolution images do not. For example, high spatial resolution multispectral images have been used to identify mortality at the individual tree level (Coops et al., 2006; Dennison et al., 2010). High spatial resolution imaging spectroscopy has been used to identify green-stage tree mortality (Fabian Ewald Fassnacht et al., 2014; Niemann et al., 2015) and understand the species and environmental drivers behind tree mortality (Paz-Kagan et al., 2017a).

1.6. Existing Research on the Rim Fire and Tree Mortality due to the 2012-2016 Drought in the Southern Sierra Nevada

Some studies on the Rim Fire have already been conducted. Most of these studies are related to the ecological impact of the fire and focus on factors that influenced fire severity. Two studies have been conducted that used field plot data to establish pre-fire condition and RdNBR values to measure severity. One was located in a part of the Rim Fire where fires have been allowed to burn relatively uninhibited in the past 40 years (Lydersen et al., 2014) and another in an area where fire suppression has occurred since the 1890's (Harris and

Taylor, 2015). A third study used pre-fire lidar to measure stand characteristics over a 4,461 ha study area (Kane et al., 2015).

Overall, these studies found a mixture of important factors, depending on the study area's history, fire history, and the means of measuring the study area. All studies found elevation and fire weather to be important, with Lydersen et al. (2014) finding whether the fire was burning under plume conditions to be particularly predictive of fire severity. Fire history was also important for Lydersen et al. (2014) and Kane et al. (2015) Both of these plot based studies found shrub cover positively influenced fire behavior. Kane et al. (2015) did not find pre-fire canopy metrics as measured with lidar to be predictive of fire severity.

Although bark beetle mortality in the southern Sierra Nevada only reached notable levels in 2014, several studies and datasets have already been published relating specifically to this event. The US Forest Service has conducted aerial detection surveys (ADS) across the Sierra Nevada each year since 2014 (*R5-PR-034, 2016 Aerial Survey Results: California*, 2017). Asner et al. (2016) used imaging spectroscopy and a network of spaceborne sensors to estimate progressive canopy water stress between 2012 and 2015 throughout California. Young et al. (2017) used the US Forest Service ADS combined with data on climate and tree densities. They found both climate and density played a role in predicting tree mortality in the southern Sierra Nevada. Paz-Kagan et al. (2017) used combined high-resolution imaging spectroscopy and lidar to analyze the predictive power of species, individual tree characteristics, topography, soils, and other factors for tree mortality in the southern Sierra Nevada. They found pine trees at lower elevations to be the most impacted by mortality.

1.7. Objectives and Chapter Summary

I have five major objectives for this dissertation. Broadly, the first two objectives are to develop tools and methods that enhance our ability to quantify disturbances using imaging spectrometry. They are:

1) *To test the ability of imaging spectroscopy to measure fire severity through SMA. To evaluate potential workflows for their accuracy and ability to be implemented on a global scale.*

This objective is the focus of Chapter 2. I used post-fire AVIRIS imagery acquired over the Rim Fire, on 17 November 2013, to fulfill this objective. In order to make the SMA flexible to spectral variability, the Multiple Endmember SMA (MESMA; Roberts et al. 1998) algorithm was implemented. I investigated the impact that reducing the number of bands included in the MESMA analysis and applying different methods for creating a spectral library had on the accuracy of unmixed pixels. In order to assess accuracy, field metrics, including Geo Composite Burn Index (GeoCBI) plots (De Santis and Chuvieco, 2009), and manual interpretation of high spatial resolution WorldView images were used. The manuscript Chapter 2 is based on is published in the journal *Remote Sensing.*

2) *To simulate spaceborne imaging spectroscopy and Landsat-8 images across the southern Sierra Nevada and compare each platform's ability to detect red stage tree mortality. To also, examine whether imaging spectroscopy can more effectively leverage seasonal and annual data than Landsat-8 images.*

This objective is one of the foci of Chapter 3. I used AVIRIS imagery that was acquired between 2013 and 2015 as part of the HyspIRI campaign across the southern Sierra Nevada. The imagery was degraded to simulate HyspIRI imagery and Landsat imagery to address this objective. In order to identify which pixels were non-conifer, healthy conifer, and red stage mortality, a random forest (RF, Breiman 2001) classification was used. The accuracy of single-date images and several temporal combinations of multi-date images was tested and compared for both the imaging spectroscopy and simulated Landsat datasets. In order to train the RF model and assess the accuracy, 2015 WorldView scenes were manually classified across the southern Sierra Nevada. To test the portability of the classification, separate scenes were used for training and for validation. The manuscript Chapter 3 is based on is currently in press in the journal *Remote Sensing and the Environment*.

The latter three objectives describe the ecological impact of tree mortality due to drought. They are:

3) *To identify conifer areas that were green and areas that were dominated by red stage mortality across the southern Sierra Nevada in 2015.*

This objective is another focus of Chapter 3. Multiple classification outputs spanning the southern Sierra Nevada were created in order to address Objective #2. The most accurate of these outputs can be used as a map to identify healthy and red stage mortality trees in 2015.

4) *Using the high-resolution remote sensing available in the Soaproot Saddle area, to identify canopy level trees by species and size class pre-drought and identify the impact of the drought by species and size class in 2016.*

This objective is the focus of Chapter 4. I used high spatial resolution airborne imaging spectroscopy and lidar to accomplish this objective. Specifically, polygons representing individual tree crowns at the canopy-level were created using lidar. An object-level classification was performed with RF, using the crown polygons combined with imaging spectroscopy. To analyze a tree's 2016 status, WorldView imagery was used. Two outputs of the 2016 status were created, a spatially explicit map of mortality created from a maximum-likelihood classification (MLC) and a non-spatially explicit Monte Carlo simulation model output. The Monte Carlo output was theoretically more accurate in its ability to estimate the live trees in 2013 and 2016 by species and size class, as it was able to propagate error from the various steps in the estimation.

5) *To identify the distinguishing ecological variables separating trees that were alive and red stage mortality in 2016, at both the broad scale of a large part of the southern Sierra Nevada and the narrow scale of the Soaproot Saddle area.*

This objective is the focus of Chapter 5. The results of Chapter 3 include areas that were classified as healthy conifers in 2015. Additional WorldView imagery was collected across the southern Sierra Nevada in 2016. Using the 2015 healthy conifers as a sampling base, areas across the southern Sierra Nevada were randomly sampled and their 2016 status

determined. Using the results from Chapter 4 and WorldView imagery from 2015 and 2016, individual ponderosa pines that were alive in 2015 were randomly sampled and their 2016 status determined. For both scales, possible ecological variables that may influence tree mortality were considered. For the southern Sierra Nevada, this included spectral indices processed from the AVIRIS imagery, for Soaproot Saddle, this included canopy structure and composition variables identified from the lidar data and in Chapter 4.

Chapter 2: Evaluating Endmember and Band Selection Techniques for Multiple Endmember Spectral Mixture Analysis using Post-Fire Imaging Spectroscopy

Zachary Tane[1,2], Dar Roberts[1], Sander Veraverbeke[3,4], Ángeles Casas[5], Carlos Ramirez[2], Susan Ustin[6]

[1]University of California Santa Barbara, Department of Geography

[2]United States Department of Agriculture, Forest Service, Pacific Southwest Region, Remote Sensing Lab

[3]Vrije Universiteit Amsterdam, Faculty of Science

[4]University of California Irvine, Department of Earth System Science

[5]Independent Researcher

[6]University of California Davis, Center for Spatial Technologies and Remote Sensing (CSTARS), Department of Land, Air, and Water Resources

This chapter is based on a manuscript published in the journal of *Remote Sensing*:

Tane, Z., Roberts, D., Veraverbeke, S., Casas, A., Ramirez, C., & Ustin, S. (2018). Evaluating Endmember and Band Selection Techniques for Multiple Endmember Spectral Mixture Analysis using Post-Fire Imaging Spectroscopy. Remote Sensing, 10, 389.

2.0. Abstract

Fire impacts many vegetated ecosystems across the world. The severity of a fire is major component in determining post-fire effects, including soil erosion, trace gas emissions, and the trajectory of recovery. In this study, I used imaging spectroscopy data combined with Multiple Endmember Spectral Mixture Analysis (MESMA), a form of spectral mixture analysis that accounts for endmember variability, to map fire severity of the 2013 Rim Fire. I evaluated four endmember selection approaches: Iterative Endmember Selection (IES), count-based within endmember class (In-CoB), Endmember Average Root Mean Squared Error (EAR), and Minimum Average Spectral Angle (MASA). To reduce the dimensionality of the imaging spectroscopy data I used uncorrelated Stable Zone Unmixing (uSZU). Fractional cover maps derived from MESMA were validated using two approaches: 1) manual interpretation of fine spatial resolution WorldView-2 imagery, and 2) ground plots measuring the Geo Composite Burn Index (GeoCBI) and the percentage of co-dominant and dominant trees with green, brown, and black needles. Comparison to reference data demonstrated fairly high correlation for green vegetation and char fractions (r^2 values as high as 0.741 for the MESMA ash fractions compared to classified WorldView-2 imagery and as high as 0.841 for green vegetation fractions). The combination of uSZU band selection and In-CoB endmember selection had the best trade-off between accuracy and computational efficiency. This study demonstrated that detailed fire severity retrievals based on imaging spectroscopy can be optimized using techniques that would be viable also in a satellite-based imaging spectrometer.

2.1. Introduction

Fire behavior, size, and severity are changing in the western United States (Dennison et al., 2014; Miller et al., 2009; Steel et al., 2015). To fully comprehend these changes, techniques to reliably map fire effects over large areas are required. The most common means of assessing fire severity with remote sensing is using the NBR and its derivatives (Key and Benson, 2006; Miller and Thode, 2007). NBR based techniques are popular because of their simplicity, ease of use, and relatively good performance when compared to field measurements (Cocke et al., 2005; van Wagtendonk et al., 2004). The NBR, however, is sensitive to variations in soil brightness (Smith et al., 2010), vegetation type (Epting et al., 2005), and vegetation density (Lentile et al., 2009). These limitations constrain the use of NBR-based indices for consistent fire severity assessments over large areas within heterogeneous ecosystems (Lentile et al., 2009). Variation in fire severity can effectively be broken down into detectable differences in the relative abundance of char, green vegetation, dead vegetation, and bare soil; remotely sensed fire severity assessments are therefore essentially based on mixtures composed of these four constituents. Under this paradigm, Spectral Mixture Analysis (SMA), in which reflectance is assumed to a be a linear combination of components or endmembers at a subpixel level (Adams et al., 1986; Roberts et al., 1993), represents a viable alternative to NBR-based analysis, potentially overcoming NBR's sensitivity to different cover type and soil brightness variation (Quintano et al., 2013; Rogan and Franklin, 2001). SMA has been used previously to characterize tree mortality and soil char cover (Hudak et al., 2007; Kokaly et al., 2007; Lentile et al., 2009; Robichaud et al., 2007; Veraverbeke and Hook, 2013).

Lentile et al. (2006) defines fire severity as the immediate ecosystem impacts of fire; burn severity, in contrast, is defined as the combined shorter and longer term ecosystem impacts and response to fire. Key and Benson (2006) also separates first-order effects, which are related to the fire only, and second-order effects, which are related to other environmental (e.g. wind and rain) and vegetative processes. Veraverbeke et al. (2010) followed these conventions and used the term fire severity when images were acquired soon after the fire (e.g. within the first month) and second-order effects can safely be neglected.

In SMA, an endmember class is one of the categories the image will be divided into, and an endmember is the individual training spectra that are constituents of each endmember class. In simple SMA, only one endmember represents each endmember class across the image. MESMA, in contrast, allows the endmember representing each endmember class to vary on a per-pixel basis (Roberts et al., 1998). This approach accounts for the variability that may exist within each endmember class and further allows for consistency and accuracy across ecosystems where there could be considerable spectral variability within an endmember class (Roberts et al., 1998; Somers et al., 2011).

SMA is particularly well suited for imaging spectrometry data, as the large number of bands provide additional information for cover type discrimination in critical, but spectrally narrow regions; for example, the red edge for green vegetation discrimination (Green et al., 1998). The AVIRIS, samples spectra from 350 nm to 2,500 nm at a nominal sampling interval of 10 nm (Jia et al., 2006). There is currently no spaceborne imaging spectrometer with a similar signal-to-noise ratio to AVIRIS and global coverage with frequent return intervals, which currently impedes the use of imaging spectroscopy for fire severity comparisons at regional scales and over longer time periods. However, there are several

proposed spaceborne imaging spectrometers, including the EnMAP (Guanter et al. 2015), the PRISMA (Stefano et al. 2013), and the HyspIRI (Lee et al. 2015), that would make using imaging spectroscopy to monitor fire severity possible at regional to global scales within the decade.

A drawback of MESMA, particularly if three or more endmember classes are allowed to be modeled within a single pixel, is that the number of endmember combinations tested can be large. A variety of approaches have been developed that attempt to select the minimum number of spectra in a library needed to represent within endmember class variation and therefore eliminate redundant spectra. Many techniques focus on automated or semi-automated endmember selection, which identifies pure pixels through the extremes of image data (Boardman et al., 1995) or the construction of synthetic endmembers based on image data (Tompkins et al., 1997). Other techniques first create a large spectral library from various sources and then reduce its size to achieve a library that is both parsimonious and captures each endmember class's variability (Dennison et al., 2003; Roth et al., 2012; Schaaf et al., 2011). Several means exist to evaluate which endmembers to keep. Generally, criteria evaluated focus on either which endmembers best represent their endmember class (Dennison et al., 2004; Dennison and Roberts, 2003; Roberts et al., 2012), or which endmembers best model the library as a whole (Schaaf et al., 2011). All techniques have slightly difference balances between capturing spectral variability and creating efficient libraries. While there are several studies reviewing endmember extraction techniques (Keshava and Mustard, 2002; Parente and Plaza, 2010; Veganzones and Grana, 2008), the comparison of endmember selection techniques for MESMA is rare (Roth et al., 2012), and to my knowledge, there has been no evaluation of various endmember selections techniques

for cover fraction identification (MESMA with multiple non-shade endmembers allowed per pixel).

Individual bands in imaging spectroscopy tend to be highly correlated, and the inclusion of all bands in image analysis techniques increases computational times and can decrease accuracy (Keshava and Mustard, 2002; Pal and Foody, 2010). Data reduction techniques are therefore often applied imaging spectroscopy data sets prior to SMA (Keshava and Mustard, 2002); two of the more common are Principal Component Analysis (PCA; Miao et al. 2006) and maximum noise fraction (MNF; Green et al. 1988). PCA, MNF, and similar techniques reduce data dimensionality based on the spectral properties of the image; however, they do not necessarily do so in a manner that improves separability between endmember classes (Li, 2004). Asner and Lobell (2000) proposed a data reduction technique designed specifically to improve the accuracy of SMA when applied to plant cover with AutoSWIR. AutoSWIR uses *a priori* optical properties of leaf, litter, and soil material to select critical spectral regions to use for spectral unmixing. Somers et al. (2010) proposed a technique similar to AutoSWIR in stable zone unmixing (SZU), which uses variability within and between endmember classes to select spectral regions to use in SMA. Since SZU is based solely on the input spectral library, it has the built-in assumption that the endmembers in a spectral library are representative of the variability of the spectra in the image to be analyzed; however, it has the advantage of selecting spectral regions specific to the problem. SZU has been demonstrated to be effective in invasive species monitoring, soil type classification, and oil spill detection and tracking (S. H. Peterson et al., 2015; Somers et al., 2010; Zhao et al., 2014). Neither autoSWIR nor SZU specifically addresses the highly correlated nature of adjacent bands. Somers and Asner (2013) proposed a further refinement

on SZU, uncorrelated SZU (uSZU), which selects bands that capture the maximum variability within and between endmember classes while eliminating highly correlated bands. uSZU was shown to have improved cover abundance estimate accuracy and performance times compared to SZU (Somers and Asner, 2013).

In this chapter, I test the ability of imaging spectroscopy based MESMA to derive cover fractions that correspond with field measurements. Additionally, I test the specific effects of four different endmember selection techniques and one band reduction technique on MESMA's accuracy and processing time in the context of deriving indicators of fire severity of a large wildfire using imaging spectroscopy.

2.2. Methodology

In order to test the effectiveness of derived cover fractions at modeling the actual mixed composition of pixels, four post-fire AVIRIS flight lines were processed using MESMA. I used four endmember selection techniques and tested each technique with both the full AVIRIS spectra and a reduced spectral subset determined from a band selection algorithm. The result was eight separate spectral libraries. Each of these eight libraries was used to perform a separate run of the MESMA algorithm (Figure 2.1). In order to evaluate MESMA derived fractions correspondence with fire severity, two separate validation data sets were used. First, the various cover fractions generated by the eight MESMA runs were compared through linear regression against randomly selected and manually classified plots on WorldView-2 scenes. Using MESMA derived fractions from a spectral library that performed well, the relationship of the cover fraction with two field measurements, GeoCBI, and the percent cover of green, brown, and black trees over an area, was evaluated.

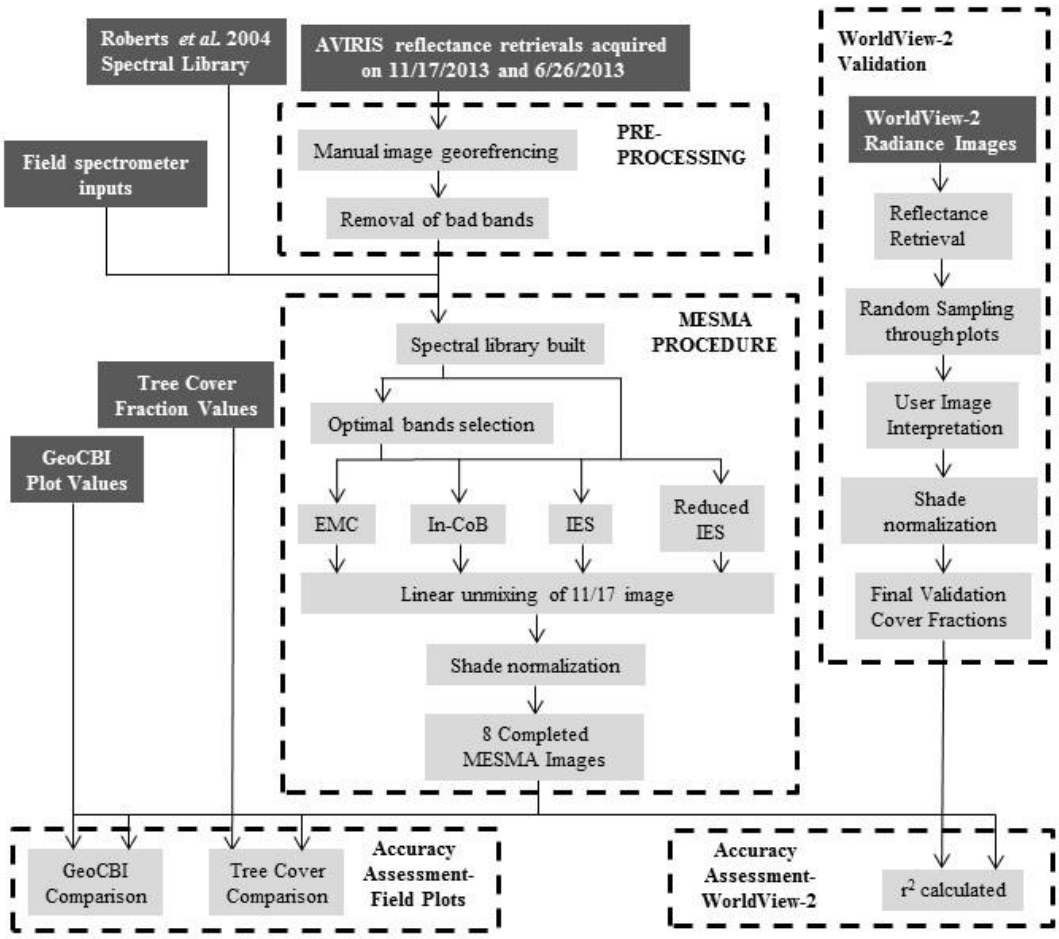

Figure 2.1. Flow chart of methods. Endmembers collected via Airborne Visible/Infrared Imaging Spectrometer (AVIRIS), field spectrometry, and an existing spectral library are used to perform Multiple Endmember Spectral Mixture Analysis (MESMA). Before MESMA, four different means of determining the optimal endmembers from a large spectral library were used: a technique that, for any given endmember within an endmember class, evaluates the count of the other endmembers modeled under an error threshold (In-CoB); a technique that uses the endmember average root mean square error (EAR), minimum average spectral angle (MASA), and In-Cob (EMC); a technique which uses forward-selection to iteratively add or remove spectra until an optimal state is reached (IES); and a technique that post-processes the IES library to produce a more parsimonious result (Reduced IES). Each endmember selection technique is tested with a full AVIRIS spectrum and with a spectral subset. The fractions are tested for goodness of linear fit with the WorldView-2 data via coefficient of determination value (r^2) and also compared with field data.

2.2.1. Methodology

The Rim Fire occurred in California's Sierra Nevada, starting in the Stanislaus National Forest and burning into Yosemite National Park (Figure 2.2). The Rim Fire started on 17 August, 2013 and was contained on 24 October, 2013. According to the official fire perimeter statistics from the state of California (http://frap.fire.ca.gov/) the Rim Fire burned

104,131 ha and was the largest fire ever recorded in the Sierra Nevada and the fourth largest in California (Steel et al., 2015). Several vegetation types were affected by the fire: coniferous forests dominated by Ponderosa pine (*Pinus ponderosa*), Lodgepole pine (*Pinus contorta*), red fir (*Abies magnifica*), and mixed conifer stands; deciduous and evergreen hardwood forests made up of various lower montane species including blue oak (*Quercus douglasii*), valley oak (*Quercus lobata*), interior live oak (*Quercus wislizeni*), and California buckeye (*Aesculus Californica*); annual grass; and shrubs, primarily composed of many common upper and lower montane Sierra Nevada chaparral species such as manzanita (*Arctostaphylos spp.*) and California lilac (*Ceanothus spp.*).

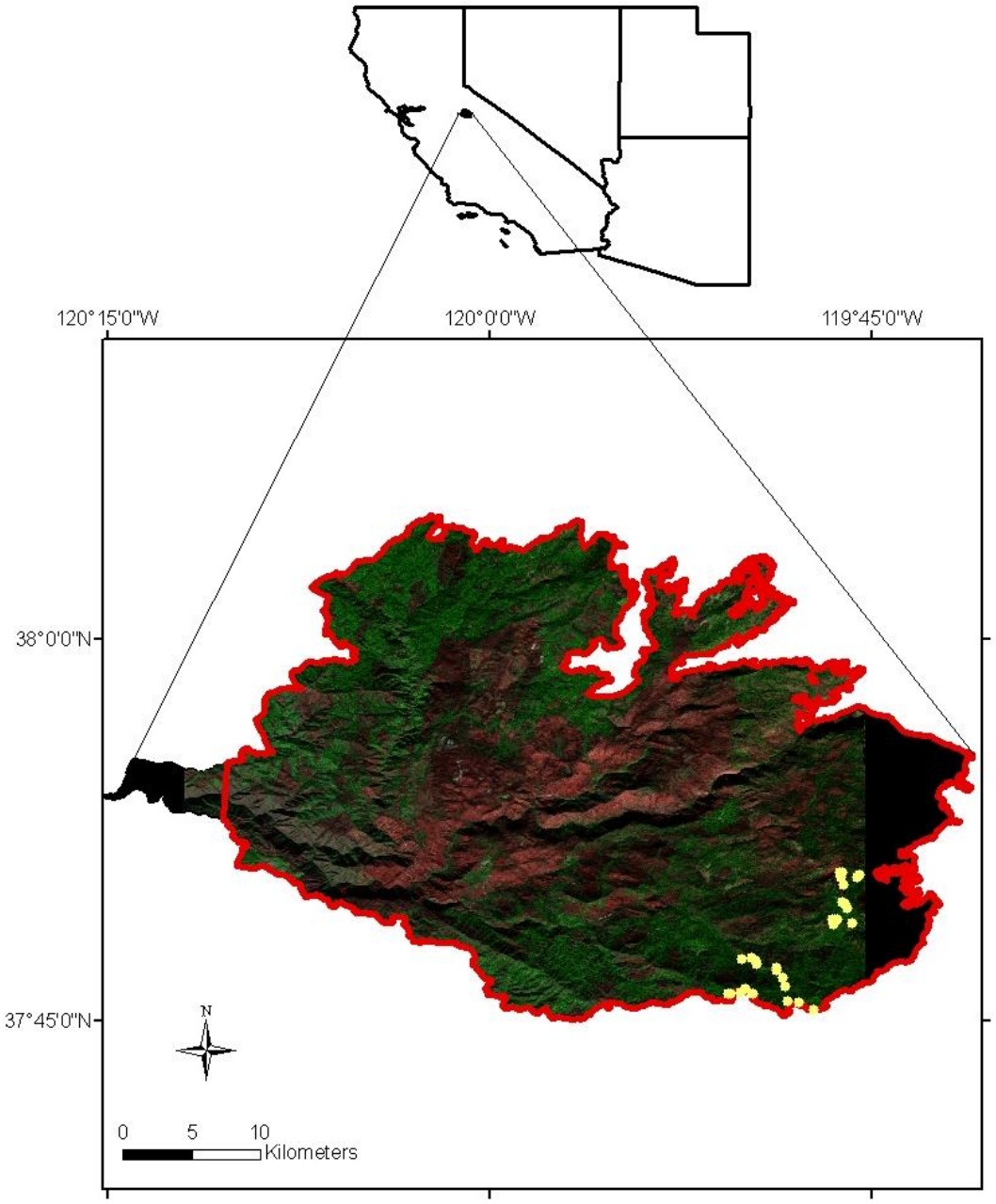

Figure 2.2. Airborne Visible/Infrared Imaging Spectrometer (AVIRIS) false color composite of the Rim Fire from 17 November, 2013 imagery. The composite used bands centers at 2,217 nm (red), 832 nm (green), and 657 nm (blue). Areas of no data within the Rim Fire are portrayed as black. Areas included in the mosaic of 28 September, 2013 WorldView-2 imagery are outlined in red. The location of the field plots used in this analysis are portrayed with yellow dots.

2.2.2. AVIRIS Imagery and MESMA

2.2.2.1. Preprocessing

Level 2 ortho-reflectance AVIRIS flight lines were acquired from the Jet Propulsion Lab (JPL) ftp site (https://aviris.jpl.nasa.gov/data/AV_HyspIRI_Prep_Data.html). The flight lines used in this analysis were f131117t01p00r07, f131117t01p00r08, f131117t01p00r09, and f131117t01p00r10, all acquired on 17 November, 2013. Before retrieval, the images had been orthorectified. Surface reflectance was retrieved using ATmospheric REMoval program (ATREM; Thompson et al. 2015). Images were further manually georeferenced using United States Geological Survey (USGS) 2004 1m digital orthophoto quarter quad (DOQQ) maps (http://nationalmap.gov/viewer.html) as base maps. Images were warped using a first-degree polynomial with nearest neighbor resampling. Images were resampled to a uniform 14.8 m on a side pixel size. The flight lines cover approximately 93% of the Rim Fire burn scar. Wavelengths 365 - 405 nm, 1325 - 1420 nm, 1810 - 2040nm, and 2450 - 2500nm were known to either be associated with atmospheric water absorption features or found to contain significant atmospheric artifacts and a low signal-to-noise ratio from visual inspection; bands within these wavelengths were not considered in further processing, leaving 177 AVIRIS bands for use in the analysis. In addition, flight lines over the same area from 26 June, 2013 were used as sources for the spectral library used for the MESMA process. The flight lines used for this purpose were f130626t01p00r13, f130626t01p00r14, and f130626t01p00r15. These flight lines were processed using procedures already described.

2.2.2.1. Spectral Library

Five different endmember classes were used to unmix the Rim Fire images: GV; NPV, which includes dead needles, forest litter, bark senesced grass and other non-

photosynthetically active plant material; soil, which includes bare soil and rock; char, which includes charred plant material and ash; and shade. Typical sources for endmembers include either spectra derived from the field, laboratory, or spectra derived from the imagery itself using pure pixels (Settle and Campbell, 1998).

In this study, a combination of sources were used (Table 2.1). Field samples of charcoal, non-photosynthetic vegetation and substrate were collected and analyzed at the JPL spectroscopy lab (Baldridge et al., 2009). Measurements in the 400 - 2500 nm spectral domain were obtained with an Analytic Spectral Devices (ASD) Full Range Spectrometer under artificial lighting conditions with an ASD Pro lamp. Reflectance was calibrated using a white Spectralon panel. I also used spectra collected from AVIRIS imagery, acquired on 26 June, 2013 and 17 November, 2013. To extract these spectra, polygons of areas composed solely of one of the four endmember classes (not including shade) were identified in the images. The spectra of all pixels within each polygon were extracted and labeled by endmember class. The spectral profile of each pixel was then manually reviewed to assure that it was consistent with the endmember class it was labeled as. To capture spatial scales that were not otherwise available in my analysis, an existing spectral library created from Wind River Research Forest (in Southern Washington state) was used (Roberts et al., 2004). This library included collections of leaves (branches) and tree bark, measured with an ASD in the field**.** Tree crowns measured *in situ* via a canopy crane were also included in this library. Although the spectra in the Wind River library were acquired in a different geographic location, many of the species and genera are common for both locations. Although Roberts et al. (2004) also included stand level spectra measured with AVIRIS, these spectra were not included in this study.

Table 2.1. The number and origin of endmember used for the source spectral library. Analytic Spectral Devices is abbreviated as (ASD) and denotes field collected samples spectrally analyzed at a lab. Images acquired through Airborne Visible/Infrared Imaging Spectrometer are abbreviated as (AVIRIS). Spectra developed during a study in Wind River Research Forest (Roberts et al., 2004) are denoted as Wind River. Green vegetation is abbreviated as (GV) and non-photosynthetic vegetation as (NPV).

	Char	GV	NPV	Soil	Total
17 November AVIRIS	457	308	0	358	1227
26 July AVIRIS	0	1739	245	510	2634
ASD	21	0	3	46	70
Wind River	0	498	129	139	766
Total	478	2545	377	1053	4453

2.2.2.3. Band Selection

Once the spectral library was finalized, the uSZU band selection technique (Somers and Asner, 2013) was performed to identify bands that optimize endmember class discrimination. uSZU is an automated band selection technique which attempts to select bands which maximize variation between endmember classes in a spectral library while minimizing the correlation between selected bands. uSZU assigns each band a Stability Index (SI) value based on the interclass variability divided by the intraclass variability for each class (Somers and Asner, 2013):

$$\boldsymbol{SI_i} = \frac{\boldsymbol{\Delta inter,i}}{\boldsymbol{\Delta intra,i}} = \frac{\left|\sum_{j=1}^{k} \boldsymbol{R_{mean,j,i}}\right|}{\mathbf{1.96} * \sum_{j=1}^{k} \boldsymbol{\sigma_{j,i}}} \qquad (2.1)$$

Where k is the total number endmembers, $R_{mean,j,i}$ is the mean reflectance for endmember class *j* at wavelength *i*, and $\sigma_{j,i}$ is the standard deviation of class *j* for wavelength *i*. The band with the highest SI value is selected. Then a spectral correlation value (Corr) is calculated:

$$\boldsymbol{Corr(X,Y)} = \frac{\boldsymbol{cov(X,Y)}}{\boldsymbol{\sigma_x \sigma_y}} \qquad (2.2)$$

Where $cov(X,Y)$ is the covariance between the selected waveband, X and each remaining waveband, Y; and σ is the standard deviation. All bands with *corr* values above a predetermined threshold c are then discarded. The process is repeated, with the threshold for correlation needed to discard a band decreasing by the value i with each iteration. For this study, values of c=0.99 and i=0.001 were used, both of these values were tested in (Somers and Asner, 2013) and found to give acceptable accuracy. MESMA that was based on uSZU band reduced spectral libraries will be noted in this chapter by including the term "uSZU" in the name.

2.2.2.4. Endmember Selection

Several approaches have been developed for determining the relative value of individual endmembers for representing their endmember class. One method for doing this is a count-based (CoB) approach, where each endmember is selected iteratively, and, using simple SMA, tested to see how many endmembers it can successfully model within the spectral library, using a predetermined Root Mean Square Error (RMSE) threshold to define success (Roberts et al., 2003). When this approach is applied to an endmember within its own endmember class, it is called (In-CoB); a desirable endmember will have a high In-CoB number (indicating a large number of other endmembers within the endmember class are derivative). This technique can also be applied against all the endmember classes which the endmember does not belong (Out-CoB), in this case, a desirable endmember will have a low Out-CoB number, indicating that this endmember would minimize confusion with other endmember classes.

Another approach for selecting endmembers is Endmember Average Root Mean Square Error (EAR), which evaluates each endmember's ability to model all other within class

endmembers based on a summed RMSE (Dennison and Roberts, 2003). EAR is calculated using the following formula:

$$\boldsymbol{EAR}_{\boldsymbol{A_i}} = \frac{\sum_{j=1}^{n} \boldsymbol{RMSE}_{\boldsymbol{A_i A_j}}}{\boldsymbol{n-1}} \qquad (2.3)$$

Where *A* is an endmember class, A_i is the selected single endmember, and A_j are each of the other endmembers within the endmember class, and *n* is the total number of spectra in class *A*. A smaller EAR value is more desirable. Another approach, Minimum Average Spectral Angle (MASA, (Dennison et al., 2004)), is similar to EAR but evaluates the summed spectral angle (Kruse et al., 1993) instead of the RMSE fit. Both EAR and MASA evaluate only within an endmember class and do not evaluate interclass confusion.

Two techniques based on EAR, MASA, and CoB were used in this chapter. The first technique used a combination of EAR, MASA, and CoB to select three endmembers, it will therefore be abbreviated to "EMC". The combined EMC technique selected three endmembers for each endmember class: an endmember which minimizes the EAR value, an endmember which minimizes the MASA value, and an endmember which maximizes the In-CoB value. If multiple endmembers had the same In-CoB value, the endmember with the smallest Out-CoB value was selected. If the same endmember is selected through multiple EMC criteria (for example, the spectra that minimizes MASA also minimizes EAR), then fewer than three endmembers were used for that endmember class. The In-CoB (Roberts et al., 2012) technique was also used in this study. For this technique, the In-CoB value of each endmember in an endmember class was evaluated, and any endmember with a unique In-CoB value was selected. If multiple endmembers have the same In-CoB value, the endmember with the minimum EAR value was selected. Another approach to endmember selection is Iterative Endmember Selection (IES; (Schaaf et al., 2011), which first picks two

endmembers that maximize the performance of two-endmember SMA classifying the entire spectral library, as determined by using Cohen's kappa (Cohen, 1960). The algorithm then iteratively adds and removes endmembers in order to maximize kappa until the smallest spectral library that maximizes kappa is developed. While the other endmember selection approaches focus on within-class variability, IES explicitly considers confusion of endmembers between classes. In this study, the parameter of 0.025 was used as an RMSE constraint for the two-endmember SMA needed to classify the spectral library (Roth et al., 2012). Spectral libraries processed in this way will be referred to as "IES".

IES generally results in relatively large spectral libraries that can make the resultant MESMA analysis computationally expensive. Roberts et al. (2017) proposed a method for reducing the size of IES generated spectral libraries through an iterative process, wherein the brightest endmember in each endmember class is initially chosen and all endmembers are modeled as a mixture of that endmember and shade are subsequently removed from the spectral library. Following the first pass, a new set of bright endmembers are selected from the reduced library, targeting endmembers that are most spectrally distinct from the first set. The process is repeated iteratively until either there are no more endmembers within a class in the reduced library, or new endmember selections fail to further reduce the library. The goal of this process is to identify the smallest set of endmembers for each class that also fully characterizes the spectral diversity of that class. The final result is a spectral library that retains the high accuracy of IES, while significantly reducing the number of endmember combinations. Spectral libraries processed in this way will be referred to as "Reduced IES".

2.2.2.5 MESMA

Four endmember MESMA (a maximum mixture of three endmember classes and shade could be modeled for any given pixel) was performed on the post-fire images using the resultant eight spectral libraries. In order for a model with more endmembers to be chosen over a model with fewer endmembers, the model with more endmembers must improve the model's RMSE for the pixel by a minimum threshold of 0.007 (Roberts et al., 2012). The endmember and shade fraction were constrained to be physically reasonable (no fractions below 0 or above 1 were allowed). The shade fraction was further constrained to be no higher than 0.8. A maximum allowed RMSE of 0.025 was also used to constrain the MESMA model (Roberts et al., 1998).

2.2.3. Validation

2.2.3.1. WorldView-2 Imagery

High spatial resolution imagery provides a validation source for cover fractions over large portions of the fire area. WorldView-2 is a commercially operated very high spatial resolution, multispectral satellite imager. Twelve WorldView-2 images from 28 September 2013 that together captured about 97% of the Rim Fire burn scar (Figure 2.2) were purchased from Satellite Imaging Corp. The images had a pixel resolution of 2 m. After acquisition, images were converted into reflectance using Atmospheric and Topographic CORrection (ATCOR) as implemented in the PCI Geomatica software package (PCI Geomatics, Geomatica version 2014) using a LiDAR data set acquired by the National Center for Airborne Laser Mapping (NCALM-University of Houston).

In order to compare the AVIRIS-derived MESMA analysis and the WorldView-2 images, 120 square samples were randomly selected. The samples were 119.2 m on a side, or equivalent to an eight by eight square of AVIRIS pixels, this was chosen to reduce

problems of differences in georeferencing between the images, as well as reduce the effect of pixels which are only partially within the sample area in the AVIRIS imagery. Areas within the sample squares were manually interpreted and digitized from the WorldView-2 imagery into five cover classes: GV, NPV, char, soil, and shadow (Figure 2.3). The spectral resolution of WorldView-2 typically allowed for easy discrimination of GV. The NPV, char, and soil classes were not always easy separable spectrally, but contextual clues such as shape and texture were often helpful in separating these classes. There were likely some pixels that were misclassified, but overall this was considered a minor source of error.

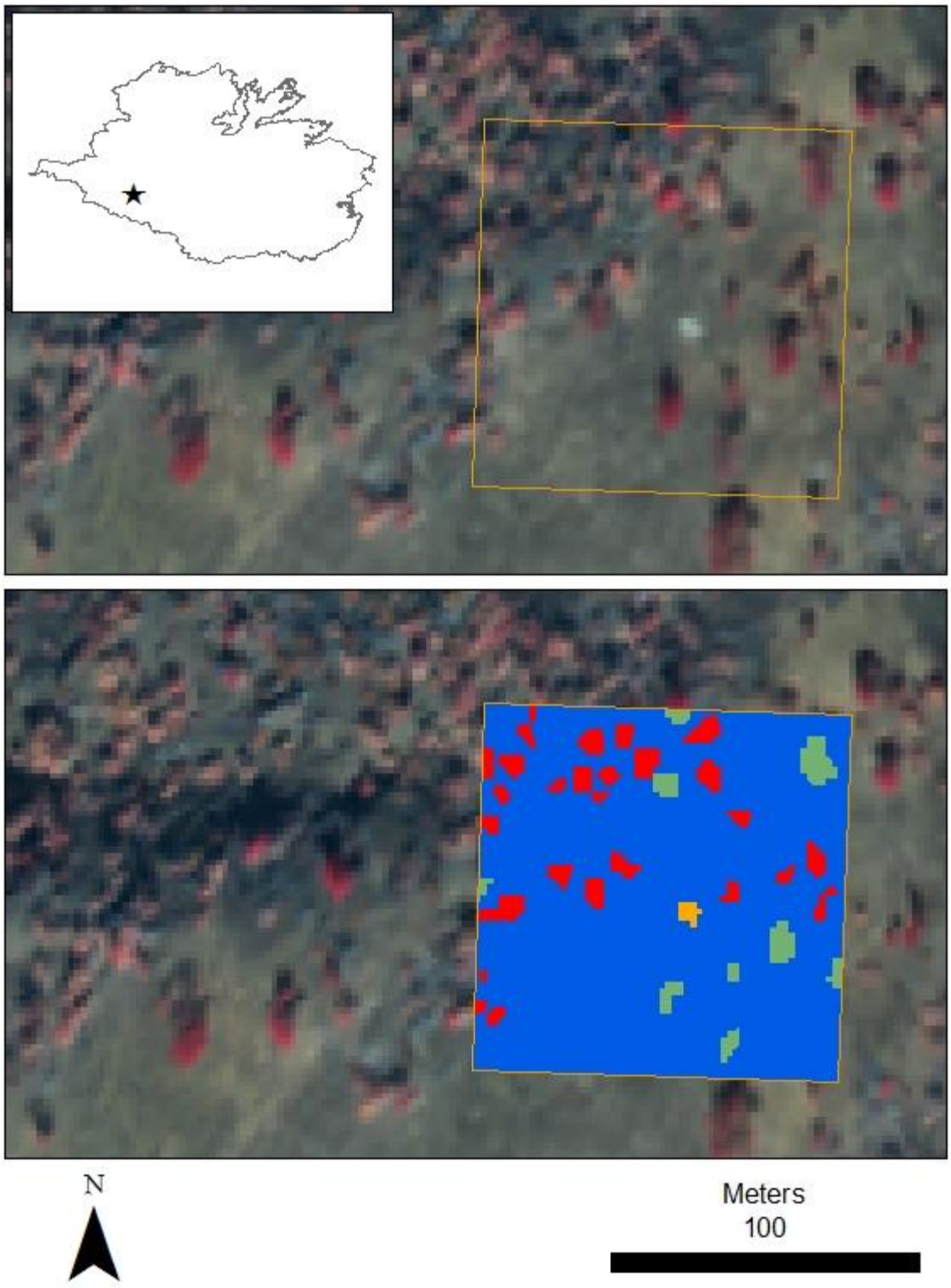

Figure 2.3. An example of a randomly selected manually classified WorldView-2 plot, the false color infrared WorldView-2 imagery uses band centers at 830 nm for red, 660 nm for green, and 545 nm for blue. The upper image displays just the WorldView-2 imagery and the sampling box, the lower box has the classified area. In the lower image blue represent char dominated pixels, green represents green vegetation dominated pixels, red

represents non-photosynthetic vegetation dominated pixels, orange represents soil dominated pixels. An overview of the plot location is featured in the top left.

For both the eight MESMA unmixing results and the manually interpreted high-resolution imagery, the average cover for each cover class was calculated for each point, then the fractions were shade normalized, in which the shade cover fraction was removed by dividing each endmember by the total percent cover of all non-shade endmembers (Adams and Gillespie, 2006). This allowed the relative abundance of the non-shade endmembers classes to be compared by partly correcting for the effects of differential solar geometry between the two images (Rogan and Franklin, 2001). The quality of a linear fit for the relationship between each of the eight MESMA analysis and the manually identified imagery based on validation plots was assessed.

2.2.3.2. Field Plots

Thirty-four field plots of fire severity were collected in October 2013. The plots were located in the southeastern part of the fire and were, due to permitting restrictions, all taken within Yosemite National Park. Five severity was assessed in 30 by 30 m square shaped plots. The plot's center coordinates were recorded with a handheld Trimble GeoExplorer 6000 series GeoXH GPS device (these unit average approximately 1-m x and y error, see Figure 2.2 for plot locations). The plots were located no less than 200 m apart and were taken in areas of relatively homogeneous fuel type and fire severity. Four of the 34 original plots were removed from the analysis since they were located outside of AVIRIS images of 17 November, 2013.

GeoCBI (De Santis and Chuvieco, 2009), a modified version of Composite Burn Index (CBI) (Key and Benson, 2006), was measured in the field plots. GeoCBI divides the ecosystem into five different strata: (i) substrates; (ii) herbs, low shrubs and trees less than 1

m; (iii) tall shrubs and trees of 1 to 5 m; (iv) intermediate trees of 5 to 20 m; and (v) tall trees taller than 20 m. In the field form, 20 different factors can be rated (e.g. soil and rock cover/color change, percent leaf area index change, char height) but only those factors present and able to be reliably evaluated for that strata are considered. Ratings are given on a continuous scale between zero and three and the results are averaged per stratum. These stratum averages are weighted according to their fractional cover within each plot to compute a final GeoCBI rating. GeoCBI scores range from zero to three, with three representing the highest severity. In addition to GeoCBI, every dominant and co-dominant tree within each plot was identified. Trees were then assigned to three possible classes based on their needle color: green, brown, or black.

To compare the 30 by 30 m GeoCBI plots with the 14.8 m pixel size, a weighted plot level averaging of pixels was performed. Weights were assigned based on each pixel's percentage of area within a plot. A weighted average of all pixels within an individual plot was then calculated, and compared with the plot level data.

2.3. Results

2.3.1. uSZU Band Selection

After uSZU of the 177 original bands, 20 were retained in the analysis. Selected bands ranged across the spectrum with a preference for the red edge (five bands were selected between 670 and 735 nm). uSZU also appears to have selected several bands that are at the edges of wavelengths removed due to atmospheric noise, suggesting the sensitivity of the technique to spectral artifacts. Figure 2.4 shows the final selection of bands using the uSZU algorithm.

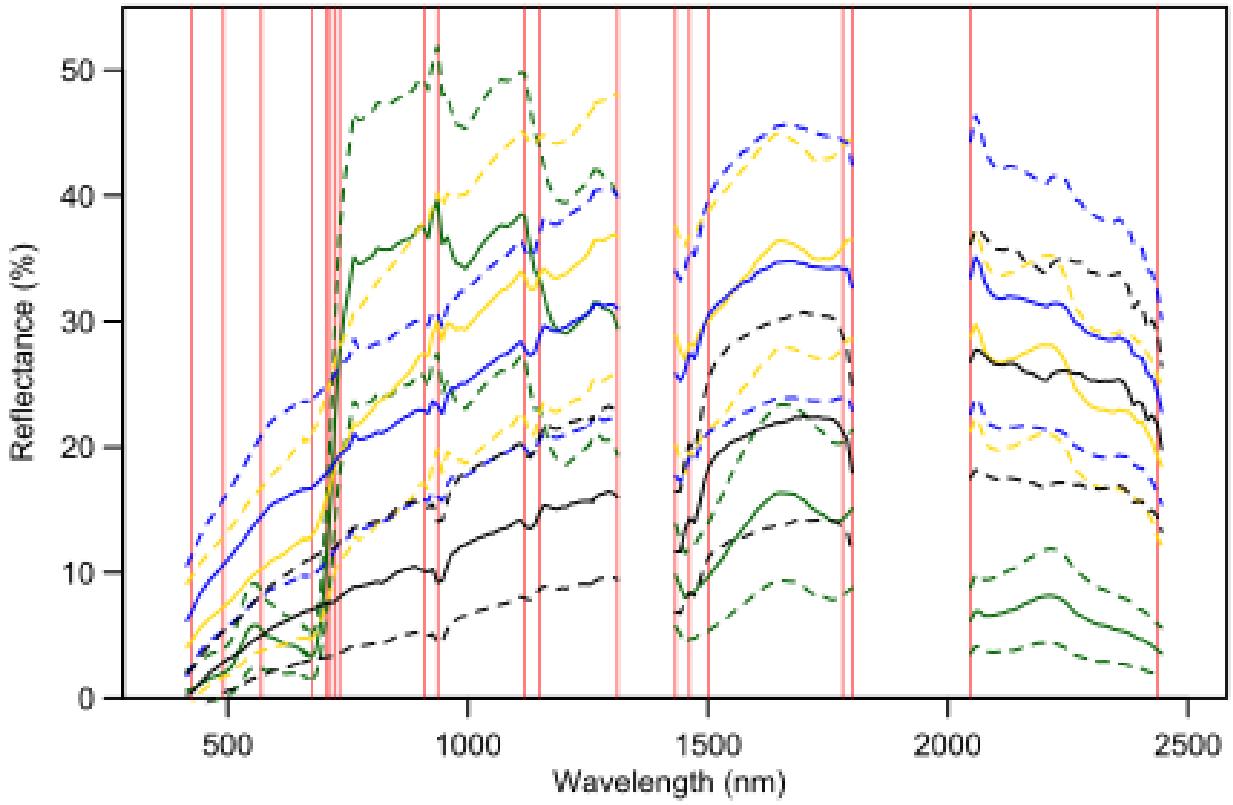

Figure 2.4. Spectral profile of the average spectra in each endmember class (solid line), plus or minus one standard deviation of the spectral average (dotted line). Green vegetation is represented by dark green, non-photosynthetic vegetation is represented by yellow, soil is represented by blue, and char is represented by black. Spectral bands selected by the uncorrelated Stable Zone Unmixing (uSZU) algorithm are represented by red vertical lines.

2.3.2. uSZU Band Selection

The number of endmembers selected by each technique varied considerably (Table 2.2). EMC has an inherent limit to the number of endmembers that may be selected; in EMC no more than the number of endmember classes multiplied by three endmembers are kept (the maximum possible number of endmembers in an EMC reduced library is therefore 12 in this study). uSZU generally had the effect of increasing the number of endmembers selected for all techniques except EMC. The increase was generally moderate, resulting in a 10 - 25% increase in the number of endmembers. Despite the larger number of endmembers selected,

the processing time for the MESMA algorithm was dramatically reduced for all band reduction techniques, with time reductions ranging between 30 and 55%.

Table 2.2. The number of endmembers and modeling times of various combinations of endmember and band selection techniques. Modeling time was assessed on a 640X530 pixel Airborne Visible/Infrared Imaging Spectrometer (AVIRIS) scene within the Rim Fire. Models were run using a computer with an Intel Xeon central processing unit E7-4850v2 at 2.3 GHz with 48 cores and 512 gigabytes of random-access memory. Models were run in a manner to minimize run time with computer resources. Uncorrelated Stable Zone Unmixing (uSZU) represents a feature reduction technique. EMC, In-COB, and IES are all endmember reduction technique for Multiple Endmember Spectral Mixture Analysis (MESMA). Total models represents the number of models need to run four endmember MESMA.

Class	EMC	uSZU EMC	In-CoB	uSZU In-CoB	IES	uSZU IES	Reduced IES	uSZU Reduced IES
Char	2	3	5	5	10	10	5	7
GV	2	2	14	17	31	42	25	40
NPV	3	2	11	11	36	40	32	37
Soil	2	2	15	16	55	53	35	38
Total Models	83	83	5,729	7,071	115,543	156,821	45,327	92,415
Processing Time	0.98	0.44	14.88	8.70	151.85	66.76	78.36	54.45

2.3.3. Unmixed Images and Overall Model Comparison

The eight endmember libraries produced broadly similar patterns (Figure 2.5). The EMC method without band selection stands out as modeling more NPV than the others, notably modeling NPV in areas that other approaches modeled as GV. Unmixed images generated from libraries without uSZU band selection appear to have slightly more NPV than their uSZU counterparts, but otherwise give similar results.

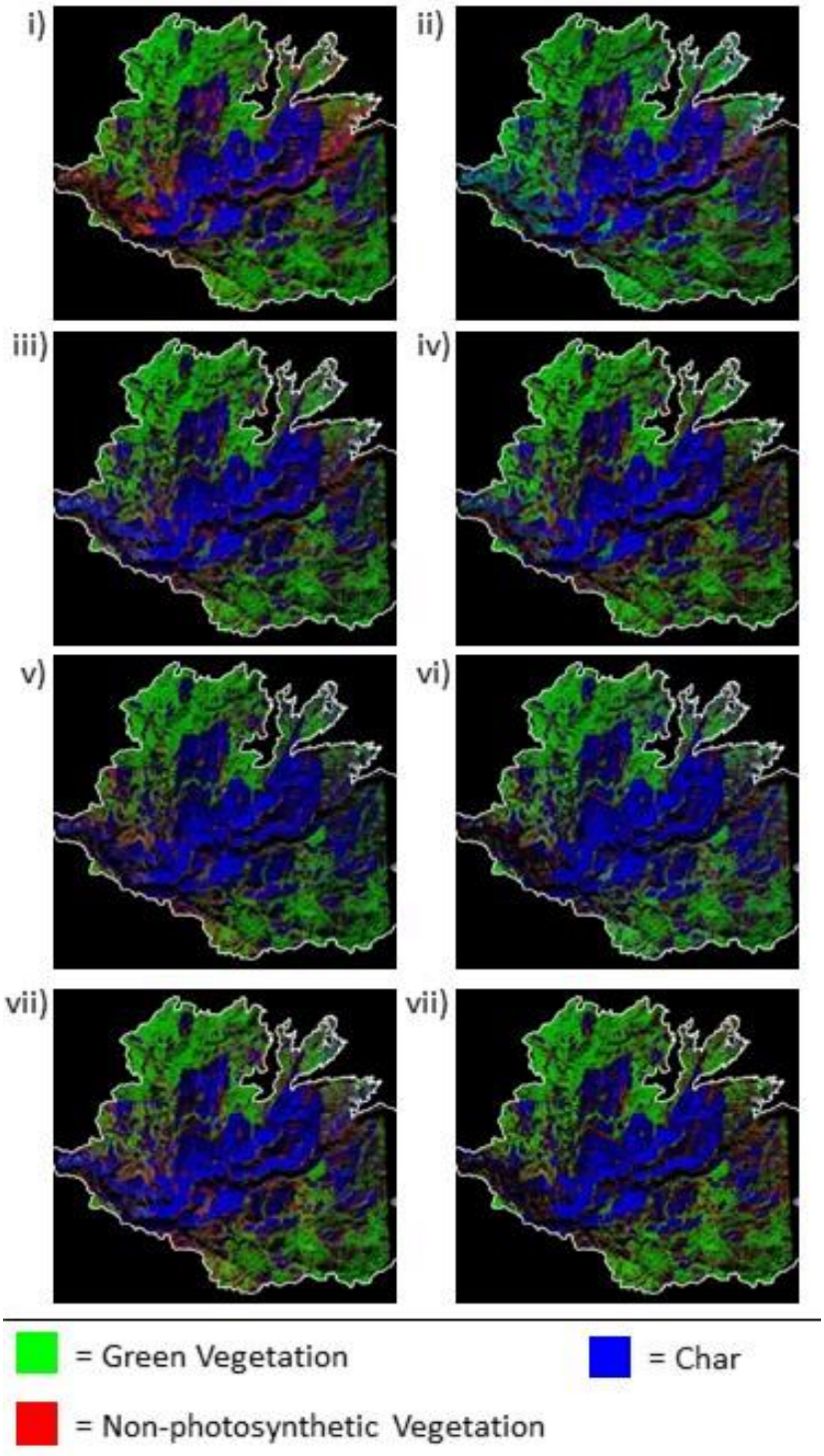

Figure 2.5. MESMA cover fraction images within the Rim Fire burn scar, soil cover is not shown in the image series. The boundary of the Rim Fire is represented by a white line. Black indicates areas that were not classified or only had soil cover. Endmember selection and band selection techniques are as follows: i) EMC, ii) uSZU EMC, iii) In-CoB, iv) uSZU In-CoB, v) IES, vi) uSZU IES, vii) Reduced IES, viii) uSZU Reduced IES.

While the models were qualitatively similar, there were quantifiable differences between them (Table 2.3). The number of pixels successfully modeled, defined by the number of pixels where any endmember combination tested by the MESMA algorithm resulted in an RMSE below the threshold of 0.025, ranged from 79.1% of the fire area (uSZU In-CoB) to 93.0% of the fire area (IES). Soil was the most variable endmember class between the models, with one scene containing as few as 7.5% of pixels with any modeled soil cover (uSZU EMC) to 41.8% of pixels (IES). Char and GV were the most commonly modeled endmember classes with between 36.9 - 53.1% of pixels containing char and between 35.3 - 54.1% of pixels containing GV.

Table 2.3. Percent of total pixels within the Rim Fire boundary that were successfully modeled and the percent of pixels containing each endmember class for various endmember selection techniques. In total, approximately 7,850,000 pixels within the Rim Fire boundary were considered. A single pixel was allowed to contain up to three endmember classes (not including shade).

	EMC	**uSZU EMC**	**In-CoB**	**uSZU In-CoB**	**IES**	**uSZU IES**	**Reduced IES**	**uSZU Reduced IES**
Modeled	87.0%	81.7%	83.2%	79.1%	93.0%	92.0%	85.7%	86.4%
Char	36.9%	53.1%	47.3%	36.9%	33.4%	42.9%	41.6%	34.4%
GV	54.1%	52.9%	43.1%	39.9%	35.3%	39.4%	36.8%	38.1%
NPV	38.8%	21.9%	27.7%	22.0%	23.5%	21.2%	30.0%	21.65
Soil	7.9%	7.5%	11.5%	26.2%	41.8%	28.6%	17.5%	28.4%

2.3.4. Endmember Sources in Model Selection and the Image

Most spectral libraries selected endmembers from all sources (Table 2.4). In the initial spectral library, a majority of spectra were derived from AVIRIS imagery, however, a disproportionally small amount of spectra from this source were selected by most endmember reduction techniques. This suggests that, by the metrics used by the endmember reduction techniques, most image derived spectra were redundant and were therefore eliminated. In contrast, spectra created in Wind River (Roberts et al., 2004) were disproportionally retained by most endmember selection techniques. This indicates spectra from that source were generally distinct from other spectra included in the initial spectral library.

Table 2.4. The source of endmembers for each endmember reduction technique.

Spectra Source	EMC	uSZU EMC	In-CoB	uSZU In-CoB	IES	uSZU IES	Reduced IES	uSZU Reduced IES
AVIRIS	9	9	15	18	41	45	20	30
ASD	0	0	5	4	12	14	9	12
Wind River	0	0	25	27	79	86	68	80

When spectral libraries were used to model cover fractions across the Rim Fire, spectra generated from the AVIRIS images were disproportionally selected, given their abundance in the reduced spectral libraries (Table 2.5). All spectral sources were used to some degree. It should be noted that not all endmember classes modeled in this study were collected for each spectral source and there were large differences in the number of spectra collected for each source.

Table 2.5. Percentage of pixels modeled by source for each endmember reduction technique. A single pixel can be modeled by multiple different sources, resulting in totals that exceed 100%.

Spectra Source	EMC	uSZU EMC	In-CoB	uSZU In-CoB	IES	uSZU IES	Reduced IES	uSZU Reduced IES
Not Modeled	13%	18.3%	16.8%	20.9%	7%	8%	14.3%	13.6%
AVIRIS	87%	81.7%	42.1%	53.2%	61.8%	55.3%	48.6%	32.5%
ASD	0	0	15.7%	6.2%	5.4%	10.3%	6.9%	26.4%
Wind River	0	0	45.8%	38%	47.1%	44.4%	47.6%	41.6%

2.3.5. Validation

2.3.5.1. WorldView-2 Based Validation

The classified WorldView-2 imagery and the AVIRIS-based MESMA cover fractions were compared using the 120 randomly selected polygons across the two image types (Table 2.6). The best linear correlations between WorldView-2 fractions and MESMA were observed for the GV cover, which displayed a near 1:1 relationship and had generally high r^2 values regardless of the endmember selection technique used. Correlation coefficients for char were generally fairly high (between 0.59 - 0.741), however, all models showed a tendency to under-model char, as demonstrated by linear models consistently having an intercept above 0.2. Correlations were generally poor for NPV and soil, with r^2 values often below 0.2. Larger endmember libraries did not always translate to higher fractional cover accuracy; for example, the highest r^2 for the char fraction was found for the uSZU EMC library (0.741).

Table 2.6. The coefficient of determination (r^2), intercept, and slope value of a linear fit between WorldView-2 estimated cover fractions as the dependent variable and AVIRIS derived MESMA cover fraction for different endmember and band selection techniques as the independent variable. Green vegetation is abbreviated as GV, non-photosynthetic vegetation as NPV.

		EMC	**uSZU EMC**	**In-CoB**	**uSZU In-CoB**	**IES**	**uSZU IES**	**Reduced IES**	**uSZU Reduced IES**
Char	r^2	0.605	0.741	0.727	0.642	0.620	0.538	0.687	0.594
	Intercept	0.355	0.303	0.212	0.202	0.321	0.223	0.255	0.310
	Slope	0.721	0.755	0.841	0.835	0.765	0.783	0.771	0.750
GV	r^2	0.750	0.770	0.836	0.871	0.848	0.846	0.853	0.861
	Intercept	-0.054	-0.023	-0.026	-0.065	0.020	0.000	-0.010	-0.019
	Slope	0.653	0.769	0.708	0.675	0.895	0.812	0.804	0.748
NPV	r^2	0.086	0.099	0.164	0.249	0.209	0.237	0.165	0.245
	Intercept	0.110	0.103	0.109	0.126	0.099	0.107	0.099	0.094
	Slope	0.240	0.521	0.426	0.375	0.968	0.943	0.377	0.699
Soil	r^2	0.273	0.261	0.088	0.042	0.014	0.049	0.075	0.057
	Intercept	0.013	0.015	0.015	0.013	0.019	0.016	0.011	0.012
	Slope	0.641	0.102	0.222	0.965	0.041	0.088	0.2	0.103

Plots of the linear regression for the uSZU IES MESMA run and the WorldView-2 classifications are provided below (Figure 2.6). The plots are broadly representative of the trend of most MESMA versus WorldView-2 relationships. There is general support for the linear relationship of the GV identification by MESMA and the WorldView-2, with a high r^2 value and little systematic error. Based on the manual interpretation of the WorldView-2 imagery, MESMA appears to be systematically modeling a lower fraction of NPV and char cover, and modeling a higher fraction of soil cover.

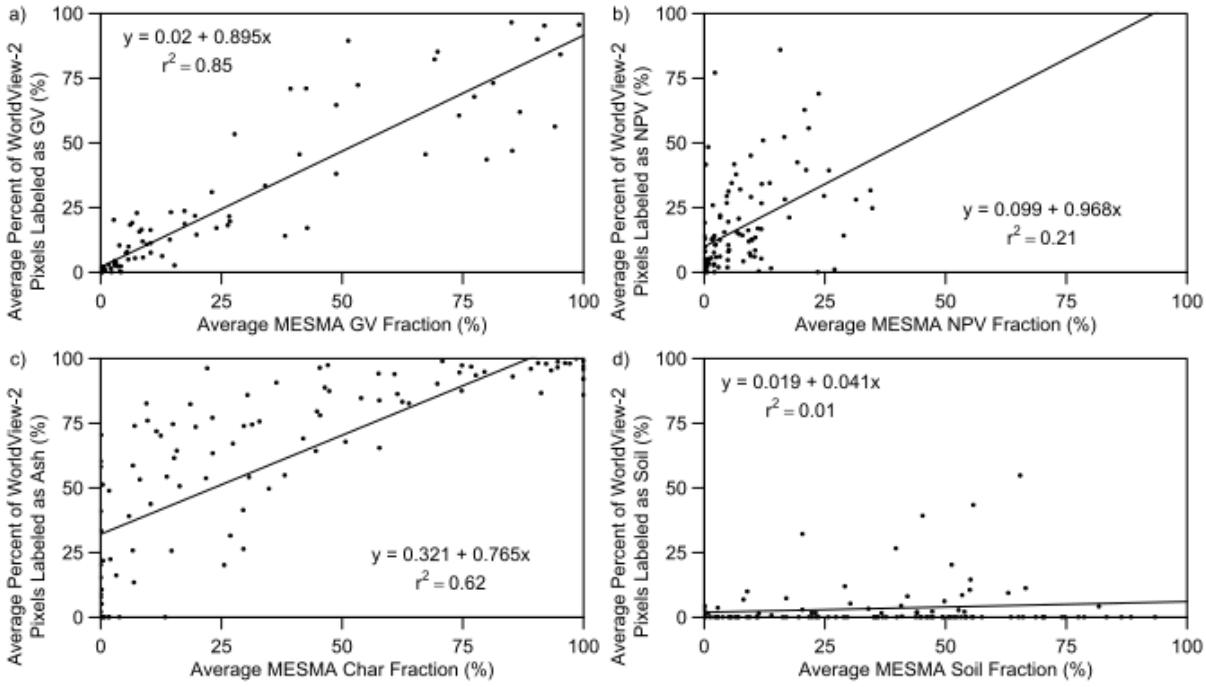

Figure 2.6. Scatter plots of the relationship between the 120 WorldView-2 classification points and MESMA with the IES endmember selection technique for green vegetation (GV), char, non-photosynthetic-vegetation (NPV), and soil.

2.3.5.2. Comparison with GeoCBI Plot Data

Due to the similarity between MESMA unmixed models used in this study, I limit my comparison to only the cover fractions generated from MESMA using the IES library and the full AVIRIS bands. First, the relationship between individual cover fractions and GeoCBI was assessed (Figure 2.7). The relationship between the GV fraction and GeoCBI appeared to be inversely linear (a linear regression produced an intercept of 2.93, a slope of -1.89 and r^2 value of 0.644). In contrast, the relationship between NPV and GeoCBI is clearly non-linear. NPV fractions are generally highest at GeoCBI values of 1.5 to 2.5 suggesting that NPV is high at moderate severities, but low at the highest and lower severity levels. The char fraction appears to be more of a binary relationship only appearing in the model at the highest GeoCBI levels (above 2.75) and is at or near zero for all other GeoCBI levels.

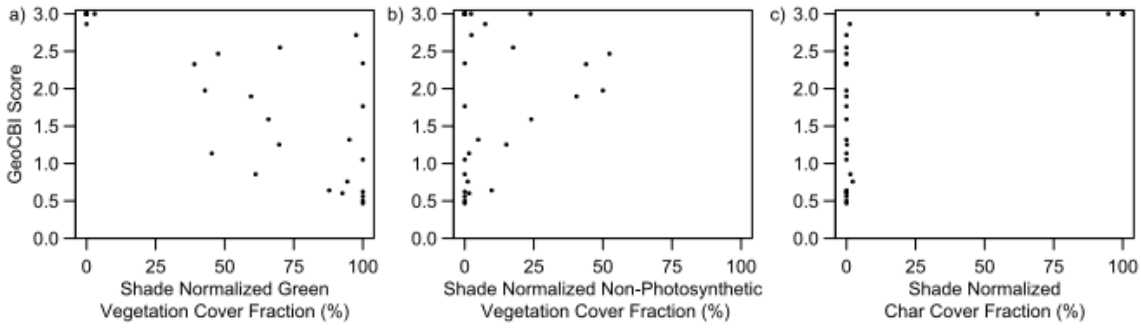

Figure 2.7. Scatter plots of the relationship between GeoCBI, a ground plot derived method of measuring fire severity and estimated cover fractions for green vegetation, non-photosynthetic vegetation, and char.

2.3.5.2. Comparison with Field Tree Status Data

I also compared the MESMA cover fractions of GV, NPV, and char with the percentage of canopy level trees with mostly green, brown, and black needles (Figure 2.8). Similar to the GeoCBI values, the char percentage and percentage of black trees appeared to have a near binary relationship in the plots. If the percentage of field identified black trees within the plot was under 50%, then typically no char fraction was modeled for the pixel, if it was above 50%, then the char fraction was almost always modeled as close to 100%. The relationship between the brown trees and NPV appeared to generally be more linear, although the modeled NPV cover was never greater than 50% even with near 100% brown trees. The relationship between the green trees and green vegetation may be positively linear, but the amount of scattering makes interpretation difficult. It is important to remember that few AVIRIS pixels are purely tree cover, most are a mixture of tree and substrate, so a pixel with 100% brown trees may indeed be made up of 50% other materials. Finally, it is important to note that the percent of trees in the plot may not be an ideal reference for the cover fraction as it does not account for variation in tree density, and this may partially contribute to the observed biases.

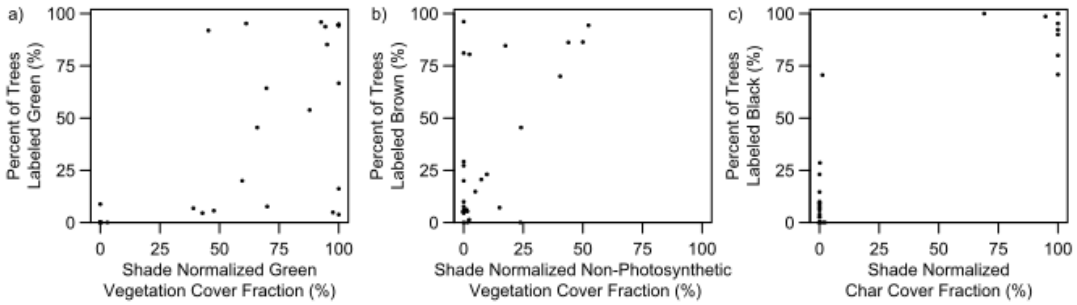

Figure 2.8. Scatter plots of the relationship between percent of black, brown, and green trees, and estimated cover fractions for green vegetation, non-photosynthetic vegetation, and char.

2.4. Discussion

2.4.1. Potential Bias and Uncertainty in the Cover Types

Whereas previous studies found the relationship between the char fraction and GeoCBI to be linear (Veraverbeke et al., 2014; Veraverbeke and Hook, 2013) this was not the case in this study. The GV fraction retrieval by MESMA, was found to be linear, however. GV's high accuracy is likely due to both the spectral separability and the temporal persistence of the class. In contrast to GV, at the spectral resolution of WorldView-2 soil, NPV, and ash were all somewhat difficult to separate. Human interpretation likely reduced inter-class confusion in classifying the WorldView-2 imagery, but this was still a source of error associated with the WorldView-2 image classification. In particular, separation of the soil and ash areas was particularly difficult with the WorldView-2 imagery. This is partially because of insufficient spectral information and partially because even at 2 m pixel resolutions, many pixels were likely a mixture of mostly ash with some soil. This mixture would impact the spectral signal, and therefore be reflected in the MESMA generated cover fractions, but these areas were generally just classified as ash in the manual interpretation of the WorldView-2 image. Another possible factor in diminished char is the amount of time between when the fire burned the area of the GeoCBI plots, which was in late August and

early September (evaluated from fire spread map in Peterson et al. 2015a), and image acquisition, which was 28 September for the WorldView images and 17 November for AVIRIS. During the time period between the fire occurring and AVIRIS image acquisition, there were four rain events totaling 64.8 mm at a weather station in Groveland, CA (data accessed from http://www.ncdc.noaa.gov/cdo-web/datasets#GHCNDMS) within 20 km from where the field plots were collected. Combined with wind, rain likely attenuated the ash portion of the char signal. The impact of weather, combined with other previously mentioned factors, likely account for why char was more prevalent and soil less prevalent in the WorldView-2 classification than the MESMA cover fraction (Figure 2.6).

2.4.2. Evaluation of MESMA Techniques' Performance

The balance of library complexity with accuracy must be considered if MESMA is to be used on spaceborne imaging spectroscopy at regional to global scales for ecological monitoring (Veraverbeke et al., 2014). Schaaf et al. (2011) and Roth et al. (2012) have shown IES endmember selection produces high classification accuracy in the two endmember MESMA case. However, IES selected the most endmembers in its final spectral library in my study and when compared to other methods in Roth et al. (2012). In this study, regardless of the technique used to generate cover fractions, the more spectrally unique classes (GV and ash) had approximately similar performances when compared with the WorldView-2 cover fractions. Using uSZU In-CoB to generate MESMA cover fractions produced relatively high r^2 values when compared to WorldView-2, even though the number of endmembers used and processing times were significantly less. That a variant of In-CoB would perform as well as IES is not consistent with Roth et al. (2012). One possible explanation for this is that when using endmembers for classification of vegetation types, as

was done in Roth et al. (2012), some degrees of mixture within endmembers, particularly with soil and NPV, is necessary for accurate classification across a landscape. If endmembers within the endmember classes of the starting library are to some degree mixed, in order maximize kappa IES will tend to select mixed pixels. However, when using MESMA for spectral unmixing to estimate cover fractions, as was done in this study, the purest endmembers will obtain the highest accuracy.

The margin of computational efficiency created by uSZU, a 30 - 50% reduction in processing times, was similar to Somers and Asner (2013). However, unlike Somers and Asner (2013), I did not observe a clear trend of increased accuracy (Table 2.6). In Figure 2.5 and Table 2.3, it is clear that the techniques that used uSZU generally mapped less NPV than techniques that did not. Spectral regions that are critical for the separation of soils and NPV due to their association with lignin and cellulose absorption, such as the 2300 – 2400 nm region (Daughtry, 2001), did not get selected by uSZU (Figure 2.4). Many of the bands which were selected appear associated with atmospheric noise. In Veraverbeke et al. (2014) bands were reduced to similar numbers as the uSZU, however they were not selected in a way that was designed to maximize differences between endmember classes, resulting in a much larger decrease in accuracy than was observed here. Future studies should investigate other band selection techniques and the optimal bands for the simultaneous separation of GV, NPV, soils, and ash.

2.4.3. Endmember Sources and Endmember Selection

Beyond pre-processing, another challenge to SMA becoming a global means of objective comparison is determining a proper base spectral library. Studies have shown the timing of the acquisition of the base spectra and the image is important (Dudley et al., 2015),

as is the spatial scale that the spectra were acquired (Roberts et al., 2012, 2004). It is notable that spectra collected in a different spatial location than the images and at different spatial scales than the images, were frequently selected to model cover fractions. This suggests that a common spectral library could be developed to map fire across at least a regional scale. It also suggests that even in environments not composed of as many complex materials as the urban (Franke et al., 2009; Herold et al., 2003; Roberts et al., 2012), a diversity of spatial scales may be beneficial to cover fraction mapping.

Although, impurity of endmembers collected in non-laboratory settings is inevitable, it is a particular challenge at the spatial scale of AVIRIS or proposed spaceborne imaging spectrometers. It is notable that the endmember classes which it is most difficult to get pure pixels from images, NPV and soil (that was not exposed rock), also appeared least accurate. Although spectra collected in the field were included in my spectral library, these may not perfectly scale to the canopy level AVIRIS observations (Roberts et al., 2004). AVIRIS – Next Generation (AVIRIS-NG; Hamlin et al. 2011) poses a potential means for overcoming some of these challenges (Roberts et al., 2017). The superior spatial and spectral resolutions allows for collecting and evaluating endmembers that are closer to being pure while still being collected at the canopy-scale of AVIRIS.

2.4.4. SMA as a Novel Means for Assessing Fire Severity

Since properly identified cover fractions have physical meaning, they have the potential to be an objective and global means of assessing fire severity. Cover fractions, if shown to be accurate and comparable to field derived fire severity estimates, have the potential to overcome many of the criticisms of NBR-based indices (Cansler and McKenzie, 2012; Lentile et al., 2009, 2006; Morgan et al., 2014). With the potential launch of several

spaceborne imaging spectrometers, and considering the demonstrated higher correlations of SMA with imaging spectroscopy data compared to broad-band data (Veraverbeke et al., 2014), the use of SMA for fire may increase in the future. Since the variation of soil and GV's spectral profile across space is one of the key reasons for NBR's subjectivity, if SMA is going to become an important means of assessing burn severity, endmember variability must be accounted for, and MESMA is one of the most reliable technique for doing so (Somers et al., 2011). In this study, only a single fire is included in the study area; however, if SMA is to become a commonly used tool for fire severity assessment, a global assortment of geographic locations and their spectral variability will need to be tested and compared. As imaging spectroscopy data becomes more common, both through more airborne and spaceborne acquisitions, global assessment will become viable.

One possibility for assessing change using SMA is using a differenced SMA (dSMA) approach. By using dSMA the entirety of the information provided by MESMA classes could be used, potentially providing a robust and more ecologically meaningful method of evaluating fire severity. However, this approach would have an inherent disadvantage of all differenced imagery comparisons, in that relatively analogous pre-fire imagery would be needed. Since all imaging spectroscopy data with signal-to-noise ratios and spectral and spatial resolutions similar to AVIRIS are currently acquired from airborne platforms, pre-fire data is rare; however proposed spaceborne imaging spectrometers such as HyspIRI and ever-increasing computational power would make this analysis possible at regional to global scales. Future studies evaluating dSMA usefulness in fire severity evaluation will require careful planning in field validation plot placement to assure that plots are placed in areas that pre-fire were heterogeneous in terms of type and percentages of vegetation cover. Given the

relative accuracy of mapping the GV cover class, using a differenced GV cover fraction (dGV) is likely to have high correlation with the field measures of burn severity. In addition, the high correlation observed for the char cover type, suggests that adding a post-fire char cover to a dGV assessment could further enhance the discrimination of burn severity.

2.5. Conclusions

I demonstrated the utility of imaging spectroscopy combined with MESMA for fire severity mapping over a large fire in California's Sierra Nevada. While currently limited to airborne acquisitions, future spaceborne missions will allow large-scale application of these techniques. One aspect that will be important for processing imaging spectroscopy and MESMA globally are techniques that maximize accuracy while minimizing calculation time. In this study, I performed MESMA using a spectral library that included several different collection methods and multiple different spatial scales. I demonstrated that band reduction can significantly reduce computational time with only small differences in performance. I also evaluated the performance of several endmember selection techniques and found that these can also be optimized between performance and calculation time. Further research is needed that evaluates cover fractions relation to fire severity comparing multiple fires across regions. However, the identification cover fractions represents a potentially objective and physically meaningful evaluation of fire severity using remote sensing.

Chapter 3: A Framework for Detecting Conifer Mortality across an Ecoregion using High Spatial Resolution Spaceborne Imaging Spectroscopy

Zachary Tane[1,2], Dar Roberts[1], Alexander Koltunov[2,3], Stuart Sweeney[1], Carlos Ramirez[2]

[1]University of California Santa Barbara, Department of Geography

[2]United States Department of Agriculture, Forest Service, Pacific Southwest Region, Remote Sensing Lab

[3]Univesity of California Davis, Center for Spatial Technologies and Remote Sensing (CSTARS), Department of Land, Air, and Water Resources

This chapter is based on a manuscript that is currently in press in the journal *Remote Sensing and the Environment.*

3.0. Abstract

Between 2013 and 2015, during a time of severe drought and elevated bark beetle (*Dendroctonus spp.*) activity in California, the amount of conifer mortality in the Southern Sierra Nevada increased greatly. Remote sensing is a critical means of providing up-to-date information on the location, magnitude, and extent of mortality across a broad geographic area. We used eleven Airborne Visible / Infrared Imaging Spectrometer (AVIRIS) flight lines, resampled to 30 by 30 m pixel size and acquired on six separate dates as part of the HyspIRI Preparatory Campaign to simulate spaceborne imaging spectroscopy. We also spectrally degraded the AVIRIS images to simulate Landsat-8 data. We tested the ability of single-date and multi-temporal remote sensing to identify red stage conifer mortality, healthy conifer, and non-conifer dominated pixels using a random forest algorithm. Accuracy was assessed with an independent validation dataset acquired via WorldView imagery in areas spatially separate from where training data were collected, as well as through comparison with aerial detection survey and canopy water loss data, with generally good agreement. We found that classifications based on imaging spectroscopy significantly outperformed broadband multispectral feature sets (with a highest overall accuracy of 85.1% obtained by imaging spectroscopy and 80.2% obtained by the simulated multispectral images). We also found that classifications based on multi-temporal imaging spectroscopy were more accurate than single-date imaging spectroscopy (the highest overall accuracy obtained for single-date imaging spectroscopy was 83.4%). Imaging spectroscopy that included interseasonal data from the end of the drought outperformed all other datasets, including interannual data that included only images collected in the summer. Multi-date analysis also improved accuracy using broad band systems. Although current spaceborne

assets are adequate for monitoring bark beetle mortality in a heterogeneous ecosystem, a spaceborne imaging spectrometer would further improve operational accuracy.

3.1. Introduction

Between the hydrological years of 2012 and 2015, California has been subject to one of the worst droughts in the past several centuries (Diaz and Wahl, 2015). One of the most prominent effects of this drought has been an increase in tree mortality in the Southern Sierra Nevada, prompting California to declare a state of emergency on 30 October 2015. In the Western United States, one of the primary vectors of mortality in conifers during drought is native bark beetles killing weakened pines (*Pinus spp.*; Raffa et al., 2008). The effect of bark beetles and subsequent tree mortality on ecosystem services and function (Edburg et al., 2012), fire and fuels (Jenkins et al., 2008), economics (Waring et al., 2009), recreation and scenery (Sheppard and Picard, 2006), public safety, and property values (McGregor and Cole, 1985) has been well documented.

Given that bark beetle driven mortality is generally widely dispersed, remote sensing is an important method for helping to understand the spatial extent, magnitude, and ecological effects of these outbreaks (Wulder et al., 2006). Generally, bark beetle mortality in conifers is broken up into four stages, each with distinct physical and spectral properties. The first stage, healthy vegetation, is the stage all conifers are in before a successful attack. The next stage, green attack, occurs after bark beetles have successfully attacked a tree, but before the tree's needles show visible signs of leaf color change (Wulder et al., 2006). In this stage, the tree is unable to transport nutrients from the roots to the needles and is therefore effectively dead. Six to twelve months after an attack, trees transition to the red stage, wherein all needles on a tree turn visibly red (Wulder et al., 2006). Finally, two to five years after an attack, the tree transitions into the gray stage, where most or all of a tree's needles have fallen to the canopy floor and only the gray branches remain. Each of these stages has

unique spectral shifts associated with them; however, in some cases, the changes in reflectance between phases are small and only over a small wavelength range (Ahern, 1988; Wulder et al., 2006).

A variety of remote sensing data sources have been used to identify effects of epidemic insect outbreaks. Sensors in the Landsat series have the advantage of a large field of view (FOV), which allows for inexpensive imaging of entire ecoregions repeatedly through time. However, the inherent physical tradeoff of this is a larger pixel size, which in heterogeneous ecosystems results in pixels that are almost always mixtures. Mixed cover pixels make it difficult to separate the target spectral signal (needle senescence and loss in conifers) from background spectral changes, e.g. leaf physiological changes in understory or non-target crown level vegetation. Often, this problem is either overcome by limiting the identification to a pre-defined homogenous target area (White et al., 2007) or by collecting airborne or satellite imagery at finer spatial resolutions and therefore with potentially fewer mixed pixels (Lausch et al., 2013). Both of these methods have limitations in their ability to monitor whole ecoregions, particularly in a cost-effective manner.

Spaceborne imaging spectroscopy, where reflectance is continuously sampled at narrow spectral intervals, could provide sufficient resolution over a wide enough spectral region to identify different cover types and their relative spectral contributions within a pixel (Roth et al., 2012; Ustin and Gamon, 2010; White et al., 2007). With the proper sensor, spaceborne imaging spectroscopy could provide the large FOV necessary for operational ecoregion monitoring, while partially overcoming the problem of mixed pixels intrinsic to a large pixel size. Currently, most research related to imaging spectroscopy and bark beetles has focused on identifying green attack trees at the fine spatial resolutions provided by aircraft platforms

(Fabian E. Fassnacht et al., 2014; Lausch et al., 2013; Niemann et al., 2015; Pontius et al., 2005; White et al., 2007). Research on the operational ability of spaceborne imaging spectroscopy to identify red stage mortality has not occurred because it would require a satellite that could collect large FOV images at a global scale with repeat sampling, a high signal-to-noise ratio, and sufficiently small pixel size— no instrument that meets these specifications currently exists. However, several instruments have been proposed, including HyspIRI (Lee et al., 2015). The National Aeronautics and Space Administration (NASA) JPL's HyspIRI Preparatory Campaign provides a unique surrogate for spaceborne imaging spectroscopy. Although the campaign was conducted with AVIRIS, several factors allow it to be analogous to a spaceborne platform for research purposes. These factors include contiguous flightlines acquired over large geographic regions that allow for ecoregion-level monitoring; three seasonal acquisitions flown over a three year period, starting before the widespread tree mortality event, thereby providing a data set that makes time series analysis and change detection possible; and algorithms that have been developed to simulate the signal-to-noise ratio and spatial resolution of the proposed HyspIRI mission (Thompson et al., 2015).

Both single-date and multi-temporal classifications have been shown to produce highly accurate separation between healthy and red stage conifer pixels with multispectral imagery; for example, over 90% accuracy for both temporal paradigms was obtained in Meddens et al. (2013). Largely due to a lack of data availability, multi-temporal imaging spectroscopy studies are uncommon (Dennison et al., 2003; Niemann et al., 2015; Roberts et al., 1997; van Wagtendonk et al., 2004). Given imaging spectroscopy's capability for accurate identification of plant functional types (Ustin and Gamon, 2010), multi-temporal imaging

spectroscopy could identify pre-disturbance plant functional units in order to better understand disturbance dynamics. However, using multi-temporal images introduces additional constraints and sources of error. These include the need for continuous acquisition of cloud-free images through time, sensitivity to co-registration errors, and the potential bi-directional reflectance distribution function (BRDF) differences between dates (Chuvieco and Huete, 2009).

In this chapter, I test the ability of imaging spectroscopy to identify red stage mortality. Specifically, I generate several reference datasets and examine the effectiveness of imaging spectroscopy versus multispectral data, multispectral versus single-date information sources, and the importance of feature reduction. I also assess which spectral regions are most effective for red stage mortality identification. Finally, I compare the imaging spectroscopy based maps of red stage mortality to other tree mortality data sources, thus providing greater context to my classification results.

3.2. Methods

3.2.1. Study Area

The study occurred in montane forests on the western side of the Sierra Nevada in California, USA. All areas that met the following criteria were considered part of this study: 1) Areas consistently imaged by the AVIRIS instrument between Spring 2013 and Summer 2015 as part of the HyspIRI Preparatory Campaign, South Sierra flight box; 2) Areas on publically owned National Forest or National Park land (the land management history of privately owned lands during and before this study could not be easily retrieved and these areas were therefore excluded); 3) Areas below 2,100 m of elevation, in order to focus primarily on areas with a major ponderosa pine component; 4) Areas that had not been

mechanically thinned between Spring 2013 and Summer 2015 as determined by the Forest Service Activity Tracking System (FACTS); 5) Areas that had not burned in a controlled fire or wildfire between Spring 2013 and Summer 2015, which was also determined by FACTS. Approximately 339,000 hectares met these conditions (Figure 3.1).

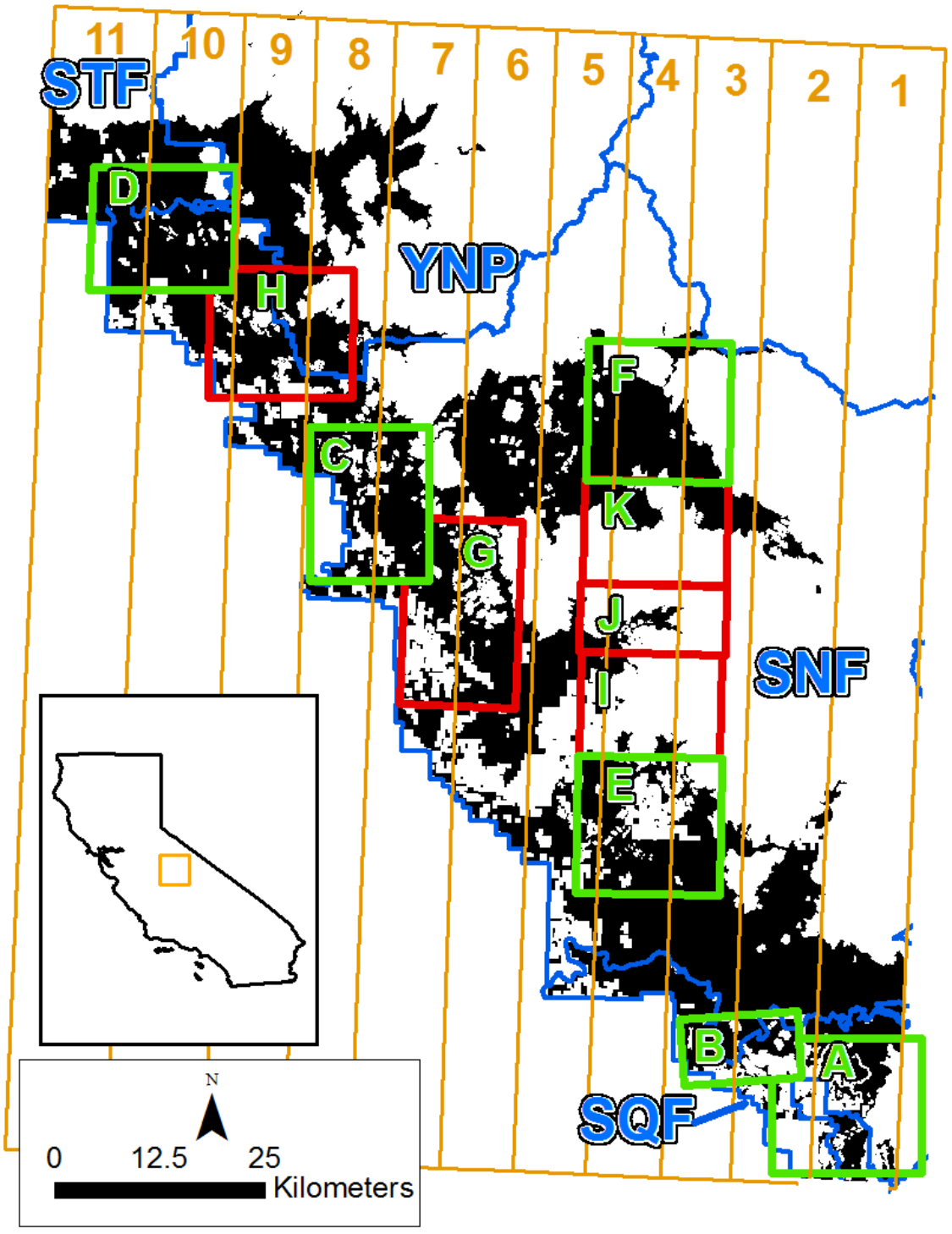

Figure 3.1. The study area, located in the Sierra Nevada, in California, USA is shown in black. Airborne Visible / Infrared Imaging Spectrometer (AVIRIS) imaged areas that were part of the southern Sierra flight box are shown in orange. The individual flight lines have been stylized to not display the areas of overlap between flight lines and the northern and southern borders of the AVIRIS flight lines have been clipped for image clarity. The orange numbers correspond with the individual AVIRIS flight line number. The individual footprints of WorldView 2 and WorldView 3 scenes used to collect training data and validation data are displayed in green and red, respectively. The following acquisition date corresponds with each letter: A- 25

March; B- 5 April, 2015; C- 6 May, 2015; D- 22 June, 2015; E- 14 July, 2015; F- 14 July, 2015; G- 6 May, 2015; H- 25 June, 2015; I- 14 July, 2015; J- 14 July, 2015; K- 14 July, 2015. The relevant national forest and national park boundaries are displayed in blue, the acronym meanings are SQF – Sequoia National Forest; SNF – Sierra National Forest; YNP – Yosemite National Park; STF – Stanislaus National Forest.

The climate of the study area is Mediterranean, typically consisting of hot dry summers and cool wet winters. The study area is comprised of a variety of different vegetation assemblages (Holland and Keil, 1996). At the lower elevations, there are montane hardwood species such as blue oak, valley oak, interior live oak, and California buckeye. Also present at these elevations are annual grasslands and shrublands composed of species such as manzanita and California lilac. At around 1000 m above sea level, conifer communities, often dominated by ponderosa pine, are widespread. At higher elevations within the maximum elevation of 2100 m in my study area, conifers are often a mixed assemblage of ponderosa pine, white fir (*Abies concolor*), sugar pine (*Pinus lambertiana*), and incense-cedar (*Calocedrus decurrens*). Conifers are comprised of a variety of densities, age cohorts, and sizes throughout the study area.

As previously stated, during the time period of the study, the region was experiencing intense drought. United States Forest Service aerial detection survey data indicates that, during the summer of 2015, red stage tree mortality was highly elevated from baseline levels (USFS, 2016). By the summer of 2016, after the time frame of this study, the mortality had dramatically spread and intensified.

3.2.2. Input Data

As part of the HyspIRI field campaign, AVIRIS data were collected over the southern Sierra Nevada during the spring, summer, and fall seasons for three years starting in 2013 through 2015. Additional data were also collected in summer 2016. In this study, the aim was to characterize red stage mortality in the summer of 2015, so the fall 2015 and summer

2016 AVIRIS flights were not used. Most of the flight lines in fall 2013 were found to have smoke contamination from the 2013 Rim Fire and a great deal more snow was present in spring 2014 than any other date, thus both dates were excluded further processing. Imagery from the following six dates were used: 3 May 2013, 12 June 2013, 3 June 2014, 6 October 2014, 5 May 2015, and 1 June 2015. In this chapter, images acquired on these dates will be referred to as spring 2013, summer 2013, summer 2014, fall 2014, spring 2015, and summer 2015, respectively. On each date eleven flight lines were imaged, therefore, in total, 66 AVIRIS flight lines were used in this study (Figure 3.1). The images were accessed from NASA's JPL servers after the following preprocessing steps were performed by JPL: the images were converted from radiance to Level 2 reflectance using the ATREM algorithm, resampled to 30 X 30 m pixel size, and degraded with a signal-to-noise ratio that is analogous to HyspIRI (Thompson et al., 2015). The reflectance products have previously been validated with high reflectance targets and found to be well calibrated (Thompson et al., 2015), although cross-track illumination differences between different flight lines are still present. Bands at wavelengths 365-405 nm, 1325-1420 nm, 1810-2040 nm, and 2450-2500 nm were discarded either because they are known to be associated with atmospheric water vapor absorption or were found to contain significant atmospheric artifacts and a low signal-to-noise ratio, based on visual inspection. This left 177 AVIRIS bands per date for use in the analysis.

After retrieval, the images went through several pre-processing steps before being used as class-separating input variables (often termed features) in a classification algorithm (Figure 3.2). Since clouds were relatively rare (only appearing rarely in spring and summer 2015), clouds and cloud shadows were manually masked and excluded from further

analysis. Although Level-2 AVIRIS images obtained from JPL are georeferenced, it is not uncommon for them to have significant spatial misalignment between dates (Khanna et al., 2013). In my study area, the images I obtained from JPL had apparent pixel displacements that routinely exceeded 2 pixels (60 m). However, analysis of subpixel scale changes in heterogeneous pixels required subpixel registration across time. Therefore, I applied an automated image registration method (Koltunov et al., 2012) that combines robust band-wise compensation for radiometric differences (Koltunov et al., 2008) with iterative intensity gradient-based alignment (Irani, 2002). After registration, the residual misalignment was estimated to be within half a pixel (15 m). WorldView (DigitalGlobe) images used in this study were also registered to the AVIRIS images, using manually identified tie points. The resulting overall co-registration accuracy between the AVIRIS and WorldView images was also less than half a pixel.

When pixels are composed of multiple cover types, a common way of estimating their relative contributions is by using SMA (Adams et al., 1986). Cover types, often referred to as endmember classes, of GV, NPV, and soil, were deemed important for mortality identification for this study (Roberts et al., 1993). In order to account for within-class variability, MESMA, where the individual spectra representing each class were allowed to vary on a per-pixel basis, was used (Roberts et al., 1998). MESMA has been shown to be a robust solution to the endmember variability problem in a wide variety of contexts (Somers et al., 2011).

In this study, a spectral library of endmembers was created from AVIRIS-NG (Hamlin et al., 2011) data collected over the study area. AVIRIS-NG is also an airborne full range imaging spectrometer similar to AVIRIS, but with several improvements, including a higher

signal-to-noise ratio, and 5 nm sampling interval resulting in twice as many bands. The data used were of sufficiently high spatial resolution (1-2 m on a side) to enable manual identification of pure pixels for each cover type. I subsequently convolved the collected spectra to AVIRIS-classic spectral resolutions. In order to decrease processing times and increase MESMA accuracy, I reduced the number of input bands uSZU (Somers and Asner, 2013). The MESMA spectral library was reduced using a CoB approach (Roberts et al., 2003). Four-endmember MESMA (a maximum mixture of all three endmember classes and shade) was performed on the AVIRIS flight lines for all time steps using ENVI/IDL 5.2 (Environment for Visualizing Images, Harris Geospatial, Broomfield, CO) with the VIPER Tools 2 software add-on package. Next, I divided the estimated fractions of first three classes by the shade fraction, thus adjusting these fractions for shade contribution (Adams and Gillespie, 2006).

To correct the reflectance bands for inherent BRDF differences between flight lines collected on different dates, at different times of the day, and over varied terrain, I applied a continuum removal (Clark and Roush, 1984) method implemented in Exelis's ENVI/IDL 5.2 (Environment for Visualizing Images, Harris Geospatial, Broomfield, CO). In continuum removal, the convex hull is fit over the entire spectrum and the reflectance value is divided by the convex hull value at that wavelength. In addition to normalizing brightness differences, continuum removal also enhances subtle spectral absorption features associated with foliar biochemistry (Niemann et al., 2015; Youngentob et al., 2011). The end results of the AVIRIS preprocessing was 180 input features per date: 177 continuum removal reflectance bands and the MESMA-derived GV, NPV, and soil fractional cover.

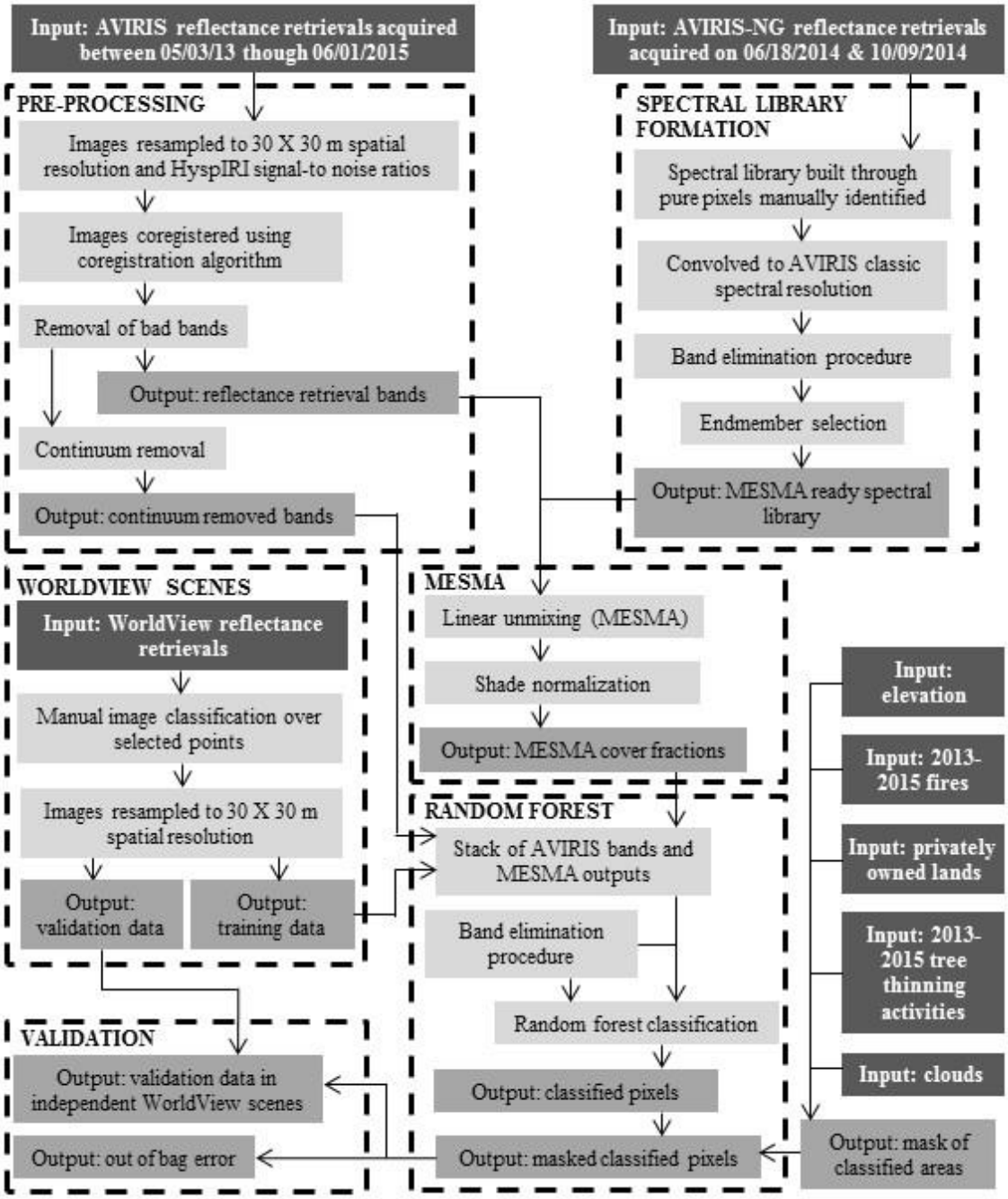

Figure 3.2. Diagram of the workflow of the AVIRIS image preprocessing, classification, and validation process.

3.2.3. Training and Validation Data Collection

Given the geographic scope of this study, collecting training and validation data *in situ* would have been prohibitively expensive and time-consuming. I employed the same strategy as several previous studies to overcome this problem: using high spatial resolution imagery

as a data source to train and validate classifications (Fabian E. Fassnacht et al., 2014; Meddens et al., 2013). Specifically, I used 1.5 m resolution multispectral images from WorldView-2 and 3 acquired between March and July 2015. Five WorldView scenes were used for training data collection, and other five scenes were used to collect validation data (Figure 3.1).

Even when using imagery for training and validation, sampling schemes must be carefully constructed. Among critical factors determining the preferred sampling design for supervised classification are the classification objectives and relative abundance of each target class in the image. For example, classifiers trained with simple random samples put less emphasis on the classification accuracy of the rarest classes, because the inclusion probability for a pixel of any given class is determined by how common the class is within an image. Common solutions to this problem include: class proportional allocation in the samples through stratified sampling, under-sampling common classes, and more complex designs (Stehman, 2009).

In this study, I used three classes: green conifer; red stage conifer, which included only red stage mortality occurring after summer 2014; and non-conifer. Gray stage conifers and any red stage mortality occurring before the fall of 2014 were considered outside the scope of this study and training data were not collected for these classes. The red stage conifer mortality class — a critical focus of this study —was relatively rare in the study area in 2015, which made the use of a probabilistic sampling design for all classes impractical. Therefore, samples for red stage conifers were selected by visually inspecting the WorldView images, whereas green conifer and non-conifer samples were identified from randomly generated points.

The red stage mortality pixels identified in the WorldView images were aggregated from 1.5 x 1.5 m to a 30 x 30 m area and used to estimate the percent area within the 30-m pixels (Meddens et al., 2013). Only 30 m pixels with more than 50% mortality were used as training and validation data for the red stage conifer class. For these pixels, the 2014 and 2015 AVIRIS spectra were reviewed manually to verify whether the spectra were consistent with conifer mortality occurring after summer 2014. Pixels with strong NPV signals in the summer of 2014, which indicated that the tree crowns were no longer representing largely healthy conifers at that time, were not used as training or validation data. A few pixels with spectra consistent with weak NPV signals in 2015 were not included as training data in order to collect a truly representative sample of red stage conifers. Some reasons that a pixel may not have a strong NPV signal despite WorldView imagery indicating it is more than 50% mortaltiy include minor co-registration errors between the AVIRIS and WorldView imagery or canopy change (trees transitioning to gray stage or falling down and thus exposing the understory) between the time the two images were acquired. No review of 2015 spectra was conducted for the validation data.

As mentioned earlier, for the collection of green conifer and non-conifer cover classes, 30 by 30 m AVIRIS pixels within the study area were randomly sampled across the WorldView images. In the training images, these pixels were labeled as conifer or non-conifer based on the class with the higher proportion of WorldView pixels within the AVIRIS pixel. 30 m pixels labeled as conifer with any amount of red stage conifer mortality in the overstory were not used as training or validation. For the green conifer and non-conifer classes, accurate classification of extremely mixed pixels was considered unnecessary for the validation experiments, given the study objectives. Therefore, for the

validation images only, 30 m pixels that had less than 80% cover of either class were not used. A summary of the training and validation pixels per WorldView scene is given in Table 3.1.

Table 3.1. Summary of 30 m training and validation pixel collection numbers by WorldView scene. Individual 14 July WorldView scenes used for validation data were combined in this table since each individual scene contributed a small amount of area.

	Number of Healthy Conifer Pixels	Number of Red Stage Conifer Pixels	Number of Non-Conifer Cover Pixels
Training			
25 March, 2015, Scene #054347101010_01_P0031	218	50	235
5 April, 2015, Scene #500431053100_01_P0021	204	388	429
6 May, 2015, Scene #500431054060_01_P0041	299	62	275
22 June, 2015, Scene #500431050050_01_P0011	152	19	1205
14 July, 2015, Scene #500503954040_01_P0071	512	595	1042
14 July, 2015, Scene #500503954040_01_P0031	197	111	1091
Training Data Total	1582	1225	4277
Validation			
6 May, 2015, Scene #500431054050_01_P0051	181	65	388
25 June, 2015, Scene #500431050040_01_P0011	356	225	225
14 July, 2015, Combined: Scene #500503954040_01_P0061 Scene #500503954040_01_P0051 Scene #500503954040_01_P0041	78	147	286
Validation Data Total	615	437	899

3.2.4. Training and Validation Data Collection

Validation data for the red stage mortality class was collected independently of the actual abundance of this class. Since the actual relative abundances of the classes were not known, sampled individual validation pixels in each class were given weights to even the influence of the classes for the purposes of calculating producer's accuracies (PA), user's accuracies (UA), overall accuracy (OA), and weighted kappa (Cohen, 1968; He and Garcia, 2009). Although this puts more importance on red stage mortality class than would be expected based on its abundance, this was felt to be appropriate given this study's focus. Weights were computed using the following formula:

$$ {}_{w}n_{ij} = \left(\frac{N}{n_{+i}}\right) * n_{ij} \qquad (3.1) $$

where N is the total number of test samples; n_{ij} is the number of samples in reference class *i* that were mapped as class *j*; n_{+i} represents the number of samples within class *i*, and ${}_{w}n_{ij}$ denotes the weighted version of n_{ij}.

I used three primary statistics to evaluate the accuracy: out-of-bag (OOB) error (Breiman, 2001), a weighted overall accuracy over an independent validation set, and the weighted kappa coefficient (Cohen, 1968; Congalton and Green, 1999) calculated for the independent validation set. Kappa variance and significance were estimated using the kappa variance equation (Congalton and Green, 1999). Since the training and validation datasets were collected in different manners (due to the different thresholds of cover needed for a pixel to be used in the green conifer or non-conifer class), the relative accuracies of the two sets should not be viewed as directly comparable.

3.2.5. Random Forest Classification

In this study, I used the RF classification technique (Breiman, 2001). The RF algorithm was implemented in the R environment (R Core Development Team 2016 Version 3.2.2)

using the "*randomForest*" package version 3.6 (Liaw and Wiener, 2002). RF is an ensemble classification technique, where reliable classifications are derived from a large number of classification trees (CT; Breiman, 2001). The training data in each CT is a subset of the training data created through selection with replacement from the entire training dataset (Breiman, 2001). In this fashion, some data points (in this study, individual training pixels) are selected multiple times and others not at all (Breiman, 2001). If a training sample is selected to be used to train an individual CT, it is considered to be an in-bag sample for that iteration; otherwise, it is an OOB sample (Breiman, 2001). RF also includes a user-defined subset of the total features at each individual split (a parameter often called *Mtry*). In the RF classification, individual CTs are not pruned and therefore have high variance; however, averaging the output over a user-defined number of CT trees (a parameter often called *Ntree*) makes the overall RF classifier stable (Breiman, 2001). Because the OOB sample is independent of the in-bag sample, one unique benefit of RF is that the average CT's error rate on the OOB samples provides an independent assessment of accuracy (Breiman, 2001). Another beneficial property of RF is since only a subset of the total features are included in each split, a measure of feature importance can be developed based on the effect each individual feature has on accuracy (Breiman, 2001).

The standard implementation of RF was slightly modified in this study. In a preliminary investigation of spatial autocorrelation, a maximum range value of 300 m was found for various bands, indicating that if two or more pixels are within this distance, they are likely to be biased towards being similar to each other and therefore may create less accurate RF classifications (Millard and Richardson, 2015). To correct for this, the data used to train each individual CT for each class were chosen by first selecting a random pixel, then all

other pixels of the same class within a 300 meter radius were eliminated (flagged unavailable for selection). This process was done iteratively for each class until all points in the class were either selected or eliminated. This is conceptually similar to using RF in an object-oriented context (Latifi et al., 2014), but the objects were defined by the range distance and a single spectral sample was taken for each object. In order to effectively weight the rare but important red stage conifer class, training pixels from both the healthy conifer and non-conifer class were randomly eliminated until the number was equal between all classes. This entire process was repeated for each individual CT used by the ensemble RF classifier, with the entire training data being made available at the start of each iteration.

One side effect of this modification is a relatively small number of pixels selected to be OOB compared to the entire training set for each individual iteration. In order to make the OOB error for the entire training set stable, a relatively high value for *Ntree* was needed. Since the RF classifier has been shown to not overfit with increasing *Ntree* values (Guan et al., 2013), a high *Ntree* value should not have an effect on the overall accuracy of the RF classifier. An Ntree value of 4,000 was used because OOB error on the training data stabilized at that value. For the other user-defined parameter in RF, *Mtry*, the exact *Mtry* value varied for each classification, but it was always equal to the square root of the corresponding number of input features, a value that a variety of remote sensing studies have shown to be a robust choice (Belgiu and Dragut, 2016).

3.2.6. Feature Set Tests

3.2.6.1. Feature Set Tests – Multispectral Simulation and Processing

In order to test the accuracy of a similar multispectral sampling effort, each of the AVIRIS dates was spectrally convolved to the spectral resolution of Landsat-8 Operational

Land Imager (OLI), bands 1-7 and 9. Since continuum removal is not possible on multispectral data, in order to minimize radiometric differences between flight lines and dates I applied the Multivariate Alteration Detection (MAD) algorithm developed by Canty et al. (2004).

Several vegetation indices were calculated based on the radiometrically normalized flight lines (Table 3.2). For the Landsat simulated data, instead of performing MESMA to obtain cover fractions, the first three Tasseled Cap transformations based on Landsat-8 imagery (Baig et al., 2014) were performed. Thus, for each multispectral date I computed the following 15 features: the radiometrically normalized eight bands and the seven vegetation indices. The workflow for processing the simulated multispectral data was selected to be as comparable as possible to Meddens et al. (2013), a study that also used multispectral data to identify red stage conifer mortality in a single and multi-date context. Feature sets processed in this way will be referred to as Multispectral feature sets for the remainder of this chapter.

Table 3.2. Broadband vegetation indices calculated as part of the multispectral preprocessing. Bands (B) refers to the Landsat 8 band order.

Index	Formula	Reference
Red-green index	B4/B3	Coops et al. (2006)
Normalized difference vegetation index	(B5-B4)/(B5+B4)	Tucker (1979)
Simple index	B6/B5	Vogelmann (1990)
Normalized difference moisture index	(B5-B6)/(B5+B6)	Wilson and Sader (2002)
Tasseled cap brightness	0.3029*B2 + 0.2786*B3 + 0.4733*B4 + 0.5599*B5 + 0.508*B6 + 0.1872*B7	Crist (1985) Baig et al. (2014)
Tasseled cap greenness	-0.2941*B2 - 0.243*B3 - 0.5424*B4 + 0.7276*B5 + 0.0713*B6 – 0.1608*B7	
Tasseled cap wetness	0.1511*B2 + 0.1973*B3 + 0.3283*B4 + 0.3407*B5 - 0.7117*B6 – 0.4559*B7	

Since the use of multiple flight lines of airborne data to simulate spaceborne data is a unique objective among red stage mortality identification studies, I also replicated the single-date workflow of Meddens *et al.* (2013) as closely as possible on my data, which provided us with an additional point of comparison. For this workflow, I used the MLC on Summer 2015 imagery (Franklin et al., 2003). Although I used the same training dataset for all experiments in the study, to better conform to the classifier used in Meddens et al. (2013), the classes with more training data were subsampled to equalize the number of samples per class (n=1225). Validation data accuracy was assessed in the same manner as in the rest of this study. This image classification this workflow will be referred to as Landsat MLC.

There are unavoidable differences between my training data and the data used by Meddens et al. (2013). The most notable difference is that in Meddens et al. only pixels with >70% cover of the dominant class were used for training, while in my study the corresponding threshold was 50%. Since mortality in my study area was not nearly as prevalent as in Meddens et al., requiring >70% red stage mortality cover would have eliminated too much training data. Meddens et al. (2013) also used four classes; and while

three of these classes were similar to ours, the fourth class used by Meddens et al., shadow and clouds, was masked before image classification in my study.

3.2.6.2. Feature Set Tests – Temporal

To evaluate the effect of the inclusion or exclusion of various time periods, six separate feature sets were tested. Three of the feature sets used represented each of the three single-date images acquired late in the drought, when the red stage mortality would be visible. Feature sets composed of single dates will be referred to as Summer 2015, Spring 2015, and Fall 2014 in this chapter (note that capitalization is used to denote the feature set names). One potential challenge for a classification based on single-date imagery is that many non-conifer areas also died back in response to the drought, and therefore both non-conifer and red stage mortality pixels could have spectral signals broadly consistent with NPV during the red stage period. Theoretically, one means of separating these classes is by comparing the spectra before and after the red stage period. In order to test the usefulness of this type of change detection, a feature set that is comprised of summer 2013, summer 2014, and summer 2015 images combined was created; this feature set will be referred to as All-Summer. Another possible means of separation is through the comparison of spectral signals between different seasons. One reason interseasonal time series may be useful is that many non-conifer vegetation types are deciduous or senesce, however healthy conifer and red stage mortality should be seasonally invariant. To test the usefulness of seasonal data only, a feature set comprised of only the combined fall 2014, spring 2015, and summer 2015 imagery was created and will be referred to as Late-Drought. To test possible synergies between the various temporal data, merging all six of the AVIRIS dates into a single large

feature set was also tested; this will be referred to as All-Dates for the remainder of the analysis.

3.2.6.3. Feature Set Tests – Feature Reduction

Although the RF classifier can perform well in high-dimensional feature spaces, feature reduction of imaging spectroscopy data has previously been shown to improve classification accuracy (Belgiu and Dragut, 2016; Ham et al., 2005). In this study, I chose to use an embedded feature selection method, wherein features are backward-eliminated based on their RF-generated feature importance value until the OOB error stabilizes (Díaz-Uriarte and Alvarez de Andrés, 2006). I implemented feature reduction using the '*varSelRF*' R package and applied it to the entire training dataset. Classifications based on feature sets processed in this manner will be referred to as Feature-Reduced for the remainder of this chapter. Multispectral single-date feature sets had only 15 features initially, so feature reduction was not deemed necessary. All other feature sets received feature reduction.

3.2.7. Ancillary Data Sources

To provide greater context and further independent validation to my results, I drew upon two ancillary data sources relevant to tree mortality in the study area. The first data source was ADS conducted by the United States Forest Service in 2015 (USFS, 2016). The ADS data used are digitized, manually delineated polygons produced by trained surveyors onboard an airplane typically flown 300-600m above the tree line. The surveyors also visually assess and record their best estimate for the number of dead trees within the polygon. My entire study area was examined via ADS in 2015. Preprocessing of the ADS data for use in this study is fully documented in Appendix 3. Because the ADS was not specifically designed as a tree mortality mapping technology, it is inherently subjective and

approximate method, both in the estimates of dead trees per unit area and the polygon location. Since at the scale of my classification (30 X 30 m pixels) ASD data lack accuracy, I did not use it for direct pixel to polygon comparison, but rather as a source for broad spatial scale comparison.

I also used the 2015 canopy water content (CWC) and progressive water stress (PWS) between 2011 and 2015 for the study area derived from Asner et al. (2016) as a point of comparison. I will briefly summarize here the methods for obtaining CWC and PWS that are documented in full in Asner et al., 2016. Airborne high resolution imaging spectroscopy was flown over a select representative area of California in 2015. To estimate the CWC, the collected imaging spectroscopy was run through atmospheric correction software to decouple the absorption of light at certain wavelengths due to atmospheric water vapor and liquid surface water. The derived CWC and several spatially explicit input features available across California were then used to train a multi-layer neural network to estimate CWC between 2011 and 2015. CWC and PWS are not direct indicators of crown mortality, but are highly indicative of stress and vulnerability in an area (Asner et al., 2016). The spatial scale of the CWC and PWS data is 30 X 30 m pixels, making direct pixel-to-pixel comparisons with my classification straightforward after co-alignment.

3.3. Results

3.3.1. Spectra Separability

In order to investigate whether a classification might be successful, the spectral differences between the classes through time were examined (Figure 3.3). Visually, it appears that pixels used to train the red stage class (pixels that transitioned to red stage after summer 2014) generally became brighter and also had increased reflectance in the red to red

edge portion of the spectrum compared to green conifers. This change appears to increase through time with a definite change between summer 2014 and fall 2014. The non-conifer class also appears to have somewhat similar spectral changes, likely associated with drought-driven dieback of chaparral, hardwoods, and other woody vegetation. It is also apparent that the reflectance retrievals from spring and summer of 2015 have more artifacts associated with the atmospheric correction processing, compared to the other dates.

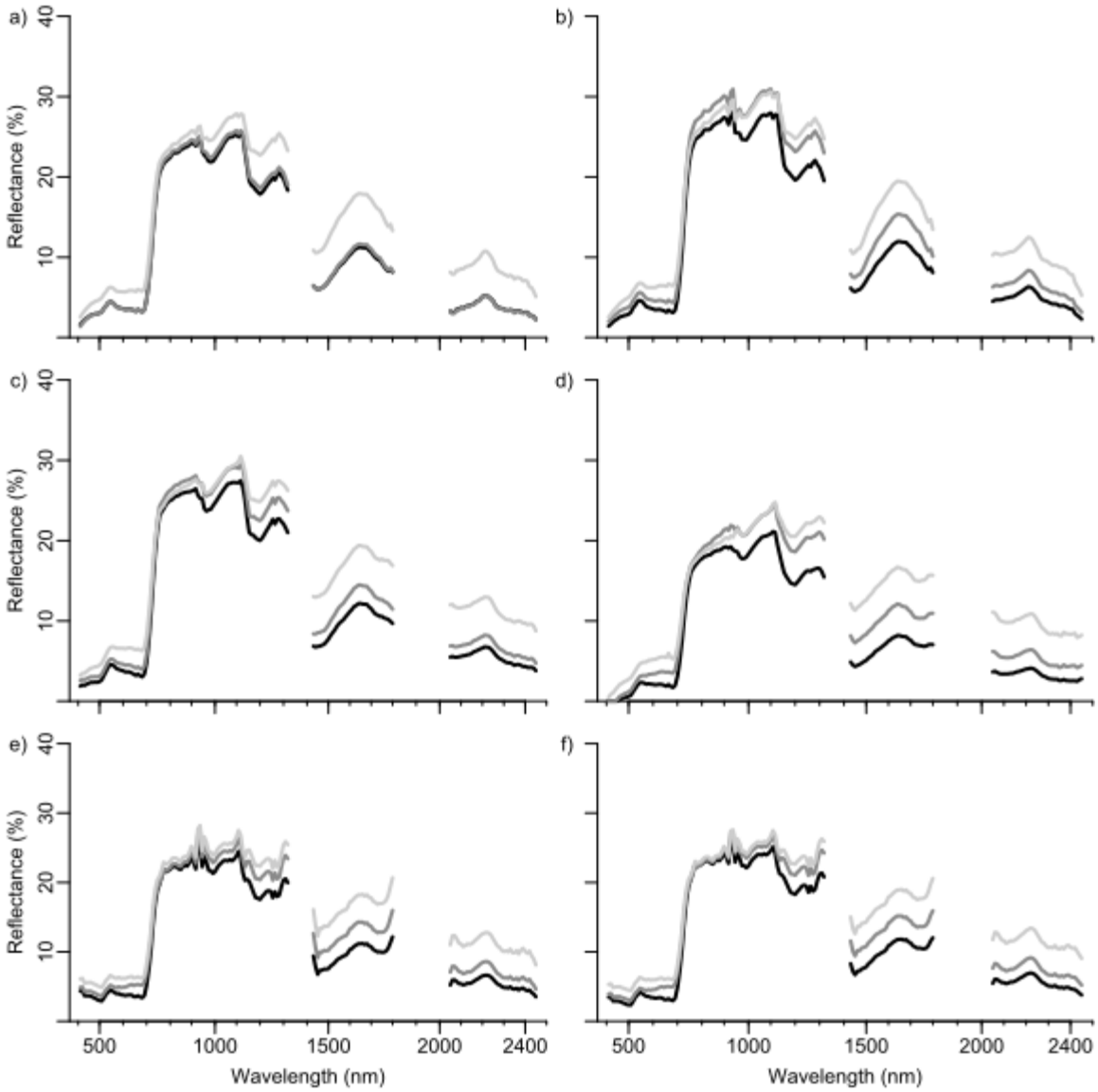

Figure 3.3. The mean AVIRIS spectral profile of all pixels used as training data for the green conifer class (black), 2015 red stage conifer (dark gray), and non-conifer (light gray) classes through time, with each letter corresponding to the following time-step: a) spring 2013, b) summer 2013, c) summer 2014, d) fall 2014, e) spring 2015, f) summer 2015.

3.3.2. Classification Comparison

Of all the classification results, AVIRIS Late-Drought Feature-Reduced had the single highest kappa statistic, although two other feature sets were not significantly lower (Table 3.3). After feature reduction, AVIRIS Late-Drought and AVIRIS All-Dates, both of which include images from fall 2014 to summer 2015, performed significantly better than any

single-date feature set. In contrast, AVIRIS All-Summer, which only included the three summer dates, performed no better than the single-date AVIRIS Summer 2015 feature set. Of the three single-date feature sets, AVIRIS Fall 2014 had the significantly highest kappa value.

Table 3.3. The out of bag (OOB) error rate, weighted overall accuracy, and weighted kappa for each of the feature sets. Superscripts indicate significance at $p < 0.05$. If a kappa does not share a superscript with another kappa value it indicates the two kappa values are significantly different from each other. Letters are ordered from highest kappa value to lowest.

	OOB Error	Weighted Overall Accuracy	Weighted Kappa	Kappa Variance
All-Dates	78.9%	83.1%	0.747^{c}	5.20E-05
All-Dates Feature-Reduced	80.0%	84.8%	0.772^{a}	4.84E-05
Late-Drought	79.3%	84.5%	0.768^{ab}	4.92E-05
Late-Drought Feature-Reduced	80.5%	85.1%	0.776^{a}	4.78E-05
All-Summer	75.8%	79.0%	0.685^{gh}	6.08E-05
All-Summer Feature-Reduced	76.7%	79.3%	0.690^{fg}	6.04E-05
Fall 2014	76.1%	83.1%	0.747^{c}	5.26E-05
Fall 2014 Feature-Reduced	75.7%	83.4%	0.750^{bc}	5.20E-05
Spring 2015	77.4%	80.8%	0.711^{def}	5.85E-05
Spring 2015 Feature-Reduced	78.5%	81.1%	0.716^{de}	5.77E-05
Summer 2015	76.4%	81.7%	0.725^{d}	5.60E-05
Summer 2015 Feature-Reduced	76.7%	79.3%	0.690^{fg}	6.04E-05
Landsat All-Dates	72.1%	80.0%	0.699^{efgh}	5.94E-05
Landsat All-Dates Feature-Reduced	72.1%	80.2%	0.703^{efgh}	5.90E-05
Landsat Late-Drought	65.3%	63.4%	0.451^{n}	7.71E-05
Landsat Late-Drought Feature-Reduced	71.1%	77.2%	0.658^{ij}	6.48E-05
Landsat All-Summer	70.1%	77.3%	0.660^{ij}	6.51E-05
Landsat All-Summer Feature-Reduced	70.3%	77.8%	0.667^{hi}	6.44E-05
Landsat Fall 2014	67.2%	76.0%	0.640^{jk}	6.78E-05
Landsat Spring 2015	68.9%	73.7%	0.605^{l}	7.25E-05
Landsat Summer 2015	69.6%	75.7%	0.635^{k}	6.90E-05
Landsat MLC	-	65.4%	0.475^{m}	8.04E-05

Feature reduction generally had a positive effect on the accuracy metrics of the AVIRIS imagery for the independent validation data, although the positive effect was not generally significant. The only classification that feature reduction was able to produce a statistically significant increase in validation kappa values was AVIRIS All-Dates dataset, which had the largest number of features. Feature reduction for the Landsat simulated multi-date feature sets also had a positive impact on the kappa value, however, except for Landsat All-Summer, the increase was not significant.

Landsat All-Dates had a significantly higher kappa value than any other Landsat-simulated feature set. Mirroring the AVIRIS data, Landsat Fall 2014 had the highest value of any other single-date feature set, however, the higher value was not significant. After feature reduction, all multi-date Landsat feature sets had higher kappa values than the Landsat single-date, although not always significantly higher. Whereas with AVIRIS Late-Drought Feature-Reduced performed significantly better than All-Summer Featured-Reduced, there was no significant difference between Landsat Late-Drought Feature-Reduced and Landsat All-Summer Feature-Reduced. Landsat MLC performed significantly worse than most other Landsat based classifications, including the most immediately analogous Landsat Summer 2015.

Classification results based on imaging spectroscopy images always had significantly higher kappa values than their multispectral counterparts (the highest performing imaging spectroscopy classification had an OA 85.1%, whereas the highest performing multispectral classification had an overall accuracy of 80.2%). In order to assess the source of differences in accuracy between classifications based on imaging spectroscopy and multispectral features, the individual class UA (errors of commission) and PA (errors of omission) of the different feature sets were compared (Figure 3.4). Clearly, the biggest source of error in all classifications is the PA of the red stage class. Feature sets with AVIRIS spectral resolution had consistently better results than the multispectral resolution feature sets for the UA of this class. The significant increase in classification accuracy of AVIRIS Fall 2014 Feature-Reduced over other single-date AVIRIS feature sets appears to be primarily a result of the superior separation of the non-conifer class from the other two classes. The AVIRIS All-Dates Feature-Reduced based classification had the highest UA and PA for all classes.

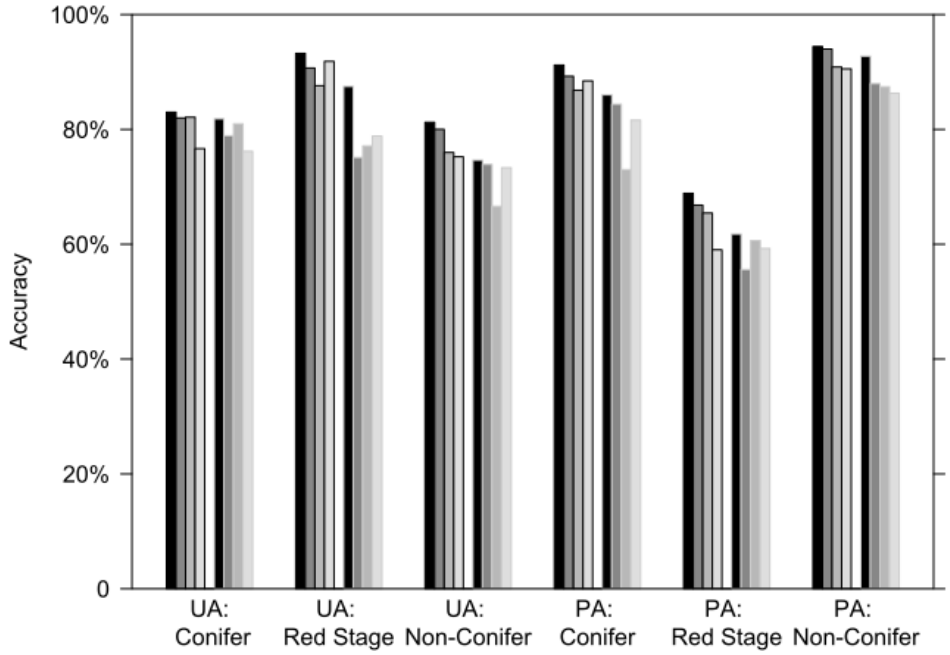

Figure 3.4. User Accuracy (UA) and Producers Accuracy (PA) for the different classification feature sets. Black fill indicates All-Dates, dark gray fill indicates Fall 2014, gray fill indicates Spring 2015, light gray fill indicates Summer 2015. Bar graphs on the left of each group with dark borders are feature reduced imaging spectroscopy based feature sets, on the right with light gray border are multispectral.

3.3.3. Spectral Region Selection

In general, the feature selection process reduced the number of input features substantially for the AVIRIS data, ranging from a reduction of 58.9% of the original bands (Fall 2014 and Summer 2015) to 89.3% (All-Dates). Both multi-temporal AVIRIS based feature sets that used fall 2014 imagery, All-Dates and Late-Drought, selected more than half of their bands from fall 2014 alone (Table 3.4). All-Summer selected a majority of its bands from summer 2015, and both the All-Dates and All-Summer feature sets selected proportionally fewer bands from images acquired before the pixels had transitioned to red stage mortality (summer 2014 and earlier). Considering the relatively narrow part of the spectrum the red edge occupies (700 – 755 nm, representing only 6 bands in AVIRIS), bands were disproportionally likely to be selected from it, with bands in the visible (410 -

700 nm) and the SWIR2 (2040 – 2430 nm) also consistently being important disproportion to the spectral range they occupy. In contrast, the numerous bands in the near infrared (755 – 1315 nm) and SWIR1 (1430 – 1800 nm) were proportionally less likely to be selected for use. However, bands from all parts of the spectrum were selected for all feature set arrangements. MESMA cover fractions were not selected for use by the All-Dates, All-Summer, and Fall 2014 feature sets, however, the Summer 2015 and Spring 2015 feature sets both used the GV and Soil cover fractions.

Table 3.4. The number of bands selected in various spectral regions by the embedded Random Forest feature reduction process for various feature sets. Note that the part of spectrum designated as visible was between 410 nm – 700 nm and included 32 unique AVIRIS bands, the part of the spectrum designated as red edge was between 700 nm – 755 nm and included 6 unique AVIRIS bands, the part of the spectrum designated as near infrared was between 755 nm – 1315 nm and included 60 unique bands, the part of the spectrum designated as SWIR1 was between 1430 nm – 1800 nm and included 38 unique bands, and the part of the spectrum designated as SWIR 2 was between 2040 nm – 2430 nm and included 41 unique bands. The green vegetation (GV), non-photosynthetic vegetation (NPV), and soil cover fractions are single bands.

Feature Set	Season	Visible	Red Edge	Near Infrared	SWIR 1	SWIR 2	GV	NPV	Soil	Total
All-Dates	Spring 2013		1	4						5
	Summer 2013									0
	Summer 2014		2	6	3					11
	Fall 2014	18	3	9	10	25				65
	Spring 2015	10	2	2		1				15
	Summer 2015	9	3	1		7				20
All-Summer	Summer 2013			1						1
	Summer 2014		3	12	4					19
	Summer 2015	12	3	11	3	9				38
Late-Drought	Fall 2014	22	4	14	16	29				85
	Spring 2015	11	2	7		2	1			23
	Summer 2015	10	3	6	1	14				34
Single Dates	Fall 2014	20	4	15	8	27				74
	Spring 2015	11	3	12	9	10	1		1	47
	Summer 2015	12	4	18	23	15	1		1	74

Comparing the bands selected by the AVIRIS Late-Drought feature reduction with the spectral range of Landsat-8, 79 out of the 140 were outside of Landsat-8's spectral range (Figure 3.5). The red edge (700 - 755 nm) and a region in the near infrared (1100 - 1200 nm) parts of spectrum consistently had bands selected in them but are not sampled by Landsat-8.

In fall 2014, several other regions, including 2300-2400 nm, also appear to be important for classification, but outside of Landsat-8's spectral range.

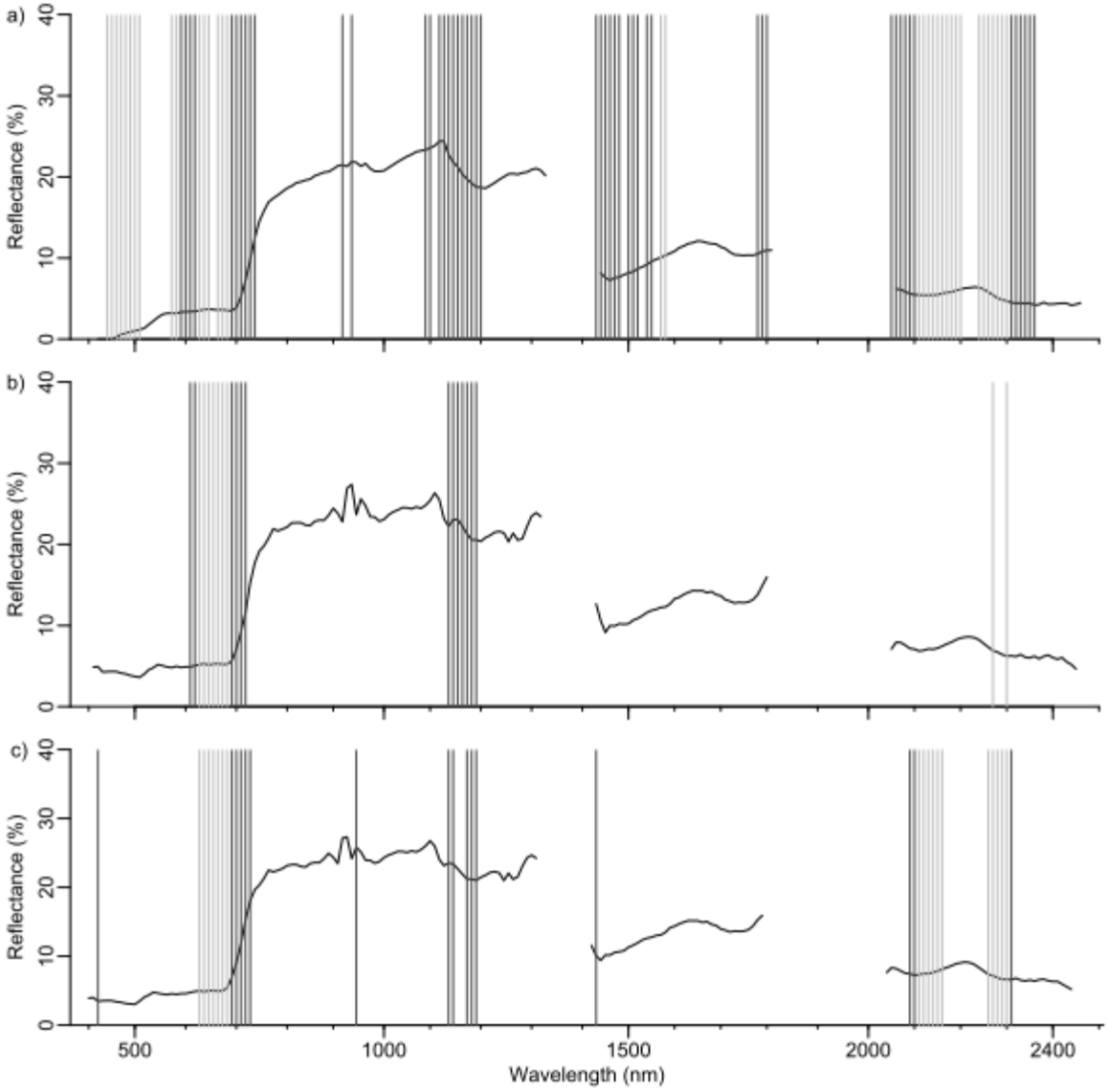

Figure 3.5. Average spectrum of red stage mortality pixels from training data in a) fall 2014, b) spring 2015, and c) summer 2015. Vertical bars represent bands selected to be used in AVIRIS Late-Drought Feature-Reduced. Light gray vertical bars are AVIRIS bands located within parts of the spectrum sampled by Landsat-8, dark gray bars are bands at wavelengths not sampled by Landsat-8.

3.3.4. Comparison to Ancillary Data

Some clear patterns emerge when comparing the AVIRIS-based classification (Figure 3.6a), the ADS mortality observations (Figure 3.6b), 2015 CWC (Figure 3.6c), and PWS from 2011-2015 (Figure 3.6d) across the study area. At the scale of the entire study area, the mapped conifer areas in the AVIRIS All-Dates Feature-Reduced based classification (Figure

3.6a) appear to broadly match the ADS survey areas identified as conifer (Figure 3.6b) and the areas of high CWC (Figure 3.6c). Although there are areas of agreement between areas mapped as dead conifer in Figure 3.6a and areas identified as having a large number of dead conifers in the ADS and areas of high PWS (Figure 3.6d), there are also areas that do not appear to be in agreement. I further investigate these differences by focusing on two areas with relatively high ADS dead trees per acre values and moderate to high PWS values (Figure 3.7). In general, my classification appears to capture the detail of tree mortality better than the other two data sources, but it also appears to model some areas as containing red stage mortality that do not according to the other data sets.

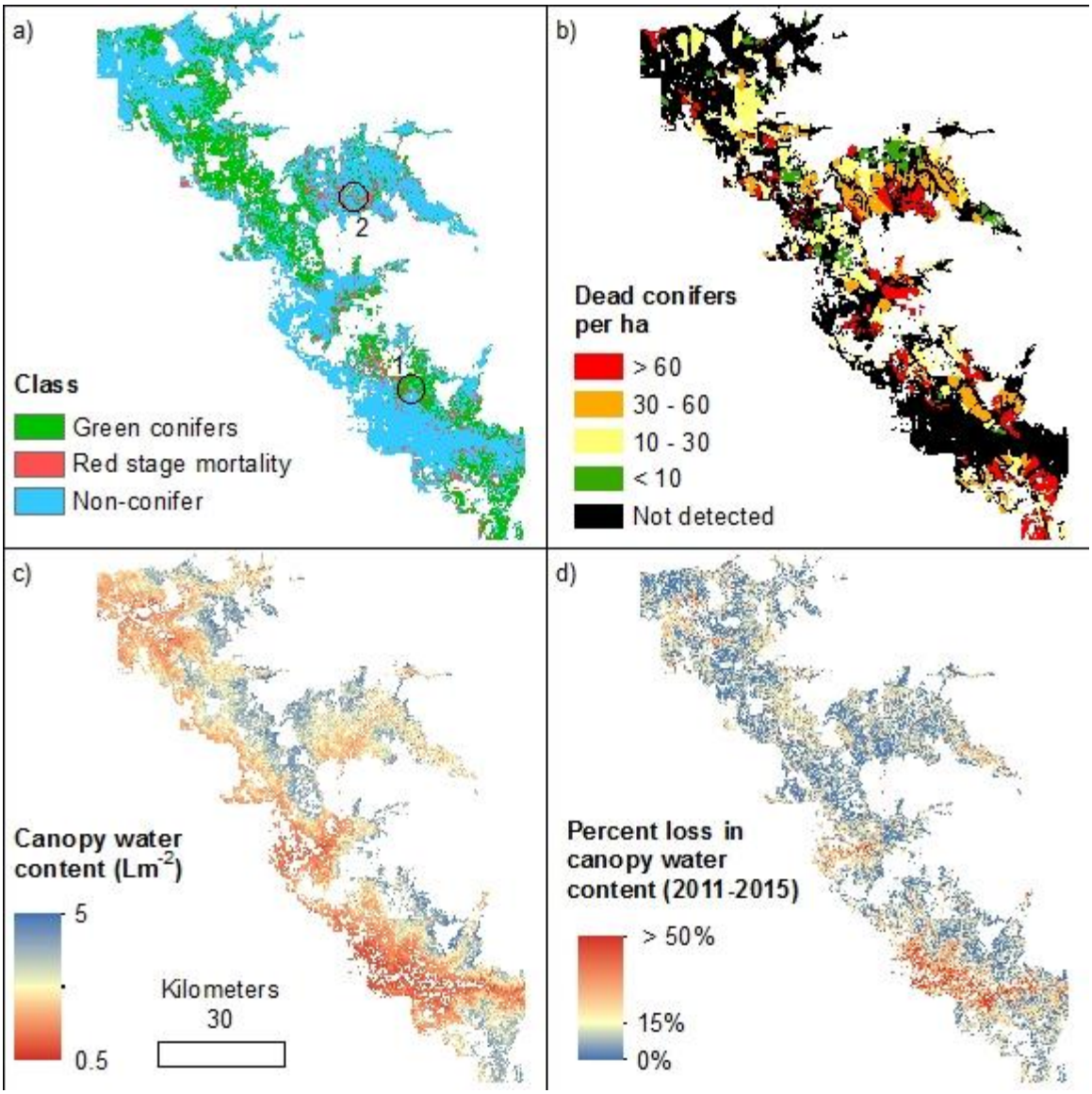

Figure 3.6. a) AVIRIS All-Dates Feature-Reduced based classification of the study area. The numbered circles represent two focus areas presented in detail Figure 3.7 b) Aerial detection survey mortality estimates for conifers per ha (USFS, 2016). c) Canopy Water Content (L m^{-2}) from Asner et al. (2016) color gradient. d) Gradient of percent of loss in canopy water content between 2011 and 2015 from Asner et al. (2016).

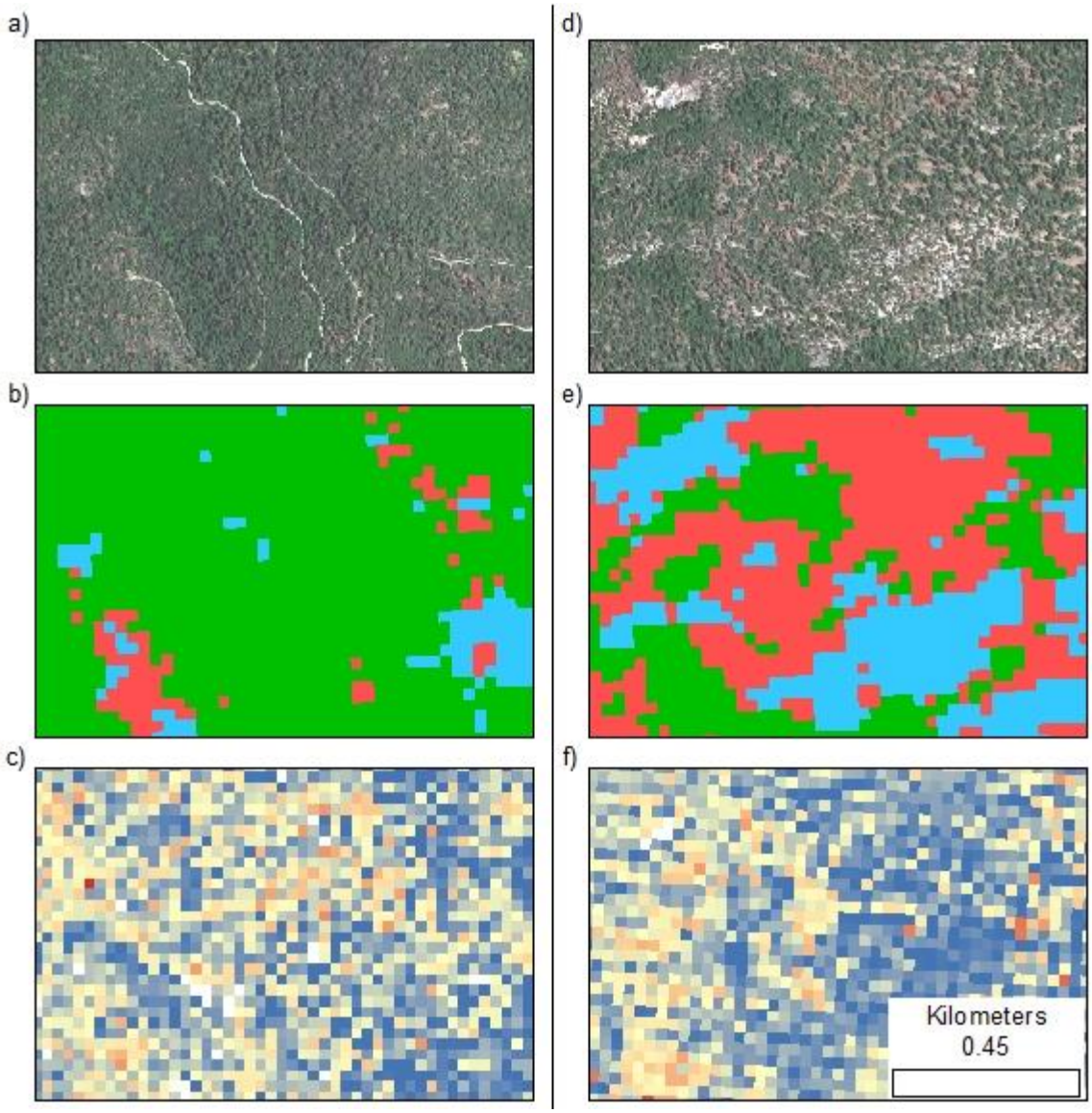

Figure 3.7. Two focus areas within the study area. Panels a), b), and c) corresponds with focal area 1 in Figure 3.6a, panels d), e), and f) corresponds with focal area 2 in Figure 3.6a. Panels a) and d) represent true color WorldView imagery acquired on 14 July 2015. Panels b) and e) represent the AVIRIS All-Dates Feature-Reduced based classification (green indicating health conifer, red indicating red stage mortality, blue indicating non-conifer). Panels c) and f) represent percent canopy water content loss from Asner et al. (2016), with blue indicated less canopy water loss and orange meaning more (see Figure 3.6d). The entirety of the area represented in panels a), b), and c) were estimated to have approximately 37 dead conifers per ha by aerial detection surveys and the entirety of panels d), e), and f) were estimated to have 98 dead conifers per ha.

In order to further investigate fine scale relationships between the classification and the ancillary data sets, 1000 healthy conifer pixels and 1000 red stage mortality pixels were randomly sampled and the differences in CWC and PWS were then examined (Table 3.5).

Red stage mortality pixels had, on average, significantly less CWC and a greater PWS loss. This analysis was not done for ADS data because it would have assumed a degree of accuracy for ADS data beyond what the data was intended for and no assessment of ADS uncertainty was conducted as part of this study.

Table 3.5. Comparison of the mean and standard error (in parenthesis) of 1000 randomly selected healthy conifer and red stage pixels as classified by AVIRIS All-Dates Feature Reduced and canopy water content (CWC) and progressive water stress (PWS) from 2011 to 2015 from Asner et al. (2016). For both metrics the difference in means is significant (at p=0.05) using a 1-sided t-test.

	Healthy Conifer Pixel	Red Stage Pixel
CWC (L m^{-2})	2.831 (0.022)	2.383 (0.021)
PWS (%)	9.6% (0.2%)	11.6% (0.3%)

3.4. Discussion

3.4.1. Performance of Various Feature Sets

3.4.1.1. Imaging Spectroscopy vs Multispectral Effect on Accuracy

Comparing feature sets constructed from the same temporal data, I observed that RF classifications based on imaging spectroscopy consistently outperformed multispectral imagery, almost always increasing overall accuracy by 5% or more. Imaging spectroscopy has been shown to be better able to identify plant functional types than multispectral imagery (Ustin et al., 2004), and it has been theorized that this ability may allow imaging spectroscopy to better identify mortality occurring in a mixture of cover types compared to multispectral imagery (White et al., 2007). The UA of the non-conifers in Figure 3.4 was one metric in which imaging spectroscopy based classifications that included the fall 2014 scene consistently outperformed multispectral classifications. Leaf moisture levels are lowest in the fall for Sierra Nevada's Mediterranean climate; lower leaf moisture levels and early senescence in broadleaf compared to needleleaf plants would cause narrow absorption features associated with the nitrogen, lignin, and other leaf chemical compounds in the SWIR2 to become more apparent in the fall (Burns and Ciurczak, 2007; Curran, 1989), and this may not be captured by a spectrally broad SWIR2 reflectance. This result provides additional evidence that the ability of imaging spectroscopy to identify plant functional type may be a major asset to tree mortality identification.

The area where imaging spectroscopy outperformed multispectral imagery the most is the PA and UA of the red stage mortality class (for All Dates Reduced Features, imaging spectroscopy's PA = 68.6%, UA=93.2%; for multiple spectral imagery PA = 61.8, UA = 87.5%). This may be due to enhanced sensitivity to narrow wavelengths association with lignin and cellulose absorption features, such as the 2300-2400 nm spectral region (Daughtry, 2001). By detecting lignin and cellulose absorption, imaging spectroscopy is better able to differentiate dead plant material from soils when compared to multispectral imagery. Figure 3.5 provides further evidence for the importance of the 2300–2400 nm spectral region, as evidenced by the amount of bands RF feature reduction selected from this region in fall 2014. Furthermore, by being sensitive to spectral regions such as the red edge and the 1100–1200 nm spectral region which is associated with liquid water imaging spectroscopy may also be able to detect subtle changes due to leaf desiccation that Landsat-8 cannot (Ahern, 1988; Asner et al., 2016). The prominence of bands selected in these spectral regions in Figure 3.5 highlights imaging spectroscopy being potentially more sensitive to liquid water change than Landsat-8 imagery. The relative importance of bands in the red edge parts of the spectrum for imaging spectroscopy's ability to detect red stage mortality identification has also been previously reported in the literature (Fabian E. Fassnacht et al., 2014).

3.4.1.2. Temporal Data Effect on Accuracy

Multi-temporal information could increase the classification accuracy over a single date by allowing either the identification of different inter-annual or inter-seasonal changes between classes. By having one analysis, which included only the three seasons where the red stage mortality would be visible (Late-Drought), and another analysis, which only

included the three flights taken in the summer of each year (All-Summer), I attempted to investigate which source of information was more important to the study. With or without band reduction, AVIRIS All-Summer failed to perform significantly better than single-date AVIRIS Summer 2015 and AVIRIS All-Dates failed to perform better than AVIRIS Late-Drought. This result strongly suggests that annual changes were not a major contributor to accuracy for the AVIRIS imagery based RF classification. On the other hand, the significantly high kappa values obtained from classifications that used the fall 2014, spring 2015, and summer 2015 image sets suggests that accounting for seasonal differences did improve the accuracy. For most classes, the UA and PA of AVIRIS All-Dates Feature-Reduced (Figure 3.4) were somewhat higher than the best single-date classifier. This suggests the superiority of the All-Dates feature set may be in its ability to incorporate important spectral features from each season and class.

RF, as applied in this study, may not be an optimal statistical learning method for interannual change detection with imaging spectroscopy. Different procedures that explicitly difference images or detect temporally anomalous spectral variation could provide higher accuracy in analyzing interannual differences in imagery. However, these approaches typically require many years of data best provided by a spaceborne sensor.

The multi-temporal Landsat imagery did not show similar patterns. After feature reduction, using images from the three summer dates and from the last three seasons yielded statistically insignificant differences in accuracy. This difference could stem from AVIRIS being able to register small seasonal spectral shifts that Landsat spectral resolution could not identify.

3.4.1.3. Feature Selection Effect on Accuracy

Although feature reduction did not produce significantly higher kappa values for most feature sets used, in this study the training dataset size was larger than in most similar studies and also comparable with the dimensionalities (i.e. the number of features) of the feature sets. The AVIRIS All-Dates feature set had by far the greatest dimensionality (two to six times greater than with the other imaging spectroscopy feature sets), and feature reduction both eliminated the largest number of features and caused the greatest and only statistically significant gain in overall accuracy for that feature set. It is also important to note that with the exception of one feature set, feature reduction never decreased the accuracy metrics of independent validation data. Feature reduction also greatly decreased processing times for training the RF algorithm and applying the classification to entire flight lines.

It is worth noting that only one feature reduction method was tested in this study; however, there are a wide variety of other feature reduction methods (Saeys et al., 2007) that could potentially lead to comparable or better accuracy of the final result. For example, Fassnacht et al. (2014) found that in a similar problem of conifer mortality classification, a genetic algorithm method for feature reduction more consistently and statistically significantly improved accuracy compared to the feature reduction method used in my study. Additional case studies comparing the value of different feature reduction techniques for tree mortality mapping would be an interesting subject of future research.

3.4.2. Overall Discussion of the Classifier Performance

The nature and challenges of the dataset used in this study, in particular using 66 AVIRIS flights to cover a large spatial area through time, is unique to the HyspIRI Prepatory Campaign. Exactly analogous studies do not exist. However, even the highest

accuracies reported in my study are still only comparable or slightly lower to the accuracies obtained in other studies of similar problems using multispectral imagery (Franklin et al., 2003; Liang et al., 2014; Meddens et al., 2013; Senf et al., 2015). In order to provide my methods and the resultant accuracies context, I replicated the methods of Meddens et al. (2013) single-date classification as closely as possible in the Landsat MLC classification workflow. The 65.4% overall accuracy I obtained is considerably lower than the 91.0% accuracy obtained in the original Meddens et al. study. Since the overall accuracy of the RF based Landsat Summer 2015 classification (75.7%) was significantly higher than Landsat MLC, and because other studies have also demonstrated RF achieving superior accuracy over MLC for red stage mortality identification (Senf et al., 2015), it seems unlikely that the classification methods chosen in this study led to lower accuracies.

Possible explanations for the higher classification error compared to previous studies include: the high species diversity and complex structure of crown level plant assemblages found in the study area; the relative rarity and spatial heterogeneity of red stage mortality in the Sierra Nevada in 2015; and methodological choices, such as the number of classes used. However, the dominant factor was, in my opinion, the manner of source image acquisition and preprocessing. Whereas my study used 11 separate AVIRIS based flight lines convolved to Landsat resolutions and radiometrically normalized for each time step, the classifications in Meddens et al. (2013) and similar studies are typically based on a single Landsat image per time step. Despite the greater signal-to-noise ratio of the simulated HyspIRI data relative to Landsat-8 (Lee et al., 2015; Roy et al., 2014) and the extensive efforts to radiometrically calibrate flight lines (Thompson et al., 2015), the cross-track illumination differences between flight lines represented a classification challenge that is absent in case of a single-

scene input. Furthermore, the FOV of AVIRIS (34 degrees) is significantly greater than that of Landsat (15 degrees), further exacerbating illumination artifacts. Since a wide swath width spaceborne imaging spectrometer was not available for this study, using an airborne dataset was the only option. One advantage imaging spectroscopy likely holds in this study is the superiority of continuum removal for reducing BRDF differences within and between flight lines over multispectral techniques, such as scene-to-scene radiometric normalization and computing vegetation indices. However, continuum removal does not completely eliminate this problem, and therefore, improved reduction of BRDF differences remains an important issue, even for a spaceborne hyperspectral sensor, if it is to be used over large area studies through time. Even relatively wide swath sensors, such as Landsat-8, often cannot cover the entirety of large ecosystems within a single overpass, and so BRDF differences in multiple images through time are inevitable. It is important to note that other results in this chapter, such as the sensitivity of specific spectral regions as indicators of red stage conifers, the importance of specific fine spectral details, the importance of data from various seasons, and the effects of feature reduction are unlikely to be affected by the use of airborne versus spaceborne data or other noted contributors to the relatively lower classification accuracy in this study.

3.4.3. Comparison with Ancillary Data

There is no perfect red stage conifer identification dataset for comparison. ADS, in addition to being a visual estimate, often use polygon sizes that are challenging for comparison with the 30 m classification results. Small ADS polygons (1-5 ha) of very intense mortality were generally in good agreement with the results. However, ADS polygons were often large and provided only the average amounts of dead trees per ha over

10's or even 100's of ha, whereas dead trees in these polygon tend to exhibit strong spatial clustering. As a result, a polygon with a reported high (average) number of dead trees per ha, could include many 30 m pixels with no mortality. Figure 3.7 illustrates this point, as the ADS identifies the scene on the left of the figure as having 37 dead trees per ha and the scene on the right as having 98 dead trees per ha (both ADS estimates made as part of much larger polygons). However, the WorldView imagery, which was acquired within a month of the ADS, shows mostly visibly green trees with scattered mortality.

Figure 3.7, particularly the scene on the right, shows an overall tendency for the classification to model red stage mortality on a larger area than it is actually occurring in. Considering red stage mortality was by far the most spatially rare class in 2015, but an equal amount of training pixels for this class were given to the RF classifier as the other two classes, some bias towards classifying more red stage mortality than is actually existent is logical. In Figure 3.7, and in other parts of the study area examined at a fine spatial scale, red stage mortality is most commonly erroneously mapped in areas with a sparse conifer canopy, often adjacent to actual red stage mortality. Understory vegetation in these areas are likely also dying back, creating a confounding spectral signal.

From a broad spatial perspective, conifers generally have the highest leaf area index and biomass in my study area, and I expect this to be linked to high canopy moisture levels. Therefore, the fact that the highest CWC values occur in areas I classified as conifer, is a positive result for the accuracy of my classification (Figure 3.6). In theory, I would also expect red stage mortality areas to both lose more canopy moisture between 2011 and 2015, and have lower CWC levels in 2015 than healthy conifer counterparts. This is consistent with my findings in Table 3.5, however, the differences in averages is not as large as one

might expect when comparing live and dead trees. It is important to remember that CWC and PWS are also model outputs, and not direct measurements. Whereas it is clear from Asner et al., 2016 and Figure 3.6 that these outputs are robust at a broad scale, Figure 3.7 demonstrates that the PWS output does not always clearly respond to overstory mortality at the finest spatial scale. One possible explanation is this is due to confounding changes in CWC in other plants within the pixel. Remaining plants in areas where some or most of the overstory vegetation has died may have less competitive pressure and therefore a less extreme CWC change than areas with live overstories, balancing out the CWC change due to overstory loss.

Overall, all data sources focused on the 2012-2015 drought's impact on Southern Sierra forests demonstrate the enormous scale of the drought and tree mortality, and therefore the need for high-temporal high-quality monitoring via remote sensing and other methods.

3.5. Conclusions

In this study, I tested the ability of a supervised classification scheme to identify areas of tree mortality over a large landscape using data equivalent to what would be collected by a spaceborne imaging spectrometer. I tested the effect of varying different aspects of the feature inputs given to the classification scheme on the overall accuracy. Feature inputs that were varied included the temporal information (both seasonality and whether a time series of images was included), the spectral information (multispectral versus imaging spectroscopy), and whether feature reduction was used or not. I observed weighted overall accuracies of 63.4% or better across all classifications; however, classification based on imaging spectroscopy data performed significantly better than comparable classifications based on multispectral features, and feature reduction generally improved the accuracy of the

classification further. I also found that multi-temporal imagery that included the ability to compare seasonal variations in spectral signals positively affected accuracy, with classifications that had different late-drought seasonal inputs generally outperforming feature sets that did not. Cross-track reflectance differences between flight lines were likely a major source of error in my classification. However, a spaceborne imaging spectrometer with a wide field of view would allow for large scale ecosystem monitoring without this error source. Although the difference between the overall accuracy of the best performing multispectral and imaging spectroscopy data was only 4.9% (85.1% for imaging spectroscopy and 80.2% for the multispectral imagery), this study, combined with others, demonstrates yet another of the wide variety of applications in which a spaceborne imaging spectrometer might add greater understanding to earth system changes and processes. A series of images spanning a longer time period, realistically feasible only with a spaceborne imaging spectrometer, would likely further enhance the power of the imaging spectroscopy based change detection demonstrated in this study.

Chapter 4: Using Combined Airborne Imaging Spectroscopy and Lidar to Describe Disturbance at the Individual Tree Level in a California Watershed

Zachary T. Tane[1,2], Dar A. Roberts[1], Michael L. Goulden[3], Carlos M. Ramirez[2]

[1]University of California Santa Barbara, Department of Geography

[2]United States Department of Agriculture, Forest Service, Pacific Southwest Region, Remote Sensing Lab

[3] University of California Irvine, Department of Earth System Science

4.0. Abstract

Between the years of 2012 – 2016, California experienced an extreme drought, which resulted in widespread tree mortality. In June 2013, before tree mortality had become epidemic, airborne high spatial resolution imaging spectroscopy and lidar were acquired over a 2,240 ha watershed in the Southern Sierra Nevada. I used this remote sensing data to create a model for pre-disturbance canopy-level species and height distribution for tree crowns above 15 m in height. Using high-spatial resolution multispectral imagery acquired in 2016, drought induced canopy mortality was estimated. A Monte Carlo simulation was used to propagate error between these estimates and evaluate uncertainty. I found survival to be highly variable among conifers, with an estimated 17.6% of ponderosa pine surviving from 2013 to 2016, compared to 67.7% of incense-cedar surviving. I found trees to be dying at about equal rates across height classes with trees 15 – 35 m in height having a 25.4% chance of survival, compared to a 24.7% chance of survival for trees taller than 35 m. Overall, the impact of the drought and associated mortality was to reduce the number of live conifer crowns from an estimated 77,067 stems to 19,451 stems between 2013 and 2016.

4.1. Introduction

Large swaths of forest across the globe are experiencing escalating tree mortality coincident with increasingly severe and warm episodic drought (Allen et al., 2010; Choat et al., 2012). California experienced an extreme drought between 2012 – 2016, including a period of low of precipitation and high temperatures during the hydrological years of 2012 – 2014 that was among the most extreme in the last 500 years (Diaz and Wahl, 2015; Robeson, 2015). The drought had an enormous impact on the state's forests, with extensive canopy moisture loss (Asner et al., 2016) and widespread tree mortality starting in 2014 (*R5-PR-034, 2016 Aerial Survey Results: California*, 2017). California's forests provide a range of cultural, biological, and recreational resources to the state's 40 million residents and additional tourists (Chornesky et al., 2015). California's forested watersheds are also the source of much of the state's water and the trees contain millions of tons of carbon in biomass (Hudiburg et al., 2009; Lutz et al., 2017). Climate model projections generally predict increasing precipitation variability over the next 50 - 100 years, with more extreme drought, both worldwide and in California (Bates et al., 2008; Berg and Hall, 2015; Cayan et al., 2010). These droughts will coincide with warmer temperatures, making California's 2012 - 2016 drought illustrative of the potential impact of drought on forests expected in the mid to late 21st century (AghaKouchak et al., 2014; Diffenbaugh et al., 2015).

Drought-driven tree mortality is often unevenly distributed by species, demographic class, and microsite; an improved ability to quantify the biotic and landscape distribution of mortality is needed to better diagnose the causes of dieback and to determine and predict the impact on ecosystem services such as carbon sequestration (Ganey and Vojta, 2011; Lutz et al., 2012; Mueller et al., 2005; Van Mantgem and Stephenson, 2007). For example, large

trees, which are disproportionately important for services such as carbon storage and wildlife habitat (Lutz et al., 2012), may prove more vulnerable to drought as a result of hydraulic or age constraints or insect foraging preferences (Mcintyre et al., 2015), or less vulnerable as a result of rooting depth and occurrence in favorable microsites (Kolb et al., 2007). Preferential mortality of large trees could increase, and preferential survival decrease, expanding the ecological impact of drought beyond what would occur with uniform mortality. Similarly, disproportionate mortality or survival across species could rapidly shift community composition, with implications for services that are strongly controlled by species effects (Ellison et al., 2005; Kelly and Goulden, 2008; Mueller et al., 2005). However, large trees and some tree species are spatially rare, making it difficult to adequately sample the demographic and community distribution of mortality (Lutz et al., 2012). This points to the need for a sampling approach that is capable of capturing variation in species, height class, and vigor.

Airborne remote sensing is one means of achieving this need. For example, airborne lidar has been shown to provide accurate information on stand structural characteristics such as tree height, biomass, and canopy shape (Andersen et al., 2006; Dubayah and Drake, 2000; Edson and Wing, 2011; Gonzalez et al., 2010; Lefsky et al., 2002; Lim et al., 2003). Another possible tool is airborne VSWIR imaging spectroscopy, where a sensor measures radiance at fine (<20 nm) spectral sampling intervals from 400 to 2500 nm. Imaging spectroscopy has been shown to be capable of creating products for a diverse set of ecological uses, including identifying surface mixtures within a single pixel (Roberts et al., 1993), analyzing canopy water content (Gao and Goetz, 1990), and detecting a broad suite of biophysical and biochemical leaf properties of plants (Asner, 1998). The greater spectral detail imaging

spectroscopy provides has also been demonstrated to be useful for identifying the plant functional types (Ustin and Gamon, 2010) and mapping plant species (Martin et al., 1998; Paz-Kagan et al., 2017a, 2017b; Roth et al., 2015).

The combination of airborne high-spatial resolution VSWIR imaging spectroscopy and lidar has been shown to be particularly powerful for ecological analysis (Asner and Martin, 2009; Koetz et al., 2007). From the perspective of species classification, the ability to first create crown canopy objects using lidar and then classify the object based on imaging spectroscopy has been shown to be an effective way of leveraging both data sets for high accuracy (Alonzo et al., 2013; Dalponte et al., 2008; Ghosh et al., 2014). Combined lidar and imaging spectroscopy can also be used to create continuous maps of individual tree species and structure (Koetz et al., 2007). The high accuracy global positioning system (GPS) inherent in lidar remote sensing systems allows for excellent georeferencing, which facilitates the comparison of pre- and post-disturbance datasets and allows tracking of individual crown mortality over time. However, putting together varying data sources, processing models, and outputs, each with its own errors and biases, can cause error proliferation issues to the detriment of a final product.

In this study, I evaluated patterns of canopy mortality due to drought by species and height class. To achieve this, I created an ecological baseline using a combination of airborne high-spatial-resolution imaging spectroscopy and lidar acquired in a southern Sierra Nevada watershed before drought-induced mortality became extreme. I then used high-spatial resolution multispectral imagery acquired in 2016 to analyze the canopy change due to drought. I performed this analysis in two contexts; first, a spatially explicit model of tree crowns was created. Next, a Monte Carlo simulation was used to propagate error and

quantify the statistical significance of observations change by tree species and height class across the project area. I hypothesize that canopy change is non-random with respect to tree species and height class, and seek to accurately describe these changes at the individual tree canopy level.

4.2. Methodology

4.2.1 Study Area

I focused my work on the Soaproot field site, which was established by the Southern Sierra Critical Zone Observatory (SSCZO; Goulden et al., 2012) and is also part of the NEON (Kampe et al., 2013). The site is located on the west side of the Sierra Nevada with elevation ranging from 1000 to 1500 m. The climate is Mediterranean, averaging between 800 and 900 mm of precipitation yearly, with an average temperature between 13 and 15 C. The region consists of a lower montane forested ecosystem that has areas that are mainly hardwood forests, with the dominant species of hardwood being California black oak (*Quercus kelloggii*) and canyon live oak (*Quercus chrysolepis*), and areas that are mainly conifer forests, dominated by ponderosa pine, with less abundant incense-cedar, sugar pine, and white fir.

Several studies indicate the entire west-side of the southern Sierra Nevada to have been heavily impacted by drought and tree mortality in 2015 and 2016 (Asner et al., 2016; Young et al., 2017). Aerial survey data indicates the study area has had a high number of dead trees per unit area identified on it, but not an exceptional number for the elevation range in the Southern Sierra Nevada, (*R5-PR-034, 2016 Aerial Survey Results: California*, 2017).

4.2.2 Remote Sensing Data Pre-Processing

4.2.2.1 Instrumentation and Pre-Processing of 2013 Remote Sensing Data

Approximately 2,240 ha of the Soaproot field site was flown by NEON's Airborne Observation Platform (AOP) on June 2013. The NEON AOP had three remote sensing instruments on it: an Optec Gemini small-footprint waveform-recording lidar with 2-4 pulses per square meter, an imaging spectrometer that sampled between 380-2510 nm with a 5 nm sampling interval at 1 meter on a side pixel size, and a color camera with approximately 0.11 m on a side pixel size. Due to the size of the project area and the relatively narrow field of view of the equipment, multiple flight lines were required to cover the entire study area. 415 ha of the area flown was excluded from analysis because it had either been mechanically thinned or burnt through prescribed fire between 2013 and 2015, leaving 1,825 ha (Figure 4.1). See Kampe et al. (2013) and Kampe et al. (2010) for a full summary of the remote sensing equipment used as part of the NEON AOP.

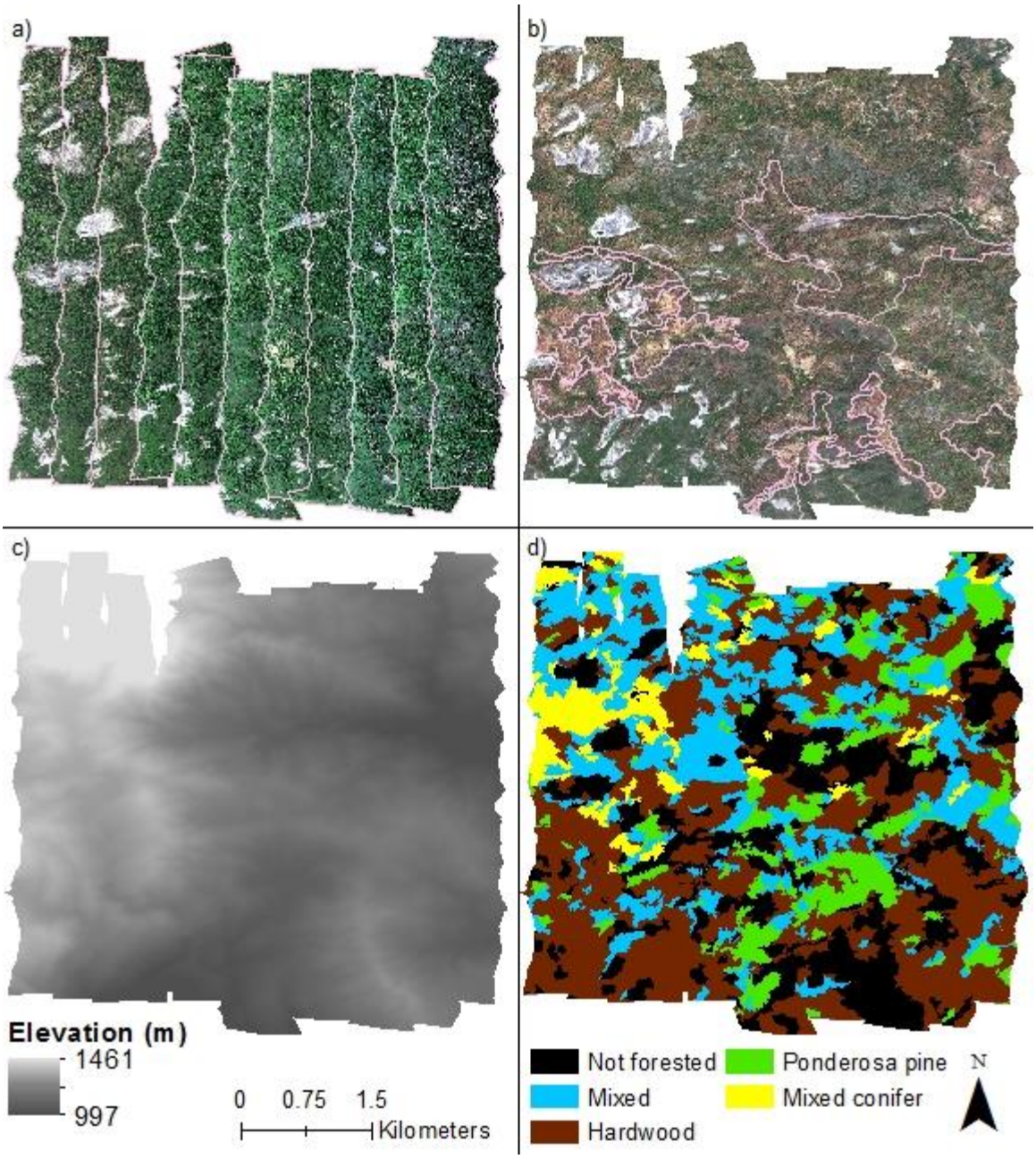

Figure 4.1. a) True color mosaic of imaging spectroscopy data acquired 12 June 2013 as part of the National Ecological Observation Network. Magenta lines represent individual flight lines for imaging spectroscopy data collection. b) WorldView imagery acquired 9 July 2016. Magenta lines represent areas that were control burned or mechanically thinned between 2013 and 2016. c) A digital elevation map of the study area, generated from 2013 lidar data with higher elevations designated with lighter colors underlies this figure. d) US Forest Service vegetation cover map. 'Not forested' represents any one of the following: chaparral, grasslands, or rock. 'Mixed' represents a mixture of hardwood and conifer tree cover. 'Mixed conifer' represents areas that are some mixture of firs and pines.

The publically available level 2 waveform lidar data and imaging spectroscopy reflectance products, released as part of the ongoing NEON project, were used as inputs in

this study. The lidar data were pre-corrected for aircraft movement using an on-flight positioning and orientation system (POS). For the imaging spectroscopy data, the sensor was first laboratory calibrated to National Institute of Standard and Technology (NIST) standards and the raw in-flight measurements were converted to absolute radiance using the laboratory calibration results (Kampe et al., 2013, 2010). Orthorectification was then performed using onboard POS and the earth gravitation model 1996 earth geoid. The data were then converted from radiance to reflectance using the ATCOR-4 atmospheric correction algorithm, with topographic inputs given from the NEON processed LIDAR data and position inputs given from the onboard POS system (Karpowicz et al., 2014).

4.2.2.2 Instrumentation and Pre-processing of the 2016 Remote Sensing Data

In order to characterize the late drought effects, a fine resolution multispectral WorldView-3 image acquired on 9 July 2016 with approximately 1.26 meter resolution was used (http://www.digitalglobe.com). The image was converted from radiance to reflectance using the ATCOR-4 atmospheric correction algorithm. The WorldView satellite is pointable (capable of taking images off-nadir) and the image for this scene was taken at an angle of 14.2 degrees of nadir. In order to correct for the errors in georeferencing due to the off-nadir image distortion and other sources, 113 ground control points were manually collected comparing the WorldView imagery and 2013 NEON AOP data. The WorldView imagery was then subsequently warped using Delaunay triangulation. The methods do not allow for a direct calculation of error, but a subjective visual comparison of the images after warping indicated there was generally less than 1 pixel (1.26 m) error.

4.2.3 Creation of a Spatially Explicit Tree, Species, and Mortality Model

4.2.3.1 Overview

Once pre-processed, goals for the remote sensing data were to: 1) Create a digital canopy model (DCM) from the lidar data, and use the DCM to identify individual trees, and some basic physiological information such as the canopy extent and height of the individual trees above 15 meters in 2013; 2) Using the imaging spectroscopy data and a machine learning algorithm, make a spatially explicit map of the species of the individually identified tree crowns; and finally, 3) using 2016 WorldView imagery identify whether those same tree crowns were alive or dead in 2016.

4.2.3.2. Lidar Data

In order to differentiate individual treetops within a lidar point cloud, waveform lidar data were tiled and processed in ENVI 5.2 (Harris Geospatial Solutions) using Idaho State University's publically available Boise Center Aerospace Laboratory (BCAL) LIDAR extension (Streutker and Glenn, 2006). In order to generate a 1 m digital elevation model (DEM) and DCM, height filtering was done in BCAL using 13-meter window and a natural neighbor algorithm. Fusion Lidar's (US Department of Agriculture, 2009) canopy maxima function was then used to identify tree canopy tops and separate them from other local maxima (the shoulders of a tree). The function necessarily makes assumptions about the size and shape of tree canopies to determine the search window to exclude other local maxima. Since previous studies have identified the mortality in this area to be primarily occurring amongst conifers (Paz-Kagan et al., 2017a), I assigned search window coefficients which were heuristically derived to fit a conifer's shape and worked well in the study area (the following parameters were used for the quadratic formula that determines search window size: A=2.75, B=-0.012, C=0.0021, D=-0.00007). However, since broadleaf trees in the area have radically differing canopy shape from conifers, it was unavoidable that the model did

not delineate broadleaf canopies as well, generally dividing a single broadleaf tree crown into multiple crowns. For this reason, beyond the general location of broadleaf canopies, model results will focus on conifer crowns.

Once tree crowns were identified, tree canopy extents were then determined in ArcGIS 10.4 by inverting the DCM and then using the watershed tool, with the individual treetops as the pour points (Edson and Wing, 2011). Canopy base heights were not allowed below 10 m to prevent canopies from erroneously extending into the understory. I found trees with tops below 15 m were increasingly error-prone with these methods, so I limited my analysis to treetops above this height threshold.

In order to test the accuracy of the classification, I created a grid of 62 m by 62 m squares across the study area and then randomly selected 115 squares. Within each square, using a combination of the lidar DCM and the NEON high-resolution aerial photography, individual conifer tree crowns were manually delineated. I only evaluated conifer accuracy, since the individual tree top identification search window parameters given to FUSION were for conifer crown shape. I then compared the algorithm's canopy delineation performance with manual delineation to assess UA, PA, and overall count accuracy (OCA, e.g. how much the classifier is over or under estimating the number of trees in the study area) using the equations outlined in Radoux and Bogaert (2017).

4.2.3.3. Imaging Spectroscopy Data

Bands within spectral regions that are highly associated with water vapor absorption or otherwise have a low signal-to-noise ratio (bands below 400 nm, between 1310-1430 nm, and 1800 -2000 nm) were discarded from further processing, leaving 373 of the original 432 bands. Next, continuum removal, as implemented in ENVI 5.2 (Harris Geospatial

Solutions), was used on the L1 imaging spectroscopy reflectance products (Kokaly and Clark, 1999). The continuum removal process divides each pixel's spectrum by its convex hull. The results of continuum removal have previously been demonstrated to enhance the reflectance signal of structural and biochemical properties of plants while reducing the impact of shade, topography, and the BRDF differences between and within individual flight lines (Youngentob et al., 2011).

4.2.3.4. Species Classification

Collection of Species Level Training and Validation Data

As part of the NEON project, the spatial location of trees were identified via GPS with species, height, and other information about each individual tree also collected. In addition, some United States Forest Service (USFS) plot data that measured species, height, and tree location was collected in 2013 using Trimble Geo XT GPS units and laser range finders to record exact tree location. Both of these data sources were used in this study when the field identified tree location and tree height measurements made the unambiguous location of trees within my DCM possible. However, field samples alone did not provide sufficient data for all the tree species within the study area, so auxiliary data sources were needed.

The main road that bisects the study area, Big Creek Road, was imaged with Google Street View© in 2007, providing another supplemental data source. Google Street View images were of high enough quality that confident classification of tree species was possible, and based on the GPS location in Google Street View and the surrounding vegetation structure, trees could confidently be relocated in Google Maps© and in the NEON AOP data (Figure 4.2). Aerial photography is another possible data source. Although not all species are readily separated through aerial photography, the canopies of broadleaf

trees and sugar pine specifically distinct enough from other species and therefore identifiable via the NEON AOP's high-resolution true color images and the DCM (particularly when supplemented with Google Earth© imagery). All Broad leaved trees were group into a single "oak" class since species could not be discriminated. Since it is possible to identify a large number of trees via aerial photo interpretation, a pre-determined number of broadleaf and sugar pine trees were collected to avoid bias. The number selected reflected the species proportional abundance on the landscape compared to the number of trees of each species already identified by other methods (as estimated from Forest Service vegetation cover maps, Figure 4.1d).

With all of the data sources assembled into a single database, a predetermined number of trees were selected for each species to be used as inputs for species classification algorithm; this number was based on the abundance of the trees on the landscape and the average number of pixels per tree crown. Trees were then randomly assigned to be used for training, ignoring the method of collection (Table 4.1). Trees not assigned for training were used as independent validation data to estimate UA, PA, and OA, and inform the Monte Carlo simulation.

Table 4.1. The number of trees for each species used for training (T) and validation (V) by collection method.

	Incense-cedar		Oak		Ponderosa pine		Sugar pine		White fir	
	T	V	T	V	T	V	T	V	T	V
Field	10	2	3		19	25			6	1
Google Street View	26	13			19	30			17	15
Aerial Photo			44	37			7	15		
Total	36	15	47	37	38	55	7	15	23	16

Figure 4.2. The process for the collection of training and validation data via Google Street View ©. a) 2007 Google Street View of Big Creek Road, using this information source tree species can accurately be obtained. b) The satellite data available from Google Maps can, in combination with Google Street View, be used to obtain the precise location of the tree. Google Maps imagery was then compared with 2013 high-resolution true color images (c) and lidar digital canopy model (d). In each panel, the red arrow indicates the location of the same sugar pine.

Object Creation and Masking

Classification was done at the object scale using pixel class majority within the object, this has been shown been shown to improve accuracy and reduce the impact of pixel-level variation within classes (Alonzo et al., 2013; Dalponte et al., 2012). My classification used tree crowns objects created as described in Section 4.2.3.2, after filtering out any pixels with normalized difference vegetation index (NDVI) scores below 0.6. If less than 25% of the pixels within the canopy object had an NDVI score above 0.6, the pixel was not classified

and instead was labeled as being dead in 2013. In accordance with these methods, validation data were assessed at the whole tree crown object level. As recommended by Dalponte et al. (2014), the canopies of trees selected to be the source of training pixels were manually delineated based on the lidar DCM. No other tree crowns used in this study, including the tree crowns selected for validation were manually delineated, with one exception. For white fir, which is a species of tree that is relatively rare within the study area, there were few trees identifiable via Google Street View or field sampling in the study area. However, several trees were identifiable in Google Street View inside the area scanned with imaging spectroscopy, but outside of the more narrow area scanned with lidar. For these trees only, tree crown extents were manually identified using the imaging spectroscopy data and high-resolution aerial images.

4.2.3.4.3. Classification Algorithm

Species classification was performed using the RF classification algorithm (Breiman, 2001), as implemented in R 3.2.2 using the R package randomForest 4.6 (Liaw and Wiener, 2002). The RF algorithm is non-parametric in its assumptions and is generally thought to perform well in high-dimensionality space; the RF algorithm is therefore often used for remote sensing applications (Belgiu and Dragut, 2016) including for species classification of imaging spectroscopy data with good accuracy (Dalponte et al., 2012; Fabian E. Fassnacht et al., 2014; Ghosh et al., 2014; Naidoo et al., 2012)

RF is an ensemble classification method where a user-determined number of individual CTs are used to make a classification determination; each CT is given a subset of training data equal to the actual training data amount but determined by sampling with replacement from the entire training data population. At each split in each individual CT, the tree is given

a user-determined subset of the total features (in this case, imaging spectroscopy bands). For this study, 500 CTs were used as a part of the RF algorithm and 19 bands were given at each split (19 being the whole number closest to the square root of the total number of bands), both of these parameters are commonly used in RF implementations on remote sensing data and generally yield good accuracy (Belgiu and Dragut, 2016).

4.2.3.5. Evaluation of a Tree's 2016 Status

To create a spatially explicit map of mortality in 2016, three possible classes were desired for each WorldView pixel: green vegetation, red-stage vegetation, and shade. To collect data for these classes, 50 random points across the study area were created. At each point, I identified the four closest pixels in each of the three classes, thus identifying a total of 200 pixels per class. Based on these training pixels, a MLC was then used across the WorldView image. The classification was then assessed at the conifer crown object level; if 75% or more of the crown object was classified as shade the conifer was identified as shaded; otherwise, the conifer was determined to either be green or red based on majority classification of the tree crown object.

In order to validate this map, tree crowns were selected for manual review by an image analyst. For use in the non-spatially explicit model (described in Section 4.2.4.1), it was deemed desirable that samples adequately sample each species and height class within seven height classes ranging from 15 – 20 m to 45 m and above. In order to accomplish this goal, a pre-determined number of tree crowns were drawn from each of the species classes (species determined in Section 4.2.3.4). For all species but ponderosa pine, some additional trees were randomly selected within the taller height classes to assure that all heights were sampled adequately. In total 2632 ponderosa pine, 440 incense-cedars, 182 white firs, and

196 sugar pines were selected for sampling. For manual validation, trees could be labeled as either being live in 2016, dead in 2016, or shaded, with dead trees including red stage mortality in 2016 or fallen in 2016. Some trees were not classifiable for reasons including the tree had a visibly dead top but still green lower canopy or the tree's crown looked pale but it could not be determined whether that was due to illumination effects or actual foliar discoloration.

4.2.4 Evaluation of Mortality Effects by Species and Height Class

4.2.4.1 Overview of the Monte Carlo Simulation

One goal of my study was to create estimates for tree abundance in 2013 by species and height class and repeat those estimates in 2016 taking into account mortality due to the drought. Since the workflow used in this study to perform these tasks required multiple interconnected estimates, issues of individual errors, bias, and error propagation need to be accounted for. The workflow previously presented in Section 4.2.3 repeatedly uses independent validation data to provide an estimate of error at each individual step. However, a more holistic approach is needed to unite these data sources into single model that is capable of estimating each tree species' abundance across the study area in an accurate and unbiased manner and the uncertainty inherent in these estimates. To this end, a Monte Carlo simulation was used. The primary input into this simulation was a non-spatial database of tree crowns in the study area with the species and height noted. This was created from a combination of the results of the tree crown delineation algorithm, DCM, and species classification. Within each Monte Carlo iteration, various independent validation datasets were used to estimate and adjust for specific errors impacting the initial database (Table 4.2). As a final product, each iteration creates a new estimate for the number of live trees in

2013 and 2016 by species and height class. The Monte Carlo simulation was run 1,000 times and standard deviation of the results were used to measure model uncertainty.

Table 4.2. Workflow for a single iteration of the Monte Carlo simulation. In the table, probability distribution function is abbreviated to PDF, overall count accuracy is abbreviated to OCA. The exact data that was used as inputs is detailed in Appendix 4.

	Input	Process	Output
Step 1	1. Total number of tree objects in each species class (source: the spatial model) 2. Error matrix of species classification (source: classification validation)	Generate percent of trees misclassified for each species from PDFs generated from error matrix, then estimate number of misclassified trees by species	Estimated number of trees misclassified by species
Step 2	1. Step 1 output 2. Database of trees objects with species and height information (source: the spatial model) 3. Histogram of tree heights by species (source: the spatial model)	For each misclassified species / actual species pair, generate tree heights randomly from the actual species' height distribution to select trees to reclassify	Updated 2013 tree object database with species corrected for classification error
Step 3	1. Step 2 output 2. Mean and standard error of OCA of crown objects (source: object classification validation) 3. Histogram of tree heights of missed crown objects (source: object classification validation)	Generate an OCA value from the PDF of OCA value, then. using the height distribution of the missed tree objects, randomly select trees to duplicate	Updated 2013 tree object database corrected for object creation error
Step 4	1. Mean and standard error of tree survival rate by species and height class (source: manual review of randomly selected 2016 tree crowns)	Generate estimate of tree survival rate by species and height class from individual PDFs	Initial estimate of survival rates between 2013 – 2016
Step 5	1. Step 1 output 2. Step 4 output	Modify survival rates to account for species misclassification using the number of trees misclassified by species and height class	Adjusted estimate of survival rate between 2013 – 2016
Step 6	1. Step 3 output 2. Step 5 output	Generate a 2016 live tree database using 2013 database and 2013-2016 survival rates	Database of 2016 trees by species and height class

4.2.4.2 Overview of the Monte Carlo Simulation Workflow

A major source of error in the non-spatial crown object database is misclassification of species due to errors in the species classification algorithm. Frequently in remote sensing based classifications of land cover, independent validation data are used to adjust for classification error via design-based inference (Olofsson et al., 2014). However, since the

validation data in this study was not sampled probabilistically across the study area, was not acquired in a manner representative of the abundance of species according to the classification maps, and is based on objects, the use of design-based inference here would be improper. In Table 4.2, the goal of step 1 of the Monte Carlo process is to estimate the number of misclassified trees by species using the independent validation of the classification discussed in Section 4.3.4.1.2. In order to do this, I calculate the probability of a reference tree being classified as any given class as:

$$\boldsymbol{p_{ij}} = \frac{\boldsymbol{N_{ij}}}{\boldsymbol{N_{.i}}} \quad (4.1)$$

where P_{ij} is the probability of a tree of reference species *i* being classified as species *j*, N_{ij} are the number of validation tree crowns of reference species *i* classified as species *j*, and $N_{.i}$ are the total number of validation tree crowns of reference species *i*. I calculated the standard error of P_{ij}, denoted as $\sigma_{\bar{P}ij}$, as:

$$\sigma_{\bar{P}ij} = \sqrt{\frac{P_{ij}*(1-P_{ij})}{N_{.i}}} \quad (4.2)$$

Using these values and a Gaussian distribution, probability density functions (PDFs) of the probability of any tree classified as class *i* actually being class *j* were calculated (see Appendix 4 for the specific parameters used as inputs here and throughout the Monte Carlo simulation). In each Monte Carlo iteration, the total number of trees in each species class, determined from the non-spatial tree crown object database, were combined with the values selected from the PDF to estimate the number of misclassified trees of each species and their true species. This is done iteratively, by first randomly selecting one class, then estimating the number of trees across the study area that are classified as being that species, but actually are a different species (these will be referred to as false positives henceforth). By subtracting

the false positives from the total number of trees classified as the species in the spatial model, the number of correctly classified trees can then be estimated. The estimated number of correctly classified trees is combined with the probability matrix to estimate the number of trees that belong to that species, but were incorrectly classified as another species class. This process is repeated for each species, adjusting the number false positives by species at each iteration until a matrix of the estimated total number of trees is calculated.

Since one goal of the Monte Carlo model is to estimate the number of trees in 2013 by height class for each species, an estimate of the height of misclassified species is needed. However, I do not have sufficient validation data to know the actual height distribution of the misclassified trees. In each iteration of the Monte Carlo simulation (step 2 in Table 4.2) this problem is addressed using the height distribution of the "true" class as an estimate for the height distribution of the misclassified trees. For example, one Monte Carlo simulation iteration might estimate there to be a total of 100 trees that were labeled as ponderosa pine, but the true class was incense-cedar. Since the height of these 100 trees is unknown, the height distribution of trees initially labeled incense-cedar is used to randomly select which ponderosa pines to relabel in the object data base. For each Monte Carlo iteration, the outcome of this process is a modified object database where the species of selected crowns in the original are relabeled.

Another major source of error was in crown delineation, when an individual tree crown was improperly designated. Section 4.2.3.2 discusses the use of independent validation data to estimate OCA, a measure of the error in the number of crown objects. The OCA and standard error of the OCA can be used to estimate a PDF for the distribution of the actual OCA value. In addition, as noted in Section 4.2.3.2, the height of crowns that were not

identified by the crown delineation algorithm was recorded. Each iteration of the Monte Carlo simulation (step 3 in Table 4.2) uses the PDF of the OCA value to estimate the number of crown objects over or under estimated by the crown delineation algorithm. Based on the height distribution of the trees missed by the crown delineation, individual tree crowns from the crown object database were randomly selected to be duplicated to represent the missing trees.

Accurate estimates of the trees that are alive in 2016 are also needed. In the Monte Carlo simulation, this was done by estimating the percentage of trees surviving between 2013 and 2016. In order to do this, randomly selected individual canopy objects that were manually reviewed in 2016 were used (the same data that were also used to validate the MLC). For each species and height class combination, the survival rate was estimated using the randomly selected tree crowns and the standard error of the survival rate was estimated using a Bernoulli distribution. These numbers were then used to create a PDF of the probable actual survival rate for each species and height class combination. In each iteration of the Monte Carlo simulation (specifically step 4 in Table 4.2), the PDF for each species and height class combination are used to generate an estimate of the actual survival rate.

Although live or dead tree crowns can be relatively reliably ascertained from WorldView images, the species of the crowns are subject to the same classification errors as the study area as a whole. Without correction, the errors will bias the mortality estimates. The Monte Carlo simulation already estimated the number of trees that were misclassified in each species and height class and the true species (step 2 in Table 4.2). These data were combined with the initial estimated species survival rates (step 4 in Table 4.2) both for the target species and height class and the misclassified species to adjust the survival rate. The

adjusted survival estimates were combined with the record of total 2013 trees by species and height class to create an estimated number of live trees in 2016.

Many of the corrections from the spatial data included in the Monte Carlo simulation were directly created from the validation data. However, two corrections of bias, the correction of misclassified tree's height distribution differing from the original class and the correction in survival rate due to species misclassification were not directly measured. The corrections for these biases were made off of good first-order estimates and assumptions, but the actual accuracy of the corrections cannot be directly measured with the data available. I test the influence of these bias corrections on the results by running Monte Carlo simulations with different assumptions in Appendix 5.

4.3. Results

4.3.1 Evaluation of the Spatially Explicitly Model

4.3.1.1 Canopy Delineation Accuracy Assessment

Comparing the canopy delineation algorithm for conifers with manually identified conifer crowns, I found the crown delineation algorithm to have a UA = 99.6%, a PA = 91.1%, and an OCA = 1.093 (standard error of the OCA was 0.013), indicating on average, for every 1000 trees identified by the crown delineation algorithm, 93 were missed. Overall, the algorithm rarely designated a single conifer crown as multiple crowns or otherwise delineated a tree crown where one was not actually present. However, the algorithm had a tendency to either miss conifer crowns or classify multiple conifers as a single crown. Ignoring errors due to the species classification algorithm, given 73,442 conifer crowns that were delineated by the algorithm in my study area, manual conifer crown classification

would be expected to average of 6,830 more conifers across the study area (standard error of 924 conifers).

4.3.1.2 Species Classification Accuracy Assessment

The spectral profile of the training data for the five canopy level tree species classes reveals there to be some spectral regions with unique patterns and deviations in reflectance for each class (Figure 4.3). Between the oaks and various conifer classes, differences in reflectance corresponded to known patterns of the two plant functional types, with oaks generally more reflective in the shortwave infrared (Roberts et al., 2004). Spectral differences between the varying conifer classes are more subtle and are likely due to a combination of the chemical, leaf structure, and canopy structure properties of the species.

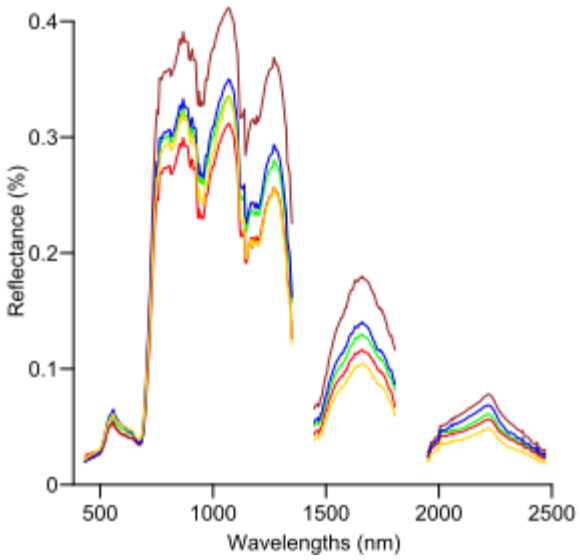

Figure 4.3. The mean spectral profile of the training data for each of the five classes. Blue lines indicate the incense-cedar class, brown lines the oak class, green lines the ponderosa pine class, red lines the sugar pine class, yellow lines the white fir class**.**

OA of the classification of individual tree crowns was 0.86. PA and UA varied considerably between classes (Table 4.3). Oak and ponderosa pine, the two classes that are most common on the landscape and consequently also had the most training data given to the RF classifier, had fairly high PA, but somewhat lower UA, indicating a tendency to overmap those. Rare species, such as sugar pine and white fir, had high UA but comparatively low PA indicating they have a tendency to be undermapped on the landscape.

Table 4.3. Error matrix of the tree crown classification of independent validation data within the study area. PA = Producer's Accuracy, UA = User's Accuracy, and OA = Overall Accuracy.

Class	Ref	Incense-cedar	Oak	Ponderosa pine	Sugar pine	White fir	UA
Incense-cedar		11		1		1	0.85
Oak			36	5	1		0.86
Ponderosa pine		4	1	49	4	1	0.83
Sugar pine					10		1.00
White fir						14	1.00
							OA
	PA	0.73	0.97	0.89	0.66	0.875	0.86

4.3.1.3 Mortality Classification in 2016 Accuracy Assessment

Comparing the MLC with manually classified tree crowns (Table 4.4), reveals the MLC to be fairly effective at discriminating green and visibly dead tree crowns with an OA of 79%. When tree crowns that are classified as shaded either by the MLC or the manual classification are ignored, the OA improves to 89%. The MLC is more likely to label a dead tree as living than a living tree as dead, compared to manual identification. The MLC classifier was also generally much more likely to label a tree as shaded compared to manual classification.

Table 4.4. Error matrix of Maximum Likelihood Classification of 2016 trees status versus manual delineation. PA = Producer's Accuracy, UA = User's Accuracy, and OA = Overall Accuracy.

Class	Ref	Green	Dead	Shaded	UA
Green		780	260	42	0.72
Dead		45	1665	43	0.95
Shaded		99	187	23	0.07
					OA
	PA	0.84	0.79	0.21	0.79

4.3.1.4 Visualization of the Spatially Explicit Model

Subjectively, the spatial location and patterns of tree species in the study area generated by the classification is logical (Figure 4.5a). Oaks are mapped at lower elevations where they would be expected to be common and often in large continuous stands. Ponderosa pine, the most common conifer species, is distributed throughout the study area, particularly at moderate to higher elevations. White fir is found in contiguous regions, primarily at higher elevations. Each of these observations conforms to known species distributions properties. United States Forest Service vegetation cover maps provided an independent source of vegetation cover information that appears to be broadly in agreement with the species classification map (Figure 4.1d). The classification also lacks any apparent 'seams' between individual flight lines or other apparent spatial biases as a result of multiple flight lines being used in a single classification.

Mortality in 2016 (Figure 4.5b) appears heavily focused in areas that were classified as being dominated by ponderosa pine crowns. Areas classified as being predominately oak crowns, as well as large patches of incense-cedar and white fir were less impacted by the mortality. Mortality among ponderosa pine is prevalent throughout the study area.

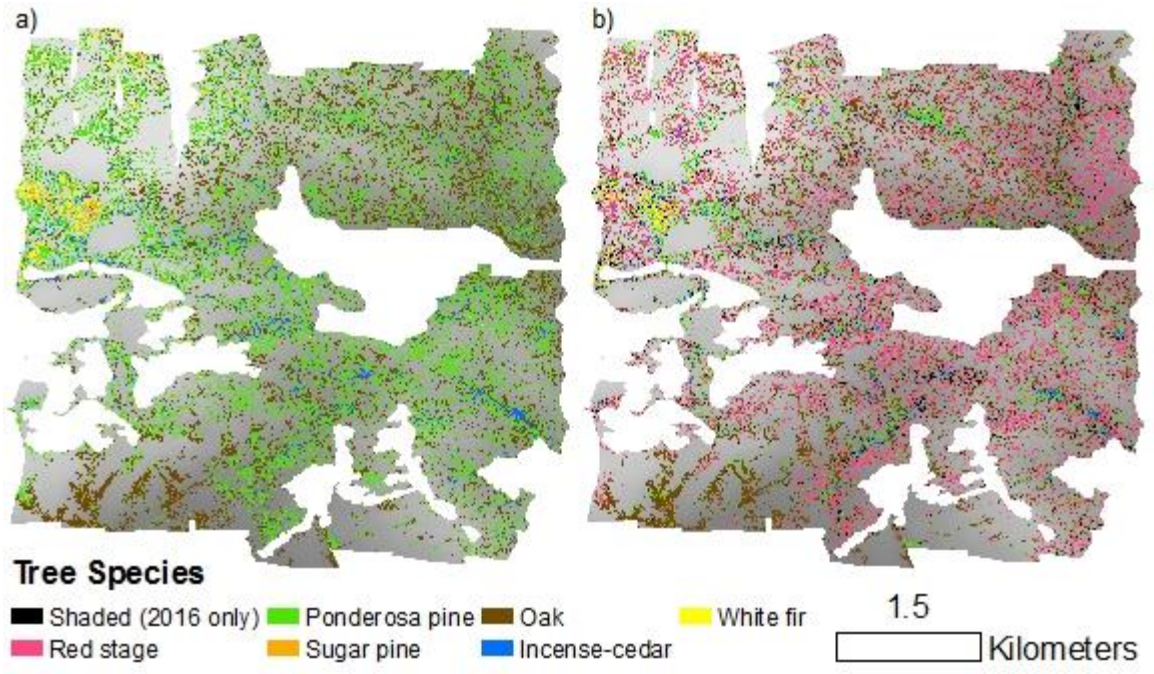

Figure 4.5. a) 2013 distribution of crowns across the landscape as identified by lidar digital canopy model based tree crown delineation algorithm. The species of tree crowns are identified from the imaging spectroscopy based random forest classification. Underlying the tree crowns is a lidar-based digital elevation model, with lower elevations indicated by darker gray and higher elevation indicated by lighter gray. Areas in white are either outside of the study area or were areas that were burnt or mechanically thinned between 2013 and 2016. b) A duplicate of a) with the tree crowns classified as being red stage mortality in 2016 overlaid on top of the map.

4.3.2 The Monte Carlo Simulation

The Monte Carlo simulation results are meant to take into account and correct for the various sources of error and bias in the spatial model. In general, the outputs of the Monte Carlo simulation show trends similar to the spatial model (Figure 4.6). Ponderosa pine was the most impacted species overall, with an average 17.6% survival rate between 2013 and 2016 among the 1,000 Monte Carlo simulations, markedly lower than the average 67.7% survival rate for incense-cedar, 62.5% for white fir, and 42.7% for sugar pine (standard deviation (SD) for the mean of 1,000 simulations = 1.6% for ponderosa pine, 4.0% for incense-cedar, 3.5% for white fir, and 3.6% for sugar pine). There was little change in the survival rate by height class; for conifers overall, the average survival rate was 24.7% for

trees above 35 m (SD = 1.7%) and 25.4% for trees between 15 – 35 m (SD = 1.5%). For ponderosa pine specifically, the survival rate was 18.7% for trees above 35 m (SD = 1.7%), whereas the survival rate of trees between 15 – 35 m was 17.2% (2.1%). Overall, the average of the Monte Carlos simulation runs indicates the number of live conifers above 15 m was reduced between 2013 and 2016 from approximately 77,067 stems to 19,451 stems (SD = 2,685 stems and 1,249 stems respectively; Figure 4.7).

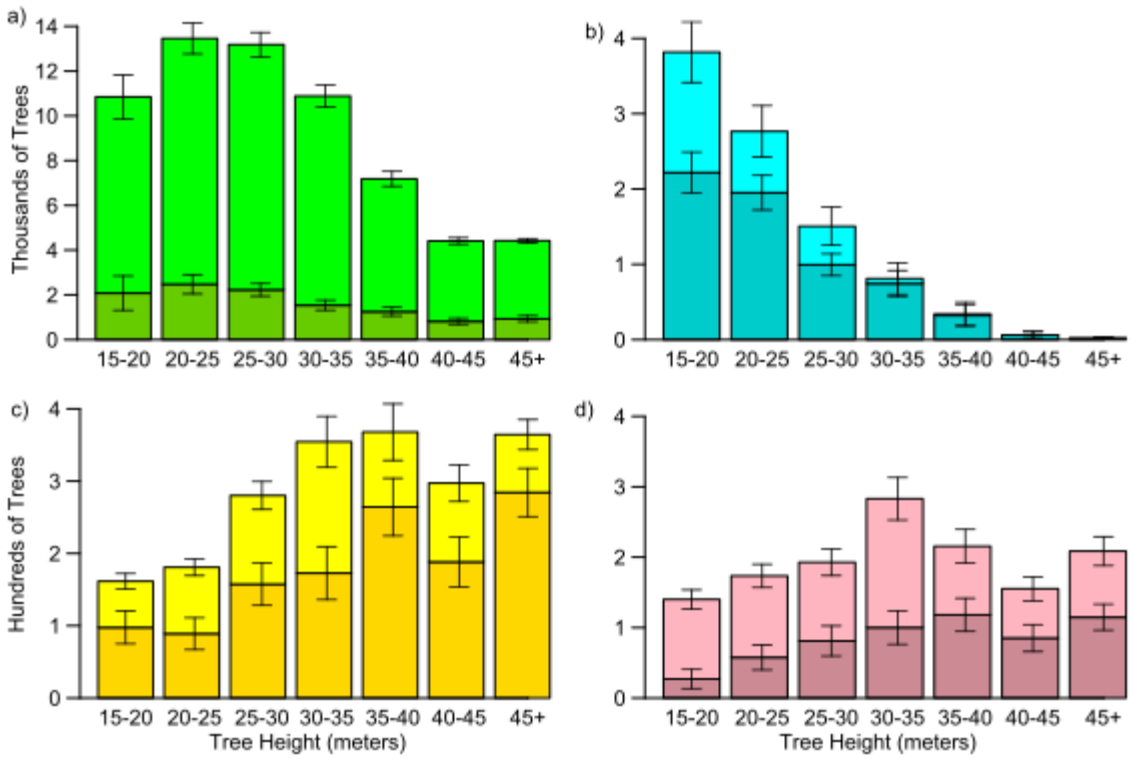

Figure 4.6. Monte Carlo simulation results for the mean number of trees by height class and species in 2013 (lighter colors) and in 2016 (darker colors) for 1000 runs for: ponderosa pine in a); incense-cedar in b); white fir in c); and sugar pine in d). Error bars represent one standard deviation of the results of 1000 runs. Note the y-axis units are different by an order of magnitude between the first and second rows.

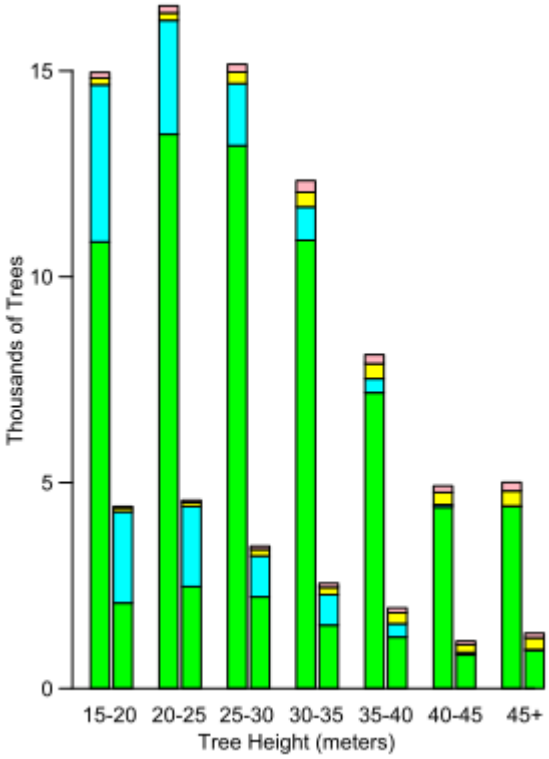

Figure 4.7. Mean change in the number of live trees in the study area by height class and species from 1,000 Monte Carlo simulation runs. For each height class, bars on the left represent 2013 levels, bars on the right represent 2016 levels. Ponderosa pine is represented by green, incense-cedar by blue, white fir by yellow, and sugar pine by red.

4.4. Discussion

4.4.1 Inherent Limitations, Bias, and Potential Error

There are several inherent limitations in the use of remote sensing for the purposes of my study. No lidar based tree crown delineation process, including manual delineation, is able to capture all the trees within complex tree canopies, particularly when some crowns are overtopped by others (Dalponte et al., 2014; Edson and Wing, 2011; Falkowski et al., 2008). The primary influence of the imaging spectroscopy signal is also top of the canopy reflection, so accurately determining the species of trees below the canopy using imaging spectroscopy is not possible. Given the capabilities of the equipment used, I was limited to

describing trees at the top of the canopy. The results of this study are not equivalent or comparable to a theoretical field survey that censused all trees above 15 m within the study area.

There are also sources of error and bias beyond what the Monte Carlo simulation could correct for. The species data used to train and validate the species classification was necessarily acquired in a non-probabilistic manner. Samples were focused in certain geographic regions of the study area and many of the samples were not acquired randomly. Since there is no obvious reason why the selected spectra of species used to train the species classification would be biased compared to the spectra of species in study area as a whole, the data were treated as pseudorandom. Considering the canopy change that has occurred since 2013, I cannot easily collect further field data to test the impact or potential bias introduced by the assumption of pseudorandomness.

Another error source not considered in this study are potential errors in the lidar-derived tree heights. Errors of this nature occur from both failure to locate the exact top of the tree and errors in the DEM that the height measurement is based on, both of which tend to negatively bias lidar-derived heights (Andersen et al., 2006; Lim et al., 2003). The impact of this error source is real, however, it also should not be overstated. Although slightly less accurate than field measurements, lidar-based tree height measurements have still been found to be fairly accurate; for example, the mean error for the lidar derived height of ponderosa pine was found to be less than 0.5 m from true height in Andersen et al. (2006). Correction for this error is also difficult, since most forms of field measurement also have error associated with them, and error is often variable between individual trees and species.

4.4.2 Accuracy and Utility of the Spatial Model

The accuracy of the tree crown level species classification is reasonable compared to other studies exploring combined imaging spectroscopy and lidar for individual species classification (Alonzo et al., 2014; Dalponte et al., 2012, 2008; Ghosh et al., 2014). The low PA of sugar pine, generally due to confusion with ponderosa pine, is logical given the spectral similarity of pine species at the leaf level (van Aardt and Wynne, 2007), as well as sugar pine's diffuse and open canopies. The canopy classification algorithm also performed comparably to previous studies (Alonzo et al., 2014; Dalponte et al., 2014).

The object-based approach for crown delineation and identification had several advantageous properties for the purposes of my study. The crown object level is a more biologically meaningful unit of measurement for change quantification compared to pixel-level changes and allowed for the easy separation from understory changes. The use of crowns objects also allowed for other tree level characterizations to be included in the analysis. In this study, only height was used, but other information such as crown width, crown level vegetation indices, and estimates of biomass are all possible. Figure 4.5 also demonstrates the ability of crown objects to communicate the impact of disturbance spatially and by species in a way that is useful for land managers to plan action in response to the disturbance.

4.4.3 Accuracy and Utility of the Monte Carlo Simulation

The occurrence of extreme drought and widespread forest dieback is unpredictable and rare, and high-quality *in-situ* observations are expensive and typically restricted in space and time; studies that include both pre- and post-dieback observations are consequently unusual (Kolb et al., 2007). Large trees are particularly difficult to sample due to their low density, and the few mortality studies that happen to include pre-mortality surveys seldom include an

adequate collection of large trees (Lutz et al., 2012). The combination of remote sensing and Monte Carlo simulation used in this study provides a preliminary means for analyzing the impact of drought across a range of demographic classes, including large trees. The general approach used here could be extended to address a suite of questions related to investigating tree survival in response to disturbance in a wide variety of ecological settings.

By using the validation data to adjust initial estimates and to simulate the effects of error propagation, the Monte Carlo simulation seeks to create more accurate and less biased estimates of the impact of mortality by species and height class. Since the independent validation data were used as an input into the simulation, no other validation exists within the study; however, the results are in agreement with previous work. For example, I found mortality was unevenly distributed across species, with much higher death rates in ponderosa pine. This bias led to a 30% less ponderosa pine across the landscape than would have been expected with uniform mortality. Though the magnitude of the 2012 - 2015 dieback was more extreme than previous droughts in California, studies of mortality during California's 1988 - 1993 drought in Yosemite (Guarín and Taylor, 2005) and in montane Southern California forests (Savage, 1994) show similar general patterns. Pines are often heavily affected by drought in California, likely due to aggressive bark beetle attacks on stressed trees (Savage, 1994). In contrast, incense-cedar and oaks are more drought tolerant, with oaks having physiological adaptations like deep root systems, xeromorphic leaf structure, and a low water-potential threshold (Abrams, 1992). Other studies of the current drought have drawn similar conclusions as well. Paz- Kagan et al. (2017a) also observed ponderosa pine and sugar pine to be the two most impacted species by the drought. The location of 2016 aerial survey data, as analyzed in Young et al. (2017) also suggests

mortality to be primarily focused in elevational gradients that are strongly associated with ponderosa pine. In Chapter 3, using imaging spectroscopy data in 2015, I also found mortality in areas associated with ponderosa pine.

One area where my model deviates from existing studies is the height of trees impacted. Paz- Kagan et al. (2017a) found mortality to be biased towards taller trees, whereas I found mortality to be essentially unimpacted by tree height. These differing findings may be due to the elevational gradient of the studies. Paz-Kagan et al. cover an elevation gradient between 1,000 – 3,400 m that includes a variety of different species aggregations which were not found within my study area. Since the patterns in mortality by height class appear to be highly species dependent (Figure 4.6), the differing species compositions between this study and Paz-Kagan et al. likely influenced the tree height bias for mortality found.

The focused mortality in ponderosa pine resulted in a rapid change in species cover across the landscape, with possible implications for a range of ecosystem services. For example, a shift from ponderosa pine to oak or incense-cedar may exacerbate the effect of mortality on live biomass. Species that do not typically grow as tall as pines and are slow growing (oaks and incense-cedar) were more likely to survive the drought, whereas the relatively fast growing ponderosa pine had the greatest mortality (Biging and Dobbertin, 1992). This process could compound with additional disturbance. The combination of conifer mortality due to drought and subsequent fire has previously been shown to negatively impact conifer regeneration in the western United States (Harvey et al., 2013).

4.5. Conclusions

The utility of combined airborne high spatial resolution imaging spectroscopy and lidar for mapping crown level species and structure was applied in a change detection context.

While limited to only canopy dominant and codominant trees, I created a model of changes in crown species and height composition due to disturbance at the biologically meaningful unit of the individual tree canopy. I create outputs that are spatially explicit and could be operationally useful for land managers needing to take action in response to disturbance. Trends of drought severely impacting pines have previously been observed; however, I was able to quantify this by creating species and height specific survival rates. Broadly, the techniques used in this study are not site or disturbance specific and could be applied in multiple other settings.

Although disturbances are an important and natural ecological process, the species and structure composition changes in the study area will require decades or longer of tree establishment and growth to approach the pre-drought levels. Mortality is also patchily distributed, with large continuous areas where most or all of the conifers have died, further hindering natural tree establishment. Although caution should be taken in extrapolating the results of the study area to larger spatial extents, aerial detection surveys indicate the mortality levels that occurred in the study area in 2015 and 2016 are not atypical for the Southern Sierra. Disturbances, particularly fire, in the near future could compound species composition change. Continuing, high-quality remote sensing data sets, combined with more field data, will be needed across a wide area to understand future changes in western forests while providing accurate inputs to vegetation models and better inform decision makers.

Chapter 5: Evaluating the Control of Ecological Variables on Bark Beetle Driven Tree Mortality during an Extreme Drought in the Southern Sierra Nevada, California

Zachary T. Tane[1,2], Dar A. Roberts[1], Carlos M. Ramirez[2]

[1]University of California Santa Barbara, Department of Geography

[2]United States Department of Agriculture, Forest Service, Pacific Southwest Region, Remote Sensing Lab

5.0. Abstract

California's Sierra Nevada experienced extreme drought and elevated temperatures between 2012 – 2016, and in the latter years, consequential tree mortality. One of the most impacted trees was ponderosa pine (*Pinus ponderosa*), with much of the mortality driven by native bark beetles (*Dendroctonus spp.*). I identify the relative importance of various potentially influential factors on tree mortality and beetle movement at two separate scales using remote sensing. I group the variables into five categories: biotic, climatic, contagion, individual, and topographic. At the scale of a single watershed, I found canopy structure and composition 45 m around a target tree to be the best predictor of tree mortality of the categories of variables analyzed. Specifically, I found more open stands that are species and size class diverse to be the most resilient to mortality. At the scale of a large portion of the southern Sierra Nevada, I found cumulative precipitation and mean temperature between 2013 – 2015 to be highly predictive of tree mortality. At both spatial scales, trees closer to large groups of trees that had died in previous years were more likely to die in 2016.

5.1. Introduction

Drought induced forest mortality is becoming increasingly pervasive globally (Anderegg et al., 2015; Choat et al., 2012). The impacts of recent high temperatures and exceptional droughts on forests can include permanent canopy level species shifts or conversion to non-forested plant types (Millar and Stephenson, 2015). In the western United States, the rate of tree mortality has been doubling every 17 – 29 years in many places, for reasons that are primarily linked to increased heat and drought stress (van Mantgem et al., 2009). While this increase is partially due to the chronic impact of shifting climate (Das et al., 2016), acute drought events are playing a central role (Clark et al., 2016). Climate models project an increase in drought events accompanied by higher heat in the next 50 – 100 years (Bates et al., 2008).

Across the world, but perhaps most notably in North America, extreme drought can trigger a spike in bark beetle populations and a resultant wave of epidemic tree mortality (Bentz et al., 2010; Raffa et al., 2008). Given the increasing prevalence of drought and subsequent beetle-driven disturbance in North America, a better understanding of the drivers are needed (Clark et al., 2016). There is a growing conceptual framework for the dynamics of bark beetles, drought, and tree mortality at the ecosystem to individual tree level (Anderegg et al., 2015). Untangling the complex interactions of climate, tree density, individual tree stress, and bark beetle populations remains a difficult challenge, however. Part of the difficulty lies in the multiple and widely varying spatial scales of different variables involved. At the individual tree level, genetics, vigor, and local competition play a role in mortality (de la Mata et al., 2017; Fettig et al., 2007). At moderate scales, the local beetle population and the stand microclimate are important (Anderegg et al., 2015; Fettig et al., 2007). At regional levels, water availability and temperature also are involved (Das et

al., 2013; Young et al., 2017). Compounding this, the relative importance of various factors can change with temporal and climatic differences (Van Gunst et al., 2016) and whether bark beetle populations have reached epidemic thresholds (Raffa et al., 2008).

No single method or study will be able to definitively determine the relative importance of each factor under all possible conditions. However, observational studies based on remote sensing have the unique potential to bridge the varying spatial and temporal scales in a way that is not easily achievable with other methods (Edburg et al., 2012; Wulder et al., 2006). Coarse-scale (>30 m pixel size), satellite based remote sensing has the demonstrated ability to evaluate where bark beetle driven tree mortality is occurring over a wide area (Franklin et al., 2003; Meddens et al., 2013), as well as assess the impact of climate and competition on mortality, both for a single event (Young et al., 2017) and through time (Van Gunst et al., 2016). In contrast, spatially-fine scale remote sensing, such as high-resolution multispectral imagery (acquired by aircraft or satellite), airborne lidar, and airborne imaging spectroscopy, can accurately characterize individual canopies. This ability has demonstrated applications to tree mortality, including identifying individual trees killed by bark beetles (Coops et al., 2006; Dennison et al., 2010) and evaluating the relationship of individual trees, tree mortality and the local environment (Baguskas et al., 2014; Paz-Kagan et al., 2017a). The spatial scale of analysis strongly impacts the types of data that can be used. Whereas fine scale remote sensing can detect information at the individual tree level, sampling an entire region is generally cost prohibitive, particularly for airborne instruments (Wulder et al., 2006). In contrast, coarse-scale remote sensing can characterize the impacts of the larger environment. However, measurements of tree density and other biotic variables generally rely on vegetation indices, which are less precise in their ability to describe the local stand

density and structure (Wulder et al., 2006). More integrative approaches are needed to bridge the various scales of remote sensing.

Between 2012 – 2016 California experienced an extreme drought, punctuated by one of the greatest periods of low precipitation and high temperatures in the past 500 years (Robeson, 2015; Williams et al., 2015). In the southern Sierra Nevada, this resulted in a precipitous decline in canopy water content and an increase in tree mortality in 2015 (Asner et al., 2016; Young et al., 2017), which intensified in 2016 (*R5-PR-034, 2016 Aerial Survey Results: California*, 2017). This decline was most acute in pine, particularly ponderosa pine (Paz-Kagan et al. 2017, Chapter 4). In the Sierra Nevada, ponderosa pine mortality due to water stress is primarily associated with bark beetle attack (Oliver, 1995; Williams et al., 2013). These conditions make the southern Sierra Nevada a good case study in the dynamics of bark beetle spread during high beetle population levels and intense drought.

In this chapter, I evaluate the relative importance of factors potentially driving mortality, as analyzed through remote sensing. In order to conduct this analysis, two spatially overlapping datasets were used, one with robust local canopy information and another with less local detail, but which covers a large area. I focus on conifer mortality on the west side of the Sierra Nevada that transitioned to red stage between the summers of 2015 and 2016.

5.2.1. Methods

5.2.1.1. Study Area

A section of the southern part of the west side of the Sierra Nevada range, from 900 to 1500 m above sea level, was used as my study area (Figure 5.1). Several different vegetation types grow within this region, including, depending on local site conditions, chaparral shrublands dominated by manzanitas, California lilac, and California buckeye among others;

oak (*Quercus spp.*) woodlands; and coniferous forests, generally consisting of ponderosa pine as the dominant conifer, but also including incense-cedar, sugar pine, and white fir in the overstory (Storer et al., 2004). The elevation range of this study area was selected to include areas where ponderosa pine was likely to be the dominant species among conifers.

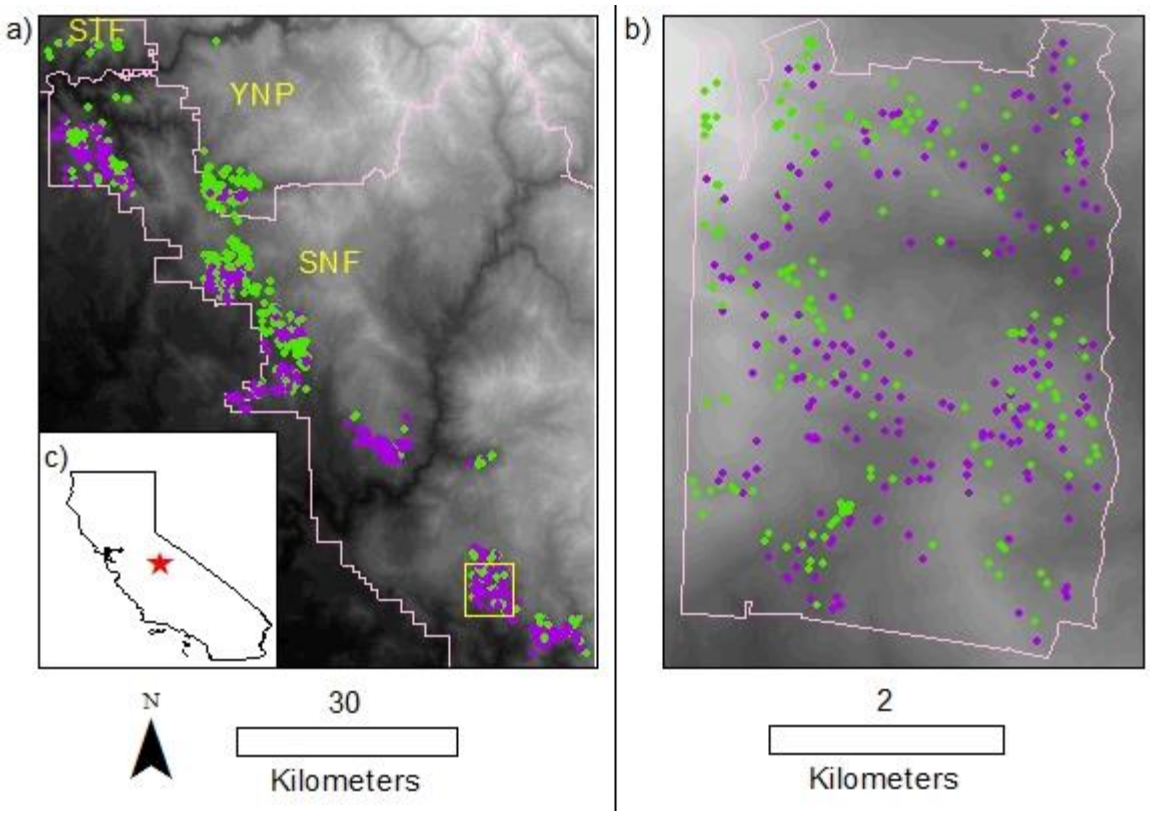

Figure 5.1. a) Map of the southern Sierra Nevada study area, including a representation of the location of the points used for the ecosystem-wide sample, with live tree areas colored green and red stage mortality areas colored purple; a representation of the national forest and park boundaries in pink; and a representation of the approximate location of the Soaproot Saddle focus area (shown in part b) in yellow. The initials represent the land ownership, SNF = Sierra National Forest, STF = Stanislaus National Forest, YNP = Yosemite National Park. b) Map of the Soaproot Saddle focus area, sampled live trees are colored green and dead trees purple. A boundary for the sampling area is shown in pink. For both a) and b) a black and white digital elevation model underlies the maps, the maps are scaled differently for appropriate contrast based on the elevation differences, but in both maps darker areas represent lower elevations. c) Representation of the location of the study area within California.

I also analyze a much narrower focus area called Soaproot Saddle. Soaproot Saddle was established by the SSCZO (Goulden et al. 2012) as a field site and was included as part of the NEON (Kampe et al. 2013). Soaproot Saddle is broadly representative of the vegetation types found elsewhere in the study area. It is used as a focus area because it was imaged with a unique combination of fine-scale airborne imaging spectroscopy and lidar, which allowed for the collection of continuous information on species and stand characteristics (see Chapter 4 for more details).

5.2.2. Overview of Methods

In order maximize the comparability of the broad study area and the Soaproot Saddle focus area, both analyses were made as parallel as possible. For both spatial scales, I first randomly selected conifers that were either alive or red stage in 2016 from a population of trees that were alive in 2015. I then assembled a spatially explicit database of grouped variables that may influence tree mortality. In order to assess and eliminate variables with high amounts of collinearity, the variance of inflation factor (VIF) statistic was used. Finally, using the RF algorithm (Breiman, 2001) and 2016 conifer survival as a response variable, I test how predictive a variety of input features were.

5.2.2.1. Collection of 2016 Live and Red Stage Mortality Data

In order to conduct a random sampling of 2016 live and dead conifers across the wider study area, regions that were classified by an algorithm as being both more than 50% conifer cover and free of conifer overstory mortality in 2015 were identified (see Chapter 3). Within these regions, areas where 1 m resolution multispectral WorldView imagery (http://www.digitalglobe.com) were collected in 2015 and 2016 were used as a sampling area. 30 by 30 m squares were randomly placed within the sampling area and each square was manually evaluated using the WorldView imagery. Squares were used only if they were correctly classified as being primarily green conifers in 2015, and if, in 2016, the areas were either free of mortality or more than 50% red stage mortality. To obtain an even weight between the two classes, samples in the more common class were randomly eliminated. A total of 924 randomly selected samples (462 in each class) were used.

A similar procedure was undertaken in the Soaproot Saddle focus area. Where WorldView imagery was available in 2015 and 2016, individual ponderosa pines trees (using the species classification in Chapter 4) were randomly selected. Trees were then

manually evaluated as to whether they were green in 2015, and if so, whether the trees were visually healthy or red stage in 2016. Random sampling was then used to make the number of trees in each class equal. In total 470 trees (235 in each class) were used.

Areas that, according to a Forest Service database, had been either burnt or thinned mechanically between 2013 and 2016 were not sampled for either dataset.

5.2.2.2. Factors Potentially Controlling Conifer Mortality Evaluated

Variables that could potentially influence tree mortality were collected at both scales. I placed each of these variables into one of five categories: biotic, climatic, contagion (distance from existing areas of red stage mortality), individual, and topographic (Table 5.1). Climatic category variables were obtained from the parameter-elevation relationships on independent slopes model (PRISM, Daly et al. 2008). This model evaluates precipitation and temperature at a 100 X 100 m pixel size. The Soaproot Saddle area was deemed to be too spatially limited for there to be significant precipitation and temperature differences that were not directly linked to topography, so climatic variables were evaluated only at the scale of the entire southern Sierra Nevada. Variables in the topographic category were obtained from processing DEMs in SAGA GIS V 4.0 (http://www.saga-gis.org/en/index.html). For the southern Sierra Nevada, a 10 m DEM was accessed from the USGS database (https://lta.cr.usgs.gov/NED). For Soaproot Saddle, a 1 m DEM was interpolated from the NEON project lidar data. This was done in ENVI 5.2 (Harris Geospatial Solutions) with the BCAL extension (Streutker and Glenn, 2006), using a 13 m window and a natural neighbor algorithm. Contagion information was obtained via manual interpretation of 2015 WorldView images specific to each sample. The distance from the sample to the closest

group of one, three, and ten red stage mortality trees was assessed in discrete 50 m intervals, ranging from an interval of 0-50 m to 400 m or more.

Table 5.1. Base information on the categories and variables used for analysis. In the table, parameter-elevation relationships on independent slopes model is abbreviated as PRISM and digital elevation model is abbreviated as DEM.

Category	Variables	Data Source	Data Source Scale	Evaluation Scale
Ecoregion Evaluation				
Topographic	Aspect, curvature, elevation, slope, solar insolation, topographic wetness index	Topographic maps	10 X 10 m	10 X 10 m
Biotic (vegetation indices)	27 narrow band vegetation indices from six dates	Imaging spectrometry	30 X 30 m	30 X 30 m
Biotic (fire history)	Time since 1st, 2nd, and 3rd fire	Cal Fire fire history database	Vector	vector
Biotic (water Stress)	Progressive water stress, vulnerability score	Asner et al. 2016	30 X 30 m	30 X 30 m
Climatic	Seasonal, yearly, and 3-year, cumulative precipitation and average temperature.	PRISM	100 X 100 m	100 X 100 m
Contagion	Distance from 1, 3, and 10 dead trees	2015 WorldView imagery	1X1 m	Up to 400 m radius circle buffer
Soaproot Saddle Area				
Contagion	Distance from 1, 3, and 10 dead trees	2015 WorldView imagery	1X1 m	Up to 400 m radius circle
Topographic	Aspect, curvature, elevation, slope, solar insolation	lidar based DEM	1 X 1 m	3 X 3 m average
	Topographic wetness index		1 X 1 m	Max of 10 m radius circular buffer
Individual	Crown size, tree height	lidar and imaging spectroscopy	1 X 1 m	1 X 1 m and crown size
	Crown level average vegetation index		1 X 1 m	Crown size
Biotic (canopy structure & species composition)	Lidar based canopy density, kurtosis, max canopy height, min canopy height, various quantiles of canopy height, median/max canopy ratio, rumple index, surface area, skewness, standard deviation of canopy height, percent of the top of the tree crown occupied by: < 10 m tall cover, dead trees, hardwoods, incense-cedar, ponderosa pine, sugar pine, white fir	lidar and imaging spectroscopy	1 X 1 m	10, 20, 30, 45, 60, 100 m radius circular buffer

The Soaproot Saddle focus area was selected to take advantage of the high spatial resolution imaging spectroscopy and lidar remote sensing acquired over the area in June

2013, which allowed for the unique characterization of the canopy. Complete information on the remote sensing data processing workflow with respect to the biotic variables can be found in (Chapter 4), but are briefly summarized here. Lidar data collected as part of the NEON project were used to generate a DCM; the DCM allowed for the identification of a variety of different canopy metrics related to canopy size, density, and variability throughout the Soaproot Saddle area. In order to create spatial representations of tree crown's location and extents, an automated process delineated the DCM into individual tree crown objects. Combined with imaging spectroscopy data, these canopy objects were used to classify individual tree species. The resultant spatial database of tree crown object's extent and species allowed for estimation of the canopy cover surrounding any given tree, classified by species. Both canopy structural metrics and species composition were evaluated within circular buffers of varying sizes around the target trees (Table 5.1). The length of the radii for the buffers tested were 10 m, 20 m, 30 m, 45 m, 60 m, and 100 m.

Interpretation of the DCM allowed for the estimation of target tree height and crown size. I also used imaging spectroscopy based vegetation indices (see Table 5.2 for a complete list) averaged over crown areas to collect information on target trees' structural, biochemical, and stress properties (Roberts et al., 2011).

Table 5.2. The 28 vegetation indices uses in this analysis (modified from Roberts et al. 2011)

Index Name	Acronym	Equation	Source
Anthocyanin Content Index	ACI	R_{550} / R_{860}	Van Den Berg and Perkins 2005
Anthocyanin Reflectance Index	ARI	$(1/R_{550}) - (1/R_{713})$	Gitelson et al. 2001
Cellulose Absorption Index	CAI	$0.5*(R_{2031} + R_{2211}) - R_{2101}$	Daughtry 2001
Chlorophyll Absorption in Reflectance Index	CARI	$[(R_{700} - R_{670}) - 0.2*(R_{700} - R_{550})]$	Kim 1994
Chlorophyll Index Red Edge	$CI_{rededge}$	$R_{860}/R_{713} - 1$	Gitelson et al. 2003
Carotenoid Reflectance Index	CRI1; CRI2	$[(1/R_{510}) - (1/R_{550})]$; $[(1/R_{510}) - (1/R_{700})]$	Gitelson et al. 2002b
Enhanced Vegetation Index	EVI	$2.5 * (R_{860} - R_{650})/ (R_{860} + 6 * R_{650} - 7.5 * R_{470} + 1)$	Huete et al. 2002
Modified Anthocyanin Reflectance Index	mARI	$[(1/R_{550}) - (1/R_{713})] * R_{860}$	Gitelson et al. 2001
Modified Chlorophyll Absorption in Reflectance Index	MCARI	$[(R_{700} - R_{670}) - 0.2*(R_{700} - R_{550})] * (R_{700}/R_{670})$	Daughtry et al. 2000
Moisture Stress Index	MSI	R_{1610}/R_{840}	Rock et al. 1986
Normalized Difference Infrared Index	NDII	$(R_{840} - R_{1610}) / (R_{840} + R_{1610})$	Hardisky et al. 1983
Normalized Difference Lignin Index	NDLI	$[\log(1/R_{1754}) - \log(1/R_{1680})]/ [\log(1/R_{1754}) + \log(1/R_{1680})]$	Serrano et al. 2002
Normalized Difference Nitrogen Index	NDNI	$[\log(1/R_{1510}) - \log(1/R_{1680})]/ [\log(1/R_{1510}) + \log(1/R_{1680})]$	Serrano et al. 2002
Normalized Difference Vegetation Index	NDVI	$(R_{860} - R_{650}) / (R_{860} + R_{650})$	Rouse et al. 1973
Normalized Difference Water Index	NDWI	$(R_{860} - R_{1240}) / (R_{860} + R_{1240})$	Gao 1996
Photochemical Reflectance Index	PRI	$(R_{531} - R_{570}) / (R_{531} + R_{570})$	Gamon et al. 1997
Pigment Sensitive Normalized Difference	PSND	$[(R_{800} - R_{675}) / (R_{800} + R_{675})]$	Blackburn 1998
Plant Senescence Reflectance Index	PSRI	$(R_{678} - R_{500})/R_{750}$	Merzlyak et al. 1999
Pigment Specific Spectral Ratio	PSSR	(R_{800} / R_{675})	Blackburn 1998
Red Green Ratio Index	RGRI	R_{650} / R_{550}	Gamon and Surfus 1999
Red Edge Vegetation Stress Index	RVSI	$(R_{714} + R_{752})/2 - R_{733}$	Merton and Huntington 1999
Structure Insensitive Pigment Index	SIPI	$(R_{800} - R_{445})/(R_{800} - R_{680})$	Penuelas et al. 1995
Simple Ratio	SR	R_{860} / R_{650}	Jordan 1969
Visible Atmospherically Resistant Index	VARI	$(R_{550} - R_{650})/(R_{550} + R_{650} - R_{470})$	Gitelson et al. 2002a
Vegetation Index using Green Band	VI_{green}	$(R_{550} - R_{650})/(R_{550} + R_{650})$	Gitelson et al. 2002a
Water Band Index	WBI	R_{900} / R_{970}	Penuelas et al. 1997

For the larger study area, the HyspIRI Preparatory Airborne Campaign represented a unique and potentially powerful data source. The HyspIRI campaign involved flying AVIRIS seasonally for multiple years across the study area starting in 2013 (Thompson et al., 2015). Using these data and the vegetation indices presented in Table 5.2, the structural and stress properties of vegetation were assessed at a 30 X 30 m pixel size for six time points: 3 May 2013 (spring 2013), 12 July 2013 (summer 2013), 3 July 2014 (summer 2014), 6 October 2014 (fall 2014), 5 May 2015 (spring 2015), and July 3 2015 (summer 2015). The time since the last fire, second to last fire, and third to last fire, provided a means of partially assessing disturbance history over a wide area. I obtained this information from a CAL FIRE fire perimeter history database, which includes fires dating back to the 1920's (http://frap.fire.ca.gov/data/frapgisdata-sw-fireperimeters_download). For each sample point, the time since fire was recorded at discrete 10-year intervals. Finally, the PWS of a 30 X 30 m resolution pixel from 2013 to 2015 and the vulnerability score as assessed in Asner et al. (2016) was also assessed at each point.

5.2.3. Data Pre-Processing

5.2.3.1. No Data Values

After processing the fire perimeter data, it was found most of the study area had only burnt in a maximum of a single fire since 1920, meaning the time since second and third to last fire consisted almost entirely of no data values. Those variables were therefore removed from further analysis. Some spectral indices had occasional no data or infinite values. Since these rare cases would be problematic in further processing steps, they were assigned a value of 0.

5.2.3. Elimination of Collinearity among Variables

In a variety of statistical analysis contexts, collinearity is a major challenge to determining which and to what degrees various covariates impact a response variable (Zuur et al., 2010). Using RF to assess feature importance has been found to be no exception (Millard and Richardson, 2015). The VIF statistic is a commonly used index for assessing collinearity among covariates. Often when using the VIF statistic, a maximum threshold VIF value is selected, and covariates are eliminated until all remaining predictors are below that threshold value. Possible threshold values often used include two, three, and five (Zuur et al., 2010). Most or all individual variables analyzed in this study likely have a fairly weak ability to distinguish where mortality is occurring; therefore, a low VIF value of two was selected for the VIF threshold.

In order to accomplish this, within each category, the variable with the highest VIF statistic was iteratively eliminated until only variables with VIF values below two were remaining. This process will reduce collinearity, however, variables eliminated in this process may be important causal variables in predicting the response variable. For the climatic variables, all possible combinations of the temporally divided variables for both precipitation and temperature had VIF statistics above two. Therefore, only the most temporally inclusive variables, the average temperature and cumulative precipitation between 2013 and 2015, were used.

In various renditions of the RF analysis, data were analyzed both at the individual category level (as defined in Table 5.1) and as a whole. When data were aggregated for analysis as a whole, the variables in each category that were not previously eliminated through VIF were combined. VIF was again assessed, this time variables were eliminated based on both removing variables with a high VIF statistic and targeting categories

containing more variables. A complete list of the variables used and eliminated for each dataset is available in Appendix 6.

5.2.4. Assessment of Category and Variable Importance

In order to assess the importance of predictor variables for determining 2016 tree status, I used the RF machine learning algorithm (Breiman, 2001), as implemented in R version 3.2.2 (R Core Team) through the *randomForest* package (Liaw and Wiener, 2002). RF is an ensemble machine learning technique, wherein a user-determined number of individual CT are given by sampling with replacement from training data. In addition, a user-determined subset of the total training variables is given to each individual split in each CT. In this study, for each individual implementation of RF, 500 trees were generated and the subset of variables given to each individual split was the square root of the total number of variables in the RF (a number variable for each RF implementation). Both of these parameters are commonly used and have been found to yield acceptable results in previous studies (Belgiu and Dragut, 2016).

RF does not make parametric assumptions about the distribution of input variables, RF can deal with both categorical and continuous variables, the accuracy of the RF algorithm is comparable to other advanced machine learning algorithms, and RF has previously been demonstrated to perform well in high dimensional feature spaces (Belgiu and Dragut, 2016; Breiman, 2001; Fernández-Delgado et al., 2014). A means of independent accuracy evaluation is also inherently created in the RF classification process. Only a subset of the training data, equal to approximately 1-1/e, are used for any given CT. The data not used, known as OOB, can be employed as an independent validation to assess the overall accuracy of the RF algorithm (Breiman, 2001). Metrics taking advantage of the fact that only a subset

of variables are used in any given split, such as the mean decrease in accuracy (MDA) score, have been developed to estimate the importance of a single variable to the overall classification accuracy. MDA has been found to be an effective means for evaluating how relatively influential multiple ecological variables are for an outcome (Cutler et al., 2007). Although the precise MDA number for each individual RF run may vary considerably, as long as variables are fairly uncorrelated the order of the scores is generally consistent (Millard and Richardson, 2015). I also used the OOB accuracy to evaluate the ability of various categories to predict 2016 status. At both spatial scales, each individual variable category was run against the response variable of the 2016 live or red stage status. For the Soaproot Saddle area, data from the various spatial buffer sizes used to evaluate canopy structure and species composition were highly correlated. Therefore, whether there was a single optimal buffer size was also tested. A combined dataset of all of the buffers was also run against the response variable. Finally, I tested the impact on accuracy of iteratively removing each single category from the combined dataset of predictive variables. Since any given RF run's OOB and MDA score is inherently stochastic, I ran RF 100 times to determine the mean and variation of these statistics.

5.3. Results

5.3.1. Assessment of Feature Sets

5.3.1.1. Assessment of Feature Sets - Soaproot Saddle Dataset

For Soaproot Saddle, I assessed the accuracy each variable category (as defined in Table 5.1) had in predicting an individual tree's 2016 status. Categories differed in their predictive power from low (53.5% average OOB accuracy for the individual tree variable category) to moderately high (65.9% average OOB accuracy for canopy variables assessed at a 45 m

radius buffer size; Table 5.3). For the canopy category, I found a buffer size of 45 m most accurately predicted tree mortality, even compared to combining all six buffer sizes together. Canopy variables assessed at 10 m and 20 m buffer distances, encompassing just the target tree and its immediate neighbors, were less predictive of 2016 tree mortality than canopy variables assessed at larger distances.

I also analyzed the impact of iteratively removing each category from a combined dataset. Only canopy variables assessed at the 45 m buffer size were included in the combined model, because of the superior prediction accuracy achieved at that distance. Removing canopy variables from the combined dataset decreased the OOB accuracy the most, suggesting a relatively high importance not replicated by other categories. The combined dataset only had a slightly higher accuracy than the canopy category alone (OOB accuracy 67.1% versus 66.5%), which further demonstrates the unique data contained in the canopy category. Contagion variables, which record the distance from groups of 2015 red stage trees, had the second highest OOB accuracy, and also created the second greatest decrease in OOB accuracy when removed from the combined dataset. In contrast, variables in the individual tree attributes category were the least predictive and created the smallest drop in accuracy.

Table 5.3. The mean accuracy of 100 runs of the random forest algorithm's prediction of 2016 live and red-stage mortality trees in the Soaproot Saddle area based on various categories of data. Out of bag is abbreviated to OOB. "All – C45" indicates a combination of canopy variables assessed at a 45 m buffer size, topographic, contagion, and individual tree variables.

Category	Mean OOB accuracy (standard deviation)	Number of variables
Biotic - canopy – 10 m	56.6% (0.9%)	8
Biotic - canopy – 20 m	60.5% (0.9%)	9
Biotic - canopy – 30 m	63.0% (0.8%)	8
Biotic - canopy – 45 m	65.9% (1.0%)	8
Biotic - canopy – 60 m	58.9% (1.1%)	8
Biotic - canopy – 100 m	63.9% (1.2%)	9
Biotic - canopy – all scales	62.4% (1.0%)	22
Contagion	59.3% (0.8%)	1
Individual tree	53.5% (1.1%)	6
Topographic	57.3% (1.0%)	5
All	66.5% (1.0%)	33
All - C45m	67.1% (1.0%)	20
All – C45 without canopy	61.0% (1.1%)	12
All – C45 without contagion	63.7% (1.1%)	19
All – C45 without individual tree	66.7% (0.9%)	14
All – C45 without topographic	65.7% (0.9%)	15

5.3.1.2. Assessment of Feature Sets - Southern Sierra Nevada Dataset

Similar analysis of each individual category's predictive power of 2016 status was done across the southern Sierra Nevada (Table 5.4). The climatic and contagion categories had the two highest accuracies when used alone. When all variables were combined and then each category was iteratively removed, the climatic and contagion categories also had the largest decreases in accuracy. In contrast, topographic and biotic variables, which were associated with stand density, structure, and stress, appeared less important. The combined dataset performed better than any individual category. Most of this improvement appears to be from the combination of the climatic and contagion categories, as removing any other category had little impact on accuracy.

Overall, the average accuracy achieved from the combination of the landscape level, spatially coarse variables for predicting mortality across the southern Sierra Nevada (71.3%)

was moderately higher than the accuracy achieved in using the combination of fine-scale, canopy level variables for predicting single-tree mortality in a single watershed (67.1%).

Table 5.4. The accuracy of 100 runs of the random forest algorithm's prediction of 2016 live and red-stage mortality areas across the southern Sierra Nevada based on various categories of variables. Out of bag accuracy is abbreviated to OOB accuracy, vegetation indices are abbreviated to VIs, progressive water stress is abbreviated as PWS.

Category	Mean OOB accuracy (standard deviation)	Number of variables
Biotic – fire	55.0% (0.3%)	1
Biotic – PWS	54.6% (0.8%)	2
Biotic – VIs	61.5% (0.1%)	11
Climatic	67.3% (0.3%)	2
Contagion	67.6% (0.2%)	3
Topographic	56.6% (0.1%)	3
All	71.1% (0.6%)	18
All without fire	70.8% (0.6%)	17
All without PWS	70.6% (0.6%)	16
All without VIs	71.3% (0.6%)	10
All without climatic	68.1% (0.6%)	16
All without contagion	68.9% (0.7%)	16
All without topographic	70.1% (0.5%)	15

5.3.2. Assessment of Individual Variables

5.3.2.1. Assessment of Individual Variables - Soaproot Saddle Dataset

I also examined the individual MDA scores of all the variables used in the combined dataset (which included variables from the canopy category assessed at a 45 m buffer size, as well as the topographic, contagion, and individual tree categories) for Soaproot Saddle (Table 5.5). The lidar-based measurement of vertical canopy kurtosis over a 45 m buffer had the highest MDA score of all variables analyzed. Kurtosis is a measurement of the peakedness and tailedness of a distribution. For lidar applied to forestry, vertical tree heights with low kurtosis values (platykurtic distributions) are indicative of leaves being well distributed throughout the vertical canopy profile of trees. Stands that may exhibit these attributes include multilayered, multigenerational stands. High vertical canopy kurtosis

(leptokurtic distributions) could be indicative of a single-layered canopy with few leaves in the canopy understory, such as might be found during the stem exclusion phase of stands. Areas that were primarily openings, with scattered large trees, would also have relatively high canopy kurtosis values (although lower than a single-layer canopy).

The distribution of canopy kurtosis values and four other variables with the highest MDA scores (distance from 10 dead trees, elevation, percent incense-cedar cover over a 45 m area, and maximum height within a 45 m area) for trees that were alive or dead in 2015 were compared (Figure 5.2). From this comparison it is clear that trees that are surrounded by canopies which are more leptokurtic, further from a group of 10 or more dead trees in 2015, at higher elevations, are surrounded by more incense-cedar cover within 45 m, and have a higher tallest tree within 45 m were more likely to survive between 2015 and 2016. A visualization of the top four variables by MDA score within the Soaproot Saddle focus area demonstrates each variable has spatially distinctive patterns and distribution (Figure 5.3).

Table 5.5. Each of the variables included in the combined topographic, contagion, individual tree, and canopy assessed at a 45 m buffer size categories for Soaproot Saddle and all the variables combined for the southern Sierra Nevada. Variables are listed in descending order of importance as evaluated by the mean decrease in accuracy (MDA) score.

Soaproot Saddle area			Southern Sierra Nevada		
Variable	Category	MDA	Variable	Category	MDA
Canopy kurtosis over 45 m buffer	Local biotic	0.0159	Cumulative Precipitation 2013 - 2015	Climatic	0.0359
Distance from 10 dead trees in 2015	Contagion	0.0114	Average Temperature 2013- 2015	Climatic	0.0311
Elevation	Topographic	0.0087	Distance from 10 dead trees in 2015	Contagion	0.0262
Percent of incense-cedar cover over 45 m buffer	Local biotic	0.0059	TWI	Topographic	0.0112
Maximum height over 45 m buffer	Local biotic	0.0050	Distance from 1 dead tree in 2015	Contagion	0.0071
Target tree NDWI	Individual tree	0.0042	Summer 2015 EVI	Local biotic	0.0047
Target tree ARI	Individual tree	0.0033	Elevation	Topographic	0.0046
TWI	Topographic	0.0030	Summer 2013 RVSI	Local biotic	0.0043
Aspect	Topographic	0.0024	Summer 2014 CRI1	Local biotic	0.0042
Mean 5th percentile Canopy height over 45 m buffer	Local biotic	0.0023	PWS	Local biotic	0.0039
Solar insolation	Topographic	0.0022	Summer 2014 CAI	Local biotic	0.0030
Target tree WBI	Individual tree	0.0018	Summer 2014 CRI1	Local biotic	0.0029
Minimum canopy height over 45 m buffer	Local biotic	0.0014	Time since last fire	Local biotic	0.0016
Percent dead tree cover over 45 m buffer	Local biotic	0.0014	Fall 2014 CRI1	Local biotic	0.0016
Slope	Topographic	0.0012	Aspect	Topographic	0.0015
Crown size	Individual tree	0.0002	Summer 2013 CAI	Local biotic	0.0012
Percent white fir cover over 45 m buffer	Local biotic	-0.0001	Spring 2013 CAI	Local biotic	0.0011
Percent hardwood cover over 45 m buffer	Local biotic	-0.0007	Vulnerability score	Local biotic	0.0001
Target tree EVI	Individual tree	-0.0011			
Target tree SIPI	Individual tree	-0.0017			

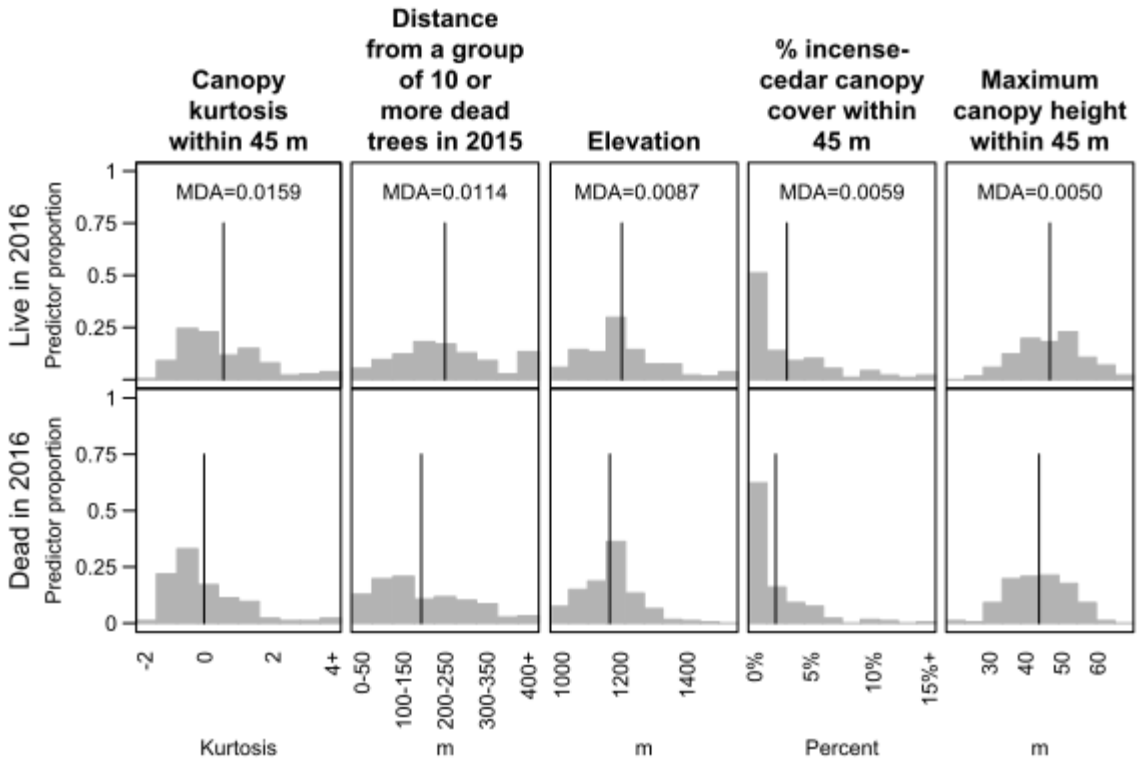

Figure 5.2. Histograms for both live and red stage mortality trees of the five most important variables, as judged by the mean decrease in accuracy (MDA), for the dataset which combined variables related to canopy assessed at a 45 m distance, topographic, contagion, and the individual trees for Soaproot Saddle. The black line represents the distribution mean. For canopy kurtosis and percent incense-cedar cover, outliers were truncated for display purposes.

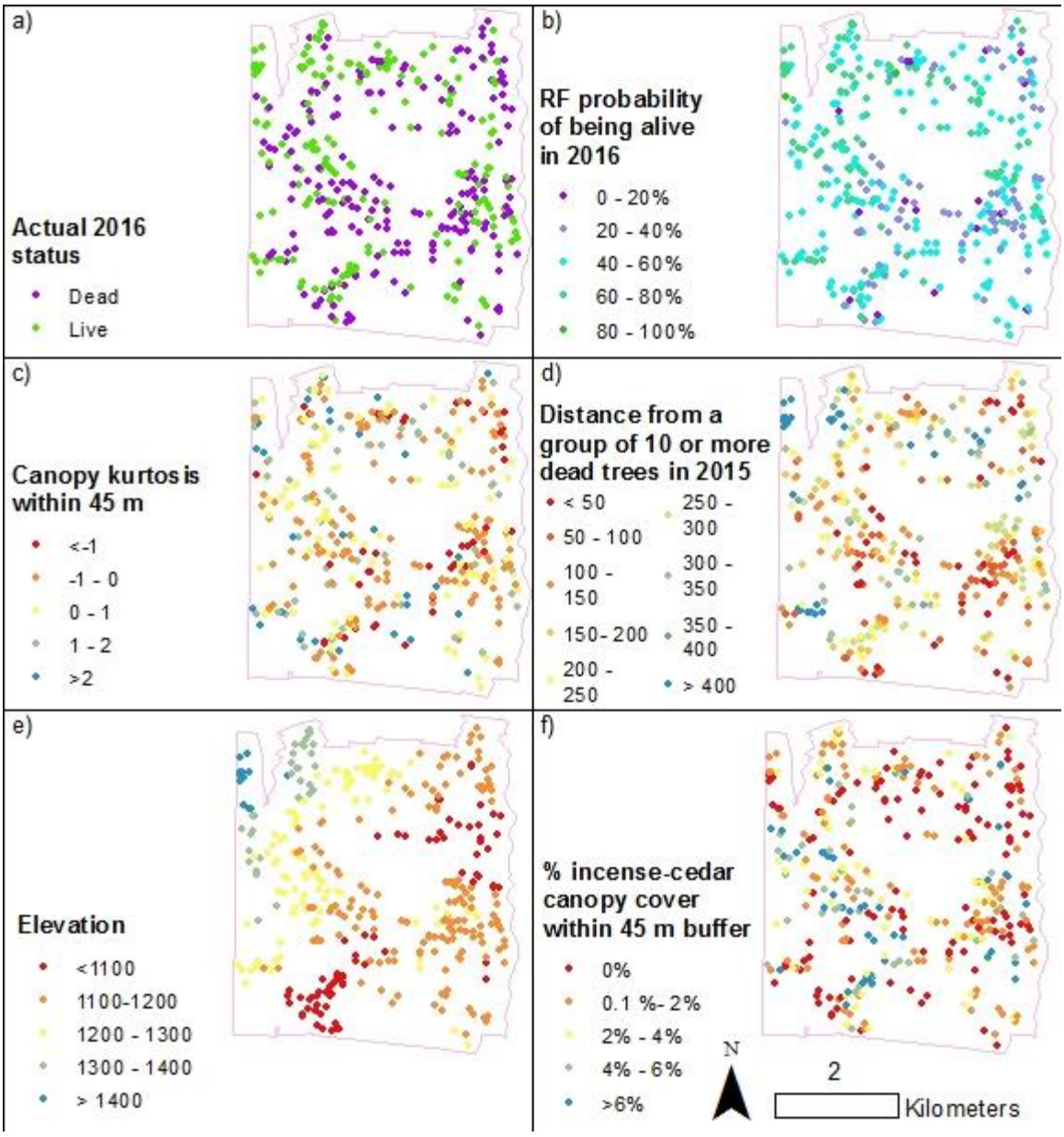

Figure 5.3. Among the sample trees, the spatial distribution of: a) live and dead trees, b) the percent of times a sample tree was classified as being alive by the 500 decision trees used by a random forest classification, c) canopy kurtosis, d) the distance from a group of 10 or more dead trees in 2015, e) elevation, and f) percent incense-cedar canopy cover. An outline of the sampling area is shown in pink.

5.3.2.2. Assessment of Individual Variables - Southern Sierra Nevada Dataset

A similar analysis of MDA scores was performed for the entire southern Sierra Nevada area for the variables that were included in the all categories dataset (Table 5.5). The two variables with the highest MDA scores were the only two climatic variables used in the analysis, the cumulative precipitation and average temperature between 2013 – 2015. Two contagion variables, distance from a group of ten dead trees in 2015 and one dead tree in 2015, had the third and fifth highest MDA scores, respectively. TWI and summer 2015 Enhanced Vegetation Index (EVI) were the variables with the fourth and sixth highest MDA scores, respectively. Histograms of the top six variables for live and dead tree areas (omitting the distance from one dead tree in 2015, which had a distribution very similar to ten dead trees) are shown (Figure 5.4). Based on a comparison between live and dead trees, live trees in 2016 tended to receive higher precipitation and experience lower temperatures between 2013 – 2015, were further from dead trees in 2015, were located in areas with a higher TWI, and had lower EVI values.

The spatial patterns of the top four variables by MDA score were also analyzed (Figure 5.5). Due to the spatial resolution of the PRISM data and the nature of climate, there is little fine-scale spatial variation of precipitation and temperature. The southern part of my study area, where 2015 mortality appears most prevalent, also received the smallest amount of cumulative precipitation between 2013 and 2015, whereas temperature shows a less pronounced latitudinal gradient. While not as uniform as precipitation, distance from 2015 mortality also shows a moderately high latitudinal gradient, with generally more mortality in the southern part of my study area.

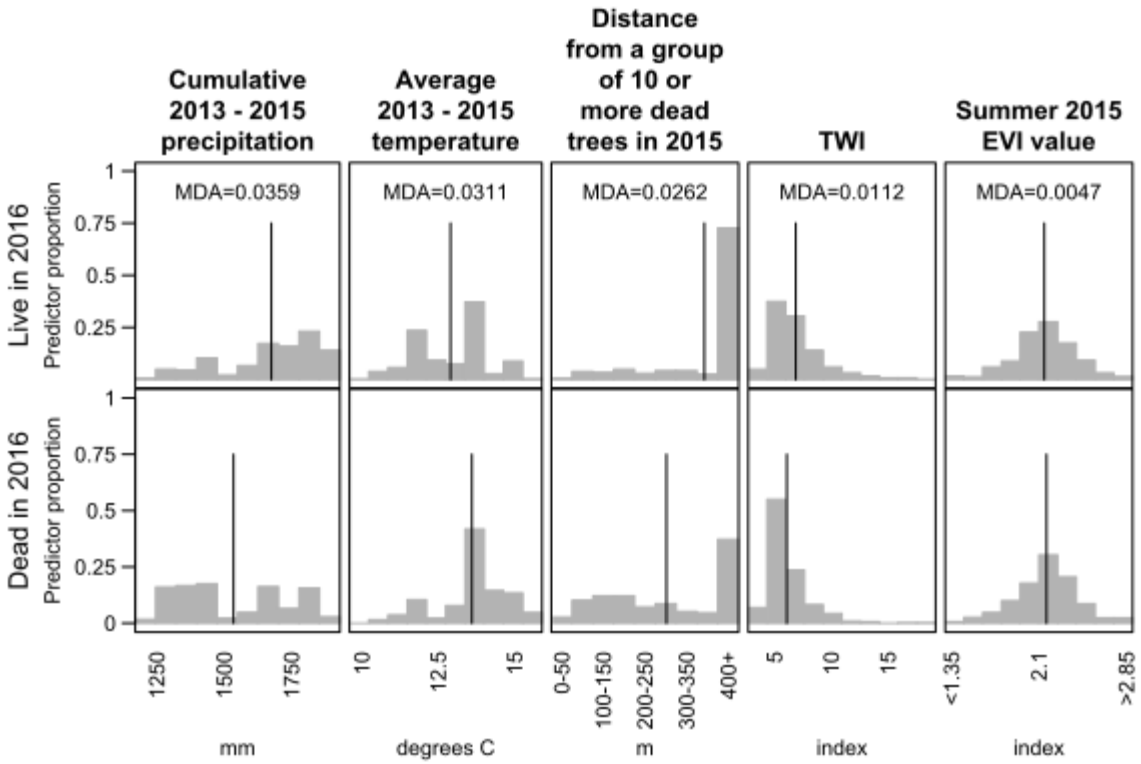

Figure 5.4. Histograms of the five of the six most important variables, as judged by the mean decrease in accuracy (MDA), for the all categories combined feature set for the southern Sierra Nevada for areas that were predominately live and red stage mortality trees. The black line represents the distribution mean. For summer 2015 enhanced vegetation index (EVI), outliers were truncated for display purposes.

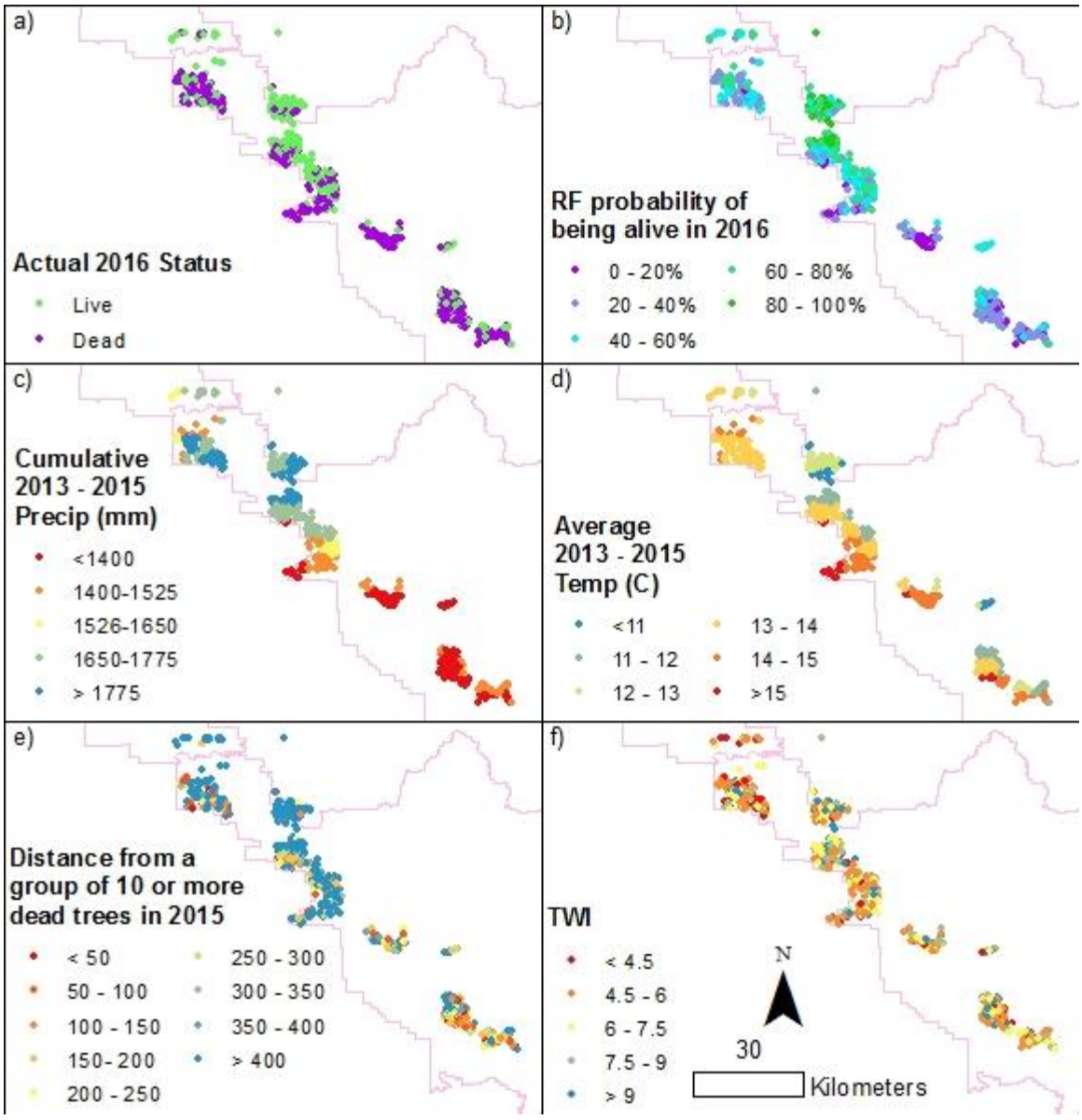

Figure 5.5. Among the sample areas, the spatial distribution of: a) live and dead trees, b) the percent of times a sample tree was classified as being alive by the 500 decision trees used by a random forest classification, c) cumulative 2013-2015 precipitation, d) average 2013-2015 temperature, e) the distance from a group of 10 or more dead trees in 2015, and f) the topographic wetness index (TWI). National Forest and National Park boundaries are shown in pink.

5.4. Discussion

5.4.1 Sources of Error and Uncertainty in the Analysis

In this exploratory analysis, I used a variety of primarily remote sensing based data sources to investigate relationships with tree mortality. However, not all relevant factors can be collected remotely, and many of the factors that can be collected are estimates that have inherent errors within them. Previous work has found mortality in the 2012 – 2016 Sierra Nevada drought to be highly influenced by species, with pines having much higher mortality than other conifers (Paz-Kagan et al. 2017, Chapter 4 of this dissertation). In the Soaproot Saddle focus area, I used an existing species classification to isolate those trees that were likely ponderosa pine. However, species classification error is a source of potential bias that I could not easily control for. At the broader southern Sierra Nevada scale, species was even more difficult to control for. I limited my analysis to coniferous forests and elevational ranges where ponderosa pine was likely to be dominant. However, other species of conifer were likely present in the area.

At the Soaproot Saddle scale, the response variable used the status of an individual tree in 2016. By contrast, in the southern Sierra Nevada it was status of groups of trees within a 30 x 30 m area. Because of the differing response variables, cross-scale comparisons should be undertaken with some caution, although Chapter 4 of the dissertation) found 2016 mortality within Soaproot Saddle to generally occur in large groups.

Remote sensing is also not a perfect tool for collecting all the categories of information. For example, at the individual tree level, several factors that are likely to impact a tree's survival, such as the tree's genetics, bole diameter, and the presence of pathogens on the tree, were not possible to measure with remote sensing. I cannot conclude that because the

individual tree category was found in this analysis to be not important, if additional individual tree information was collected through other means it would also not be predictive of tree mortality.

The variables found to be highly correlated with mortality in this analysis may not be the actual causal variable. VIF is not a test of causality, and the variables found to be important in the RF analysis could only be correlated with the true causal variables (Zuur et al. 2010). The variables kept in the VIF process were simply effective at summarizing all of the data without collinearity. For example, this analysis is equivocal as to whether canopy kurtosis is the actual causal variable of tree survival or if other highly correlated variables was the actual causal variable. I therefore examine the correlation with variables used in the analysis with eliminated variables in order to give greater context to my analysis.

5.4.2 Important Variables at the Local Scale

For Soaproot Saddle, measures of canopy structure and species composition were, among the variables assessed, highly important in predicting 2016 tree status. However, the size of the analysis area was highly important. Evaluations performed over 10 or 20 m radius area around a target tree did not yield a model that was nearly as predictive of mortality as 45 m. If a tree's 2016 survival was heavily impacted by limited growing space due to light, water, or other forms of competition, then I would expect canopy structure at 10 m to be more predictive of tree mortality. For example, Das et al. (2011) used a 9 m buffer to evaluate the impact of local tree competition. Canopy structure and species composition over larger analysis areas, such as 45 m, are more indicative of the microsite the tree is growing in than competition limited growing space. One possible explanation for a microsite's importance for tree survival is direct interaction between the microsite and the

tree. A tree's ability to resist mortality may be directly tied to higher local site index or the local historic disturbance regime. Another possibility is that the microsite is indirectly impacting tree mortality by influencing bark beetles. Microsite conditions have previously been found to influence bark beetle dynamics in several ways. Higher temperatures and greater wind speeds in the understory of recently thinned stands have been found to negatively impact bark beetle's ability to overwinter, as well as disrupt pheromone signals used in the initial phase of bark beetle attack (Fettig et al., 2007).

To provide further physical meaning to canopy kurtosis within my study area, I evaluated the correlation of kurtosis with other variables that were eliminated in the VIF analysis (likely in large part due to correlation with kurtosis). Kurtosis was highly positively correlated (coefficient of determination (r^2) of 0.89) with vertical canopy skewedness; a positive value for canopy skewedness indicates canopy distributions that are mostly near the ground with some outlying taller trees. Within a 45 m analysis area, kurtosis was also positively correlated ($r^2 = 0.57$) with percentage area below 10 m canopy height. The high importance in my model of vertical canopy kurtosis evaluated over a 45 m radius around a target tree (Table 5.5 and Figure 5.2) seems to be in line with previous findings. High kurtosis values are associated with conditions similar to recently thinned stands: non-continuous canopies that contain gaps and open understories.

Ponderosa pine survival may also be influenced by canopy-level trees' species diversity. Over a 45 m range around the target tree, the percentage cover of incense-cedar, the second most common conifer in Soaproot Saddle, was positively predictive of tree survival. More species and age heterogeneity within a stand has been found to provide less continuous food sources for bark beetle and more drought resilience (Clark et al., 2016; Fettig et al., 2007).

Positive kurtosis values were also correlated with less ponderosa pine cover over a 45 m area (r^2 = -0.60), so the strength of kurtosis in predicting survival provides further evidence for species diversity's importance. Given the strong relationship between maximum height and the vertical standard deviation of the canopy (r^2 = 0.82), which was eliminated in VIF process, higher maximum height may also be acting as a proxy for greater tree height diversity. Interestingly, hardwoods are also common within Soaproot Saddle, however, the percentage cover of hardwood canopy showed no predictive power for target ponderosa pine mortality.

Another possible factor which could be playing a role in tree survival is local soil depth and site conditions. In the southern Sierra Nevada, incense-cedar prefers deeper soils (Meyer et al., 2007), so incense-cedar cover may also be a proxy for favorable soil conditions and higher site quality. In areas with the same disturbance regime, height of the tallest trees is largely determined by site quality (Oliver and Larson, 1990). Taller maximum height of any tree within 45 m area was also predictive of survival, which further suggests the importance of site quality. Since hardwoods are often associated with poorer site quality this may also explain why increased hardwood cover around a target tree was not predictive of survival.

Trees closer to a group of ten or more dead trees in 2015 were more likely to be dead in 2016. This suggests the load of bark beetles within a tree's local vicinity was important. Spatial adjacency of bark beetle attack to previous years' mortality has been observed in other areas (Nelson et al., 2007) Alternatively, site and environmental factors that encouraged mortality in 2015 could also have encouraged mortality in 2016. However, only removing contagion variables from the combined dataset reduced the accuracy of the

analysis substantially (Table 5.3). This somewhat discounts the confounding factor of local stand conditions, at least relating to the variables assessed in Soaproot Saddle.

5.4.3 Important Variables at the Ecoregion Scale and Cross-Scale Comparison

Young et al. (2017) used aerial survey data of tree mortality to conclude that areas across the southern Sierra Nevada where mortality was highest were hotter and drier, overcoming any local climatic adaptions. The importance of 2013 - 2015 cumulative precipitation and mean temperature in predicting areas of 2016 tree mortality in my study agrees with this finding (Table 5.4). At the scale of analysis of the southern Sierra Nevada, biotic variables were not generally strong predictors of mortality. Removal of the vegetation indices in the combined category dataset had essentially no impact on the prediction OOB accuracy. In contrast, Young et al. (2017), using plot data interpolated with other remote sensing data sources, found tree density to negatively impact tree survival. I also found at the Soaproot Saddle scale that biotic variables, including open understories, tree height heterogeneity, and species diversity, were important factors in tree survival. These findings all indicate the scale and precision of assessments of biotic condition is highly important. Vegetation indices generated from medium-resolution satellite imagery (which the AVIRIS data is simulated to equivalent to) do not appear to effectively characterize biotic condition without additional input from more fine resolution datasets, such as field measurements.

That topographic aspect was not one of the more important predictors of tree mortality at either scale runs counter to several previous studies of tree mortality in the Sierra Nevada (Guarín and Taylor, 2005; Van Gunst et al., 2016). Paz-Kagan et al. (2017) studying the drivers of 2015 tree mortality in an area south of my study area found aspect to be a moderately important driver of mortality. Factors that are important in some climatic

conditions may not be important or have the opposite effect in others (Van Gunst et al., 2016). Topography has been observed to decrease in importance in predicting attack after bark beetles have become established (Nelson et al., 2007). The conditions in 2016 were also the culmination of several previous years of drought that were without historical precedent (Robeson, 2015). Conifer mortality and water stress were already quite severe in 2015 (Asner et al., 2016; Paz-Kagan et al., 2017a; Young et al., 2017). It is likely that many of the most sensitive trees to drought mortality died in previous years and were therefore excluded from analysis in this study.

Overall both models only have moderate success for predicting tree mortality. Baguskas et al. (2014) obtained an OOB accuracy value of 0.78 using similar methods to predict coastal pine mortality. The lower accuracies in my study are likely due to a combination of factors including other possible explanatory variables, which I was not able to include in the analysis; confounding influences, such as varying conifer species, on mortality predictions; and the inherent stochasticity in the movement of the bark beetles that are driving much of the mortality.

5.4.4 Management Implications

In areas where water stress is highest, changes in precipitation, temperature, and the strength of acute drought in the Sierra Nevada may be shifting climatic conditions away from ponderosa pine's requirements (Mcintyre et al., 2015; Young et al., 2017). The 2013-2015 drought, although extreme, is in line with predictions for California to experience more drought accompanied with above average temperatures in the next 50-100 years (AghaKouchak et al., 2014; Williams et al., 2015). Attempting to perpetuate pine at the lower end of its elevation range may not succeed regardless of the management action

undertaken. With limited resources, land managers should focus on cooler and wetter sites. My findings suggest management activities meant to mitigate tree mortality due to drought should concentrate on stand structures that encourage multiple size classes of trees, including openings, and diverse species assemblages over wide areas. This is in agreement with prior recommendations for management in response to increasing drought (Clark et al., 2016; Millar and Stephenson, 2015). Focusing treatments on areas surrounding tree stands that have recently succumbed to mortality has effectively deterred tree mortality in other parts of North America (Nelson et al., 2007), given the strength of the contagion effect observed here, the effectiveness of similar mitigation activities should be further investigated in the Sierra Nevada.

5.5. Conclusions

Remote sensing at two separate spatial scales allowed us to investigate possible explanatory variables behind tree mortality in the Sierra Nevada during extreme drought and high levels of bark beetle activity. Across the southern Sierra Nevada, I found variables related to climate to be a powerful predictors of tree mortality. In a smaller focus area, I found canopies that were more homogenous and have less species diversity to be more heavily impacted by mortality. Methods used to measure canopy structure available at the broad spatial scale were less predictive of tree mortality than the more spatially, biologically, and structurally detailed methods available at the finer spatial scale. Canopy structure measured at scales that take into account only local competition (10 m) was less predictive of tree mortality than canopy structure measured at scales that are associated with microsite (45 m). Trees closer to the previous year's mortality were more likely to die in the next year. Overall, I found exogenous factors such as climate and bark beetle population

movements to be highly influential on tree mortality. However, some endogenous factors, such as a stand's structure and species composition also impacted tree survival, likely via the ability to influence bark beetle's infection dynamics.

Chapter 6: Conclusions

6.1 Objectives

The objectives identified in the introductory section of this dissertation were achieved. These objectives were:

1) *To test the ability of imaging spectroscopy to measure fire severity through SMA. To evaluate potential workflows for their accuracy and ability to be implemented on a global scale.*

Although Chapter 2 only examines a single fire, MESMA's ability to identify fire severity does show promise. The GV signal was consistently comparable to the WorldView-2 GV fractions. In areas categorized by GeoCBI plots as burned at medium severity, there was generally a strong NPV signal. In areas that burned in high severity, there was a strong ash signal. Implementation of MESMA and interpretation of unmixed pixels is not as straightforward as NBR based approaches. However, the benefits of a measure of fire severity that is objective may comparable globally merits further consideration.

Workflows that used a reduced amount of spectral information and smaller libraries did not appear to have significantly worse accuracies over more information intensive workflows. Although computing power continues to increase, the processing times to implement MESMA with larger spectral libraries and the full suite of spectral information are not trivial. If cover fractions are to be considered as a tool for mapping fire severity globally, a workflow that is computational efficient must be implemented. The combination

of uSZU and In-Cob appeared to be a particularly computation efficient and accurate means of implementing MESMA for determining fire severity.

2) *To simulate spaceborne imaging spectroscopy and Landsat-8 images across the southern Sierra Nevada and compare each platform's ability to detect red stage tree mortality. To also, examine whether imaging spectroscopy can more effectively leverage seasonal and annual data than Landsat-8 images.*

The southern Sierra Nevada and the airborne data that underlies Chapter 3 poses some unique challenge for red stage mortality identification. The use of airborne flight lines meant that sun-sensor geometry varied a great deal between scenes. The southern Sierra Nevada is quite variable among vegetation types with a mix of hardwoods, shrublands, and conifer-dominated areas. Even among the conifers, there is some variability as to the dominant tree cover. In 2015, mortality was also often patchily distributed in areas that were often under 30 by 30 m. Under these conditions, I found imaging spectroscopy to perform more accurately than Landsat simulated imagery (overall accuracy of 85.1% for the best performing imaging spectroscopy compared to 80.2% for multispectral imagery). Although this difference between imaging spectroscopy and Landsat simulated imagery was only 4.9%, and it is likely that under conditions with less complexity the difference would have been smaller, this does demonstrate another area where a spaceborne imaging spectrometer would offer superior performance to existing assets.

Multi-date imagery consistently outperformed single-date imagery with the selected methods for both imaging spectroscopy and Landsat simulated data. However, the different

spectral resolutions did not use the images identically. Compared to single-date imagery, the Landsat simulated imagery appeared to gain similar accuracy from including both annual images from each summer (summer 2013, summer 2014, and summer 2015) and seasonal images from late drought (fall 2014, spring 2015, and summer 2015). In contrast, for the imaging spectroscopy data, the difference between the single-date dataset and the multi-date dataset that only included annual summer images was minimal. The inclusion of the late drought data, however, significantly improved accuracy. When a spaceborne imaging spectrometer is launched, given its increased sensitivity to spectral changes in plants, temporal combinations which did not improve classification for Landsat images should be reconsidered.

3) *To identify conifer areas that were green and conifer areas that were dominated by red stage mortality across the southern Sierra Nevada in 2015.*

The classification created in Chapter 3 showed a tendency to model too much mortality. It was particularly sensitive to areas that had sparse conifer cover. Likely the senescence of the ground cover due to the drought provided a spectral signal similar to a pixel with dense tree cover and partial mortality. Still, as Figure 3.6 demonstrates, the objective was accomplished. Field validation would likely be required if land managers were to use this map for decision-making purposes. However, the accuracy was high enough to be highly useful in sampling live and dead tree areas in 2016 for the purposes of objective #5.

4) *Using the high-resolution remote sensing available in the Soaproot Saddle area, to identify canopy level trees by species and size class pre-drought and identify the impact of the drought by species and size class in 2016.*

I find the methods of Chapter 4 to yield generally acceptable accuracies for identifying the pre-drought canopy level trees. Using the lidar created DCM, the tree delineation algorithm had an OCA of 1.093 (indicating for every 1,000 trees identified 93 were missed) for making canopy objects. I was able to use the high-resolution imaging spectroscopy and canopy objects to classify species at an overall accuracy of 86%. WorldView data allowed for the determination of most tree's 2016 status. These data sources combined, allowed for a map of both the pre-drought crown level species and the post-drought impact (Figure 4.5).

However, to create the most accurate estimates of the numerical impact of the drought on the Soaproot Saddle area, the error in the various model sources must be accounted for. To this end, a Monte Carlo simulation was used. The results of this simulation show ponderosa pine to be by far the most impacted species, with a 17.6% survival rate (Figure 4.6). The overall effect of the drought was to reduce the number of live tree stems from approximately 77,067 to 19,451 between 2013 and 2016. In the Soaproot Saddle watershed, the mortality due to drought was a disturbance with enormous ecological implications. Without further perturbations and assuming there is an ample seed and sapling stock, replenishing the number of large trees before drought will take decades to centuries. However, given model projections for global climate trends, further disturbance in the form of fire or more extreme drought in the intervening time is likely.

5) *To identify the distinguishing ecological variables separating trees that were alive and red stage mortality in 2016, at both the broad scale of a large part of the southern Sierra Nevada and the narrow scale of the Soaproot Saddle area.*

Using the results generated by Chapters 3 and 4, and some additional random sampling, I was able to accomplish this goal in Chapter 5. At the scale of a large swath of the southern Sierra Nevada, I found the climate between 2013 and 2015, specifically temperature and precipitation, to be highly predictive of 2016 tree mortality. Proximity to groups of dead trees in 2015 was also highly predictive of 2016 tree mortality. At the scale of Soaproot Saddle, the canopy surrounding a target tree, when evaluated at larger scales (a 45 m radius around a target tree was found to be optimal) was predictive of tree mortality. Canopies that fell within this radius that had more openings, more species diversity around them, and more open understories were found to be more likely to survive drought. Distances associated with local competition (a 10 – 20 m radius around a target tree) showed little predictive power for tree mortality. These results indicate that local microsite, and likely the influence it has on the movement of bark beetles around a target tree, impact an individual's chances of survival. Local competition, in contrast, does not appear to be influential on tree survival under the severe drought conditions experienced in 2016. From this research, I recommend land managers focus on promoting stand conditions that are species and structurally diverse, including openings. I also recommend that, if treatments are meant to perpetuate pine, land managers focus on cooler, wetter areas with higher growing site conditions.

6.2 Future Research

Much of the research presented in Chapters 2 and 3 of this dissertation were meant to lay the groundwork for a future spaceborne imaging spectrometer's ability to perform ecosystem-wide change detection. This was done using HyspIRI field campaign data acquired between 2013 and 2015. However, these data can only go so far. As discussed in Chapter 3, there are several complexities in airborne data that would not be present in spaceborne data. When an ecosystem-wide analysis is undertaken, the relatively narrow image swath size of airborne data means BRDF differences between flight lines needs to be accounted for. Due to the expense of aircraft, from a global perspective, airborne remote sensing will always be limited in temporal resolution and area that can be covered.

The National Academy of Sciences Space Studies Board recently identified HyspIRI as a priority asset to launch with the next decade (National Academies of Sciences, Engineering, 2018). The methods and techniques for comparing fire severity to MESMA generated cover fractions in Chapter 2 could be conducted on a global scale once this happens. Development of a globally applicable spectral library for the separation of GV, NPV, soil, and ash will be an important first step in this research. Ideally, MESMA, dNBR, and other remote sensing based fire severity extraction techniques will then be tested over a diverse set of ecosystems across the earth, accompanied with appropriate validation data. Such a series of studies would be time-consuming, expensive, and likely require collaboration between multiple research teams. However, the benefit of a globally objective and easily comparable method for evaluating fire severity would be of enormous value to field of ecology and understanding climate change's impact on fire behavior.

Similarly, a spaceborne imaging spectrometer would allow the results of Chapter 3 to be interpreted across the globe. The best means of including multi-temporal information in

identifying tree mortality is a topic of active research (Senf et al., 2017), so the importance of seasonal variability in the imaging spectroscopy based classification presented in Chapter 3 is of particular interest. The results of Chapter 3 suggest that imaging spectroscopy's sensitivity to subtle chemical changes within plants will create new possibilities for mortality identification using multi-temporal data. The Sierra Nevada during an extreme drought also posed unique challenges for change detection, since, among other factors, understory die-back was also occurring. Disturbance detection algorithms using spaceborne imaging spectrometer should be tested under a wide variety of ecosystems and conditions. Before a spaceborne imaging spectrometer is launched, further research using airborne imaging spectroscopy could test applying previously studied methods in new ecosystems or other forms of comparisons across large areas. The more potentially global methods are developed before launch, the more immediate value a spaceborne imaging spectrometer will have.

Not all the research performed in this dissertation lends itself to being conducted with spaceborne assets. The remote sensing necessary for the research in Chapter 4, fine spatial resolution imaging spectroscopy and lidar, is only possible by aircraft. While certainly not the first study to demonstrate the synergy of high spatial resolution imaging spectroscopy and lidar (Asner and Martin, 2009; Koetz et al., 2007), Chapter 4 demonstrated a novel means for disturbance monitoring. Although the exact location, timing, and nature of most forms of disturbance are difficult to predict, the methods in Chapter 4 represent a possible framework for collecting a baseline dataset that could be immediately useful when a disturbance does occur. While expensive, flying this form of remote sensing over a much larger area would have produced a more spatially robust effects analysis in Chapter 5 and

more valuable information for land managers. The more area that is monitored using a combination of high spatial resolution airborne imaging spectroscopy and lidar, the more likely future disturbances can be captured and their dynamics better understood. The methods of Chapter 4 could be replicated in other areas with diverse species assemblages. The type and quality of *in situ* data collected in association with future flights should also be carefully considered and attempted to be made as compatible with a diverse set of potential study goals as possible. The relatively low number and poor precision of the GPS locations of individual trees identified in association with the NEON project was a source of error in Chapter 4 that could have been avoided. Paz-Kagan et al. (2017) used one possible successful workflow; the remote sensing data was first acquired and then placed into field tablets with GPS units. In this manner, a match between the remote sensing data and the field data was assured.

While the successful use of WorldView imagery in Chapter 4 for post-drought analysis demonstrated that only a baseline fine spatial resolution imaging spectroscopy and lidar dataset is needed for successful change detection analysis, Soaproot Saddle was flown by the NEON AOP again in 2017 (as of the time of writing, this data has not been publically released, however). Determining whether an individual tree object identified in the 2013 data was alive or dead in 2017 would be possible with high accuracy using this data. The data could also be used to increase the accuracy of the tree crown object algorithm and, for the trees that were still alive, the species classification. Improved maps of live and dead tree locations (Figure 4.5) and estimates of the demographic impact of the drought (Figure 4.6) could be created. The baseline established in 2013 combined with future acquisitions of Soaproot Saddle with the NEON AOP could be used to monitor long-term demographic

change in response to this event, such as the rate and species composition of regeneration through time.

References

Abrams, M.D., 1992. Fire and the Development of Oak Forests. Bioscience 42, 346–353. doi:10.2307/1311781

Adams, J.B., Gillespie, A.R., 2006. Remote sensing of landscapes with spectral images: A physical modeling approach. Cambridge University Press.

Adams, J.B., Smith, M.O., Johnson, P.E., 1986. Spectral mixture modeling: A new analysis of rock and soil types at the Viking Lander 1 Site. J. Geophys. Res. Solid Earth 91, 8098–8112. doi:10.1029/JB091iB08p08098

AghaKouchak, A., Cheng, L., Mazdiyasni, O., Farahmand, A., 2014. Global warming and changes in risk of concurrent climate extremes: Insights from the 2014 California drought. Geophys. Res. Lett. 41, 8847–8852. doi:10.1002/2014GL062308

Ahern, F.J., 1988. The effects of bark beetle stress on the foliar spectral reflectance of lodgepole pine. Int. J. Remote Sens. 9, 1451–1468. doi:10.1080/01431168808954952

Allen, C.D., Breshears, D.D., McDowell, N.G., 2015. On underestimation of global vulnerability to tree mortality and forest die-off from hotter drought in the Anthropocene. Ecosphere 6, 1–55. doi:10.1890/ES15-00203.1

Allen, C.D., Macalady, A.K., Chenchouni, H., Bachelet, D., McDowell, N., Vennetier, M., Kitzberger, T., Rigling, A., Breshears, D.D., Hogg, E.H. (Ted), Gonzalez, P., Fensham, R., Zhang, Z., Castro, J., Demidova, N., Lim, J.H., Allard, G., Running, S.W., Semerci, A., Cobb, N., 2010. A global overview of drought and heat-induced tree mortality reveals emerging climate change risks for forests. For. Ecol. Manage. 259, 660–684. doi:10.1016/j.foreco.2009.09.001

Alonzo, M., Bookhagen, B., Roberts, D.A., 2014. Urban tree species mapping using hyperspectral and lidar data fusion. Remote Sens. Environ. 148, 70–83. doi:10.1016/j.rse.2014.03.018

Alonzo, M., Roth, K., Roberts, D.A., 2013. Identifying santa barbara's urban tree species from AVIRIS imagery using canonical discriminant analysis. Remote Sens. Lett. 4, 513–521. doi:10.1080/2150704X.2013.764027

Anderegg, W.R.L., Hicke, J.A., Fisher, R.A., Allen, C.D., Aukema, J., Bentz, B., Hood, S., Lichstein, J.W., Macalady, A.K., Mcdowell, N., Pan, Y., Raffa, K., Sala, A., Shaw,

J.D., Stephenson, N.L., Tague, C., Zeppel, M., 2015. Tree mortality from drought, insects, and their interactions in a changing climate. New Phytol. 208, 674–683. doi:10.1111/nph.13477

Andersen, H.-E., Reutebuch, S.E., McGaughey, R.J., 2006. A rigorous assessment of tree height measurements obtained using airborne lidar and conventional field methods. Can. J. Remote Sens. 32, 355–366. doi:10.5589/m06-030

Asner, G.P., 1998. Biophysical and biochemical sources of variability in canopy reflectance. Remote Sens. Environ. 64, 234–253. doi:10.1016/S0034-4257(98)00014-5

Asner, G.P., Brodrick, P.G., Anderson, C.B., Vaughn, N., Knapp, D.E., Martin, R.E., 2016. Progressive forest canopy water loss during the 2012–2015 California drought. Proc. Natl. Acad. Sci. 113, E249–E255. doi:10.1073/pnas.1523397113

Asner, G.P., Lobell, D.B., 2000. A biogeophysical approach for automated SWIR unmixing of soils and vegetation. Remote Sens. Environ. 74, 99–112. doi:10.1016/S0034-4257(00)00126-7

Asner, G.P., Martin, R.E., 2009. Airborne spectranomics: Mapping canopy chemical and taxonomic diversity in tropical forests. Front. Ecol. Environ. 7, 269–276. doi:10.1890/070152

Baguskas, S.A., Peterson, S.H., Bookhagen, B., Still, C.J., 2014. Evaluating spatial patterns of drought-induced tree mortality in a coastal California pine forest. For. Ecol. Manage. 315, 43–53.

Baig, M.H.A., Zhang, L., Shuai, T., Tong, Q., 2014. Derivation of a tasselled cap transformation based on Landsat 8 at-satellite reflectance. Remote Sens. Lett. 5, 423–431. doi:10.1080/2150704X.2014.915434

Baldridge, A.M., Hook, S.J., Crowley, J.K., Marion, G.M., Kargel, J.S., Michalski, J.L., Thomson, B.J., De Souza Filho, C.R., Bridges, N.T., Brown, A.J., 2009. Contemporaneous deposition of phyllosilicates and sulfates: Using Australian acidic saline lake deposits to describe geochemical variability on Mars. Geophys. Res. Lett. 36, 1–6. doi:10.1029/2009GL040069

Bates, B.C., Kundzewicz, Z.W., Wu, S., Palutikof, J.P., 2008. Climate Change and Water: technical paper vi., Climate change and water. Intergovernmental Panel on Climate Change (IPCC). doi:10.1016/j.jmb.2010.08.039

Belgiu, M., Dragut, L., 2016. Random forest in remote sensing: A review of applications and future directions. ISPRS J. Photogramm. Remote Sens. 114, 24–31. doi:10.1016/j.isprsjprs.2016.01.011

Bentz, B.J., Regniere, J., Fettig, C.J., Hansen, M., Hayes, J., Hicke, J.A., Kelsey, R., Negrón, J.F., Seybold, S., 2010. Climate Change and Bark beetles of the Western United States and Canada: Direct and Indirect Effects. Bioscience 60, 602–613. doi:10.1525/bio.2010.60.8.6

Berg, N., Hall, A., 2015. Increased interannual precipitation extremes over California under climate change. J. Clim. 28, 6324–6334. doi:10.1175/JCLI-D-14-00624.1

Biging, G.S., Dobbertin, M., 1992. A comparison of distance-dependent competition measures for height and basal growth of individual conifer trees. For. Sci. 38, 695–720.

Blackburn, G.A., 1998. Spectral indices for estimating photosynthetic pigment concentrations: A test using senescent tree leaves. Int. J. Remote Sens. 19, 657–675. doi:10.1080/014311698215919

Boardman, J., Kruse, F., Green, R.O., 1995. Mapping Target Signatures Via Partial Unmixing of AVIRIS Data, in: Summaries of the Fifth Annual JPL Airborne Earth Science Workshop. Volume 1: AVIRIS Workshop; P 23-26. pp. 23–26.

Breiman, L., 2001. Random forests. Mach. Learn. 45, 5–32. doi:10.1023/A:1010933404324

Burns, D.A., Ciurczak, E.W., 2007. Handbook of near-infrared analysis, 3rd editio. ed. CRC Press.

Cansler, C.A., McKenzie, D., 2012. How robust are burn severity indices when applied in a new region? Evaluation of alternate field-based and remote-sensing methods. Remote Sens. 4, 456–483. doi:10.3390/rs4020456

Canty, M.J., Nielsen, A.A., Schmidt, M., 2004. Automatic radiometric normalization of multitemporal satellite imagery. Remote Sens. Environ. 91, 441–451. doi:10.1016/j.rse.2003.10.024

Cayan, D.R., Das, T., Pierce, D.W., Barnett, T.P., Tyree, M., Gershunov, A., 2010. Future dryness in the southwest US and the hydrology of the early 21st century drought. Proc. Natl. Acad. Sci. 107, 21271–6. doi:10.1073/pnas.0912391107

Choat, B., Jansen, S., Brodribb, T.J., Cochard, H., Delzon, S., Bhaskar, R., Bucci, S.J., Feild, T.S., Gleason, S.M., Hacke, U.G., Jacobsen, A.L., Lens, F., Maherali, H.,

Martínez-Vilalta, J., Mayr, S., Mencuccini, M., Mitchell, P.J., Nardini, A., Pittermann, J., Pratt, R.B., Sperry, J.S., Westoby, M., Wright, I.J., Zanne, A.E., 2012. Global convergence in the vulnerability of forests to drought. Nature 491, 752–755. doi:10.1038/nature11688

Chornesky, E.A., Ackerly, D.D., Beier, P., Davis, F.W., Flint, L.E., Lawler, J.J., Moyle, P.B., Moritz, M.A., Scoonover, M., Byrd, K., Alvarez, P., Heller, N.E., Micheli, E.R., Weiss, S.B., 2015. Adapting California's ecosystems to a changing climate. Bioscience 65, 247–262. doi:10.1093/biosci/biu233

Chuvieco, E., Huete, A., 2009. Fundamentals of Satellite Remote Sensing. CRC Press.

Chuvieco, E., Riaño, D., Danson, F.M., Martin, P., 2006. Use of a radiative transfer model to simulate the postfire spectral response to burn severity. J. Geophys. Res. Biogeosciences 111, 1–15. doi:10.1029/2005JG000143

Clark, J.S., Iverson, L., Woodall, C.W., Allen, C.D., Bell, D.M., Bragg, D.C., D'Amato, A.W., Davis, F.W., Hersh, M.H., Ibanez, I., Jackson, S.T., Matthews, S., Pederson, N., Peters, M., Schwartz, M.W., Waring, K.M., Zimmermann, N.E., 2016. The impacts of increasing drought on forest dynamics, structure, and biodiversity in the United States. Glob. Chang. Biol. 22, 2329–2352. doi:10.1111/gcb.13160

Clark, R.N., Roush, T.L., 1984. Reflectance spectroscopy: Quantitative analysis techniques for remote sensing applications. J. Geophys. Res. Solid Earth 89, 6329–6340. doi:10.1029/JB089iB07p06329

Cocke, A.E., Fulé, P.Z., Crouse, J.E., 2005. Comparison of burn severity assessments using Differenced Normalized Burn Ratio and ground data. Int. J. Wildl. Fire 14, 189. doi:10.1071/WF04010

Cohen, J., 1968. Weighted kappa: Nominal scale agreement provision for scaled disagreement or partial credit. Psychol. Bull. 70(4), 213–220.

Cohen, J., 1960. A Coefficent of Agreement for Nominal Scales 20, 37–46. doi:https://doi.org/10.1177/001316446002000104

Congalton, R.G., Green, K., 1999. Assessing the Accuracy of Remotely Sensed Data: Principles and Pratices. CRC Press.

Coops, N.C., Johnson, M., Wulder, M.A., White, J.C., 2006. Assessment of QuickBird high spatial resolution imagery to detect red attack damage due to mountain pine beetle

infestation. Remote Sens. Environ. 103, 67–80. doi:10.1016/j.rse.2006.03.012

Crist, E.P., 1985. A TM Tasseled Cap equivalent transformation for reflectance factor data. Remote Sens. Environ. 17, 301–306. doi:10.1016/0034-4257(85)90102-6

Curran, P.J., 1989. Remote sensing of foliar chemistry. Remote Sens. Environ. 30, 271–278. doi:10.1016/0034-4257(89)90069-2

Cutler, R.D., Edwards, T.C., Beard, K.H., Cutler, A., Hess, K.T., Gibson, J., Lawler, J.A., 2007. Random Forests for Classification in Ecology. Ecology 88, 2783–2792. doi:10.1890/07-0539.1

Dalponte, M., Bruzzone, L., Gianelle, D., 2012. Tree species classification in the Southern Alps based on the fusion of very high geometrical resolution multispectral/hyperspectral images and LiDAR data. Remote Sens. Environ. 123, 258–270. doi:10.1016/j.rse.2012.03.013

Dalponte, M., Bruzzone, L., Gianelle, D., 2008. Fusion of hyperspectral and LIDAR remote sensing data for classification of complex forest areas. Geosci. Remote Sensing, IEEE Trans. 46, 1416–1427. doi:10.1109/TGRS.2008.916480

Dalponte, M., Ørka, H.O., Ene, L.T., Gobakken, T., Næsset, E., 2014. Tree crown delineation and tree species classification in boreal forests using hyperspectral and ALS data. Remote Sens. Environ. 140, 306–317. doi:10.1016/j.rse.2013.09.006

Daly, C., Halbleib, M., Smith, J.I., Gibson, W.P., Doggett, M.K., Taylor, G.H., Curtis, J., Pasteris, P.P., 2008. Physiographically sensitive mapping of climatological temperature and precipitation across the conterminous United States. Int. J. Climatol. 28, 2031–2064. doi:10.1002/joc

Das, A., Battles, J., Stephenson, N.L., van Mantgem, P.J., 2011. The contribution of competition to tree mortality in old-growth coniferous forests. For. Ecol. Manage. 261, 1203–1213. doi:10.1016/j.foreco.2010.12.035

Das, A.J., Stephenson, N.L., Davis, K.P., 2016. Why do trees die? Characterizing the drivers of background tree mortality. Ecology 97, 2616–2627. doi:10.1002/ecy.1497

Das, A.J., Stephenson, N.L., Flint, A., Das, T., van Mantgem, P.J., 2013. Climatic Correlates of Tree Mortality in Water- and Energy-Limited Forests. PLoS One 8. doi:10.1371/journal.pone.0069917

Daughtry, C.S.T., 2001. Discriminating Crop Residues from Soil by Shortwave Infrared

Reflectance. Agron. J. 93, 125–131. doi:10.2134/agronj2001.931125x

Daughtry, C.S.T., Walthall, C., Kim, M., de Colstoun, E., McMurtrey, J., 2000. Estimating Corn Leaf Chlorophyll Concentration from Leaf and Canopy Reflectance. Remote Sens. Environ. 74, 229–239. doi:10.1016/S0034-4257(00)00113-9

de la Mata, R., Hood, S., Sala, A., 2017. Insect outbreak shifts the direction of selection from fast to slow growth rates in the long-lived conifer *Pinus ponderosa*. Proc. Natl. Acad. Sci. 114, 7391–7396. doi:10.1073/pnas.1700032114

De Santis, A., Chuvieco, E., 2009. GeoCBI: A modified version of the Composite Burn Index for the initial assessment of the short-term burn severity from remotely sensed data. Remote Sens. Environ. 113, 554–562. doi:10.1016/j.rse.2008.10.011

Dennison, P.E., Brewer, S. c., Arnold, J.D., Moritz, M. a., 2014. Large Wildfire Trend in the Western United States, 1984-2011. Geophys. Res. Lett. 41, 2928–2933. doi:10.1002/2014GL061184.Received

Dennison, P.E., Brunelle, A.R., Carter, V.A., 2010. Assessing canopy mortality during a mountain pine beetle outbreak using GeoEye-1 high spatial resolution satellite data. Remote Sens. Environ. 114, 2431–2435. doi:10.1016/j.rse.2010.05.018

Dennison, P.E., Halligan, K.Q., Roberts, D.A., 2004. A comparison of error metrics and constraints for multiple endmember spectral mixture analysis and spectral angle mapper. Remote Sens. Environ. 93, 359–367. doi:10.1016/j.rse.2004.07.013

Dennison, P.E., Roberts, D.A., 2003. Endmember selection for multiple endmember spectral mixture analysis using endmember average RMSE. Remote Sens. Environ. 87, 123–135. doi:10.1016/S0034-4257(03)00135-4

Dennison, P.E., Roberts, D.A., Thorgusen, S.R., Regelbrugge, J.C., Weise, D., Lee, C., 2003. Modeling seasonal changes in live fuel moisture and equivalent water thickness using a cumulative water balance index. Remote Sens. Environ. 88, 442–452. doi:10.1016/j.rse.2003.08.015

Díaz-Uriarte, R., Alvarez de Andrés, S., 2006. Gene selection and classification of microarray data using random forest. BMC Bioinformatics 7, 3. doi:10.1186/1471-2105-7-3

Diaz, H.F., Wahl, E.R., 2015. Recent California water year precipitation deficits: A 440-year perspective. J. Clim. 28, 4637–4652. doi:10.1175/JCLI-D-14-00774.1

Diffenbaugh, N.S., Swain, D.L., Touma, D., 2015. Anthropogenic warming has increased drought risk in California. Proc. Natl. Acad. Sci. 112, 3931–3936. doi:10.1073/pnas.1422385112

Dubayah, R.O., Drake, J.B., 2000. Lidar remote sensing for forestry. J. For. 98, 44–46.

Dudley, K.L., Dennison, P.E., Roth, K.L., Roberts, D.A., Coates, A.R., 2015. A multi-temporal spectral library approach for mapping vegetation species across spatial and temporal phenological gradients. Remote Sens. Environ. 167, 121–134. doi:10.1016/j.rse.2015.05.004

Edburg, S.L., Hicke, J.A., Brooks, P.D., Pendall, E.G., Ewars, B.E., Norton, U., Gochis, D., Guttman, E.D., Meddens, J.H.A., 2012. Cascading impacts of bark beetle-caused tree mortality on coupled biogeophysical and biogeochemical processes. Front. Ecol. Environ. 10, 416–424.

Edson, C., Wing, M.G., 2011. Airborne light detection and ranging (LiDAR) for individual tree stem location, height, and biomass measurements, Remote Sensing. doi:10.3390/rs3112494

Ellison, A.M., Bank, M.S., Clinton, B.D., Colburn, E.A., Elliott, K., Ford, C.R., Foster, D.R., Kloeppel, B.D., Knoepp, J.D., Lovett, G.M., Mohan, J., Orwig, D.A., Rodenhouse, N.L., Sobczak, W. V., Stinson, K.A., Stone, J.K., Swan, C.M., Thompson, J., Von Holle, B., Webster, J.R., 2005. Loss of foundation species: Consequences for the structure and dynamics of forested ecosystems. Front. Ecol. Environ. 3, 479–486. doi:10.1890/1540-9295(2005)003[0479:LOFSCF]2.0.CO;2

Epting, J., Verbyla, D., Sorbel, B., 2005. Evaluation of remotely sensed indices for assessing burn severity in interior Alaska using Landsat TM and ETM+. Remote Sens. Environ. 96, 328–339. doi:10.1016/j.rse.2005.03.002

Falkowski, M.J., Smith, A.M.S., Gessler, P.E., Hudak, A.T., Vierling, L.A., Evans, J.S., 2008. The influence of conifer forest canopy cover on the accuracy of two individual tree measurement algorithms using lidar data. Can. J. Remote Sens. 34, 338–350. doi:10.5589/m08-055

Fassnacht, F.E., Latifi, H., Ghosh, A., Joshi, P.K., Koch, B., 2014. Assessing the potential of hyperspectral imagery to map bark beetle-induced tree mortality. Remote Sens. Environ. 140, 533–548. doi:10.1016/j.rse.2013.09.014

Fassnacht, F.E., Neumann, C., Forster, M., Buddenbaum, H., Ghosh, A., Clasen, A., Joshi, P.K., Koch, B., 2014. Comparison of feature reduction algorithms for classifying tree species with hyperspectral data on three central european test sites. IEEE J. Sel. Top. Appl. Earth Obs. Remote Sens. 7, 2547–2561. doi:10.1109/JSTARS.2014.2329390

Fernández-Delgado, M., Cernadas, E., Barro, S., Amorim, D., Amorim Fernández-Delgado, D., 2014. Do we Need Hundreds of Classifiers to Solve Real World Classification Problems? J. Mach. Learn. Res. 15, 3133–3181. doi:10.1016/j.csda.2008.10.033

Fettig, C.J., Klepzig, K.D., Billings, R.F., Munson, A.S., Nebeker, T.E., Negrón, J.F., Nowak, J.T., 2007. The effectiveness of vegetation management practices for prevention and control of bark beetle infestations in coniferous forests of the western and southern United States. For. Ecol. Manage. 238, 24–53. doi:10.1016/j.foreco.2006.10.011

Franke, J., Roberts, D.A., Halligan, K., Menz, G., 2009. Hierarchical Multiple Endmember Spectral Mixture Analysis (MESMA) of hyperspectral imagery for urban environments. Remote Sens. Environ. 113, 1712–1723. doi:10.1016/j.rse.2009.03.018

Franklin, S.E., Wulder, M.A., Skakun, R.S., Carroll, A.L., 2003. Mountain Pine Beetle Red-Attack Forest Damage Classification Using Stratified Landsat TM Data in British Columbia, Canada. Photogramm. Eng. Remote Sens. 69, 283–288. doi:10.14358/PERS.69.3.283

Gamon, A.J.A., Serrano, L., Surfus, J.S., 1997. The Photochemical Reflectance Index: An Optical Indicator of Photosynthetic Radiation Use Efficiency across Species, Functional Types, and Nutrient Levels. Oceologia 112, 492–501.

Gamon, J.A., Surfus, J.S., 1999. Assessing leaf pigment content and activity with a reflectometer. New Phytol. 143, 105–117. doi:10.1046/j.1469-8137.1999.00424.x

Ganey, J.L., Vojta, S.C., 2011. Tree mortality in drought-stressed mixed-conifer and ponderosa pine forests, Arizona, USA. For. Ecol. Manage. 261, 162–168. doi:10.1016/j.foreco.2010.09.048

Gao, B.-C., Goetz, A.F.H., 1990. Column atmospheric water vapor retrievals from airborne imaging spectrometer data. J. Geophys. Res. - Atmos. 95, 3549–3564. doi:10.1029/JD095iD04p03549

Gao, B.C., 1996. NDWI - A normalized difference water index for remote sensing of

vegetation liquid water from space. Remote Sens. Environ. 58, 257–266. doi:10.1016/S0034-4257(96)00067-3

Ghosh, A., Fassnacht, F.E., Joshi, P.K., Kochb, B., 2014. A framework for mapping tree species combining hyperspectral and LiDAR data: Role of selected classifiers and sensor across three spatial scales. Int. J. Appl. Earth Obs. Geoinf. 26, 49–63. doi:10.1016/j.jag.2013.05.017

Gitelson, A.A., Gritz, Y., Merzlyak, M.N., 2003. Relationships between leaf chlorophyll content and spectral reflectance and algorithms for non-destructive chlorophyll assessment in higher plant leaves. J. Plant Physiol. 160, 271–282. doi:10.1078/0176-1617-00887

Gitelson, A.A., Kaufman, Y.J., Stark, R., Rundquist, D., 2002a. Novel algorithms for remote estimation of vegetation fraction. Remote Sens. Environ. 80, 76–87. doi:10.1016/S0034-4257(01)00289-9

Gitelson, A.A., Merzlyak, M.N., Chivkunova, O.B., 2001. Optical Properties and Nondestructive Estimation of Anthocyanin Content in Plant Leaves Optical Properties and Nondestructive Estimation of Anthocyanin Content in Plant Leaves. Photochem. Photobiol. 74, 38–45. doi:10.1562/0031-8655(2001)074<0038

Gitelson, A.A., Zur, Y., Chivkunova, O.B., Merzlyak, M.N., 2002b. Assessing carotenoid content in plant leaves with reflectance spectroscopy assessing carotenoid content in plant leaves with reflectance. Photochem. Photobiol. 75, 272–281. doi:10.1562/0031-8655(2002)075<0272

Gonzalez, P., Asner, G.P., Battles, J.J., Lefsky, M.A., Waring, K.M., Palace, M., 2010. Forest carbon densities and uncertainties from Lidar, QuickBird, and field measurements in California. Remote Sens. Environ. 114, 1561–1575. doi:10.1016/j.rse.2010.02.011

Goulden, M.L., Anderson, R.G., Bales, R.C., Kelly, A.E., Meadows, M., Winston, G.C., 2012. Evapotranspiration along an elevation gradient in California's Sierra Nevada. J. Geophys. Res. Biogeosciences 117, 1–13. doi:10.1029/2012JG002027

Green, A.A., Berman, M., Switzer, P., Craig, M.D., 1988. A Transformation for Ordering Multispectral Data in Terms of Image Quality with Implications for Noise Removal. IEEE Trans. Geosci. Remote Sens. 26, 65–74. doi:10.1109/36.3001

Green, R.O., Eastwood, M.L., Sarture, C.M., Chrien, T.G., Aronsson, M., Chippendale, B.J., Faust, J.A., Pavri, B.E., Chovit, C.J., Solis, M., Olah, M.R., Williams, O., 1998. Imaging spectroscopy and the Airborne Visible/Infrared Imaging Spectrometer (AVIRIS). Remote Sens. Environ. 65, 227–248. doi:10.1016/S0034-4257(98)00064-9

Guan, H., Li, J., Chapman, M., Deng, F., Ji, Z., Yang, X., 2013. Integration of orthoimagery and lidar data for object-based urban thematic mapping using random forests. Int. J. Remote Sens. 34, 5166–5186. doi:10.1080/01431161.2013.788261

Guanter, L., Kaufmann, H., Segl, K., Foerster, S., Rogass, C., Chabrillat, S., Kuester, T., Hollstein, A., Rossner, G., Chlebek, C., Straif, C., Fischer, S., Schrader, S., Storch, T., Heiden, U., Mueller, A., Bachmann, M., Muhle, H., Muller, R., Habermeyer, M., Ohndorf, A., Hill, J., Buddenbaum, H., Hostert, P., Van Der Linden, S., Leitao, P.J., Rabe, A., Doerffer, R., Krasemann, H., Xi, H., Mauser, W., Hank, T., Locherer, M., Rast, M., Staenz, K., Sang, B., 2015. The EnMAP spaceborne imaging spectroscopy mission for earth observation. Remote Sens. 7, 8830–8857. doi:10.3390/rs70708830

Guarín, A., Taylor, A.H., 2005. Drought triggered tree mortality in mixed conifer forests in Yosemite National Park, California, USA. For. Ecol. Manage. 218, 229–244. doi:10.1016/j.foreco.2005.07.014

Ham, J., Chen, Y., Crawford, M.M., Ghosh, J., 2005. Investigation of the Random Forest Framework for Classification of Hyperspectral Data. IEEE Trans. Geosci. Remote Sens. 43, 492–501. doi:10.1109/TGRS.2004.842481

Hamlin, L., Green, R.O., Mouroulis, P., Eastwood, M., Wilson, D., Dudik, M., Paine, C., 2011. Imaging Spectrometer Science Measurements for Terrestrial Ecology : AVIRIS and New Developments 1–8.

Hardisky, M.A., Klemas, V., Smart, R.M., 1983. The influence of Soil Salinity, Growth Form, and Leaf Moisture on the Spectral Radiance of Spartina alterniflora Canopies. Photogramm. Eng. Remote Sensing 49, 77–83.

Harris, L., Taylor, A.H., 2015. Topography, Fuels, and Fire Exclusion Drive Fire Severity of the Rim Fire in an Old-Growth Mixed-Conifer Forest, Yosemite National Park, USA. Ecosystems 18, 1192–1208. doi:10.1007/s10021-015-9890-9

Harvey, B.J., Donato, D.C., Romme, W.H., Turner, M.G., 2013. Influence of recent bark beetle outbreak on fire severity and postfire tree regeneration in montane Douglas-fir

forests. Ecology 94, 2475–2486. doi:10.1890/13-0188.1

He, H., Garcia, E.A., 2009. Learning from imbalanced data. IEEE Trans. Knowl. Data Eng. 21, 1263–1284. doi:10.1109/TKDE.2008.239

Herold, M., Gardner, M.E., Roberts, D., 2003. Spectral resolution requirements for mapping urban areas. IEEE Trans. Geosci. Remote Sens. 41, 1907–1919. doi:10.1109/TGRS.2003.815238

Holland, V.L., Keil, D.J., 1996. California Vegetation. Kendall Hunt Publishing.

Hudak, A.T., Morgan, P., Bobbitt, M.J., Smith, A.M.S., Lewis, S.A., Lentile, L.B., Robichaud, P.R., Clark, J.T., Mckinley, R.A., 2007. the Relationship of Multispectral Satellite Imagery. Fire Ecol. 3, 64–90. doi:10.4996/fireecology.0301064

Hudiburg, T., Law, B., Turner, D.P., Campbell, J., Donato, D., Duane, M., 2009. Carbon dynamics of Oregon and Northern California forests and potential land-based carbon storage. Ecol. Appl. 19, 163–180. doi:10.1890/07-2006.1

Huete, A., Didan, K., Miura, T., Rodriguez, E.P., Gao, X., Ferreira, L.G., 2002. Overview of the radiometric and biophysical performance of the MODIS vegetation indices. Remote Sens. Environ. 83, 195–213. doi:10.1016/S0034-4257(02)00096-2

Irani, M., 2002. Multi-Frame Correpsondence Estimation Using Subspace Constraints. Int. J. Comput. Vis. 48, 173–194.

Jenkins, M.J., Hebertson, E., Page, W., Jorgensen, C.A., 2008. Bark beetles, fuels, fires and implications for forest management in the Intermountain West. For. Ecol. Manage. 254, 16–34. doi:10.1016/j.foreco.2007.09.045

Jia, G.J., Burke, I.C., Goetz, A.F.H., Kaufmann, M.R., Kindel, B.C., 2006. Assessing spatial patterns of forest fuel using AVIRIS data. Remote Sens. Environ. 102, 318–327. doi:10.1016/j.rse.2006.02.025

Jolly, W.M., Cochrane, M.A., Freeborn, P.H., Holden, Z.A., Brown, T.J., Williamson, G.J., Bowman, D.M.J.S., 2015. Climate-induced variations in global wildfire danger from 1979 to 2013. Nat. Commun. 6, 1–11. doi:10.1038/ncomms8537

Jordan, C.F., 1969. Derivation of Leaf-Area Index from Quality of Light on the Forest Floor. Ecology 50, 663–666. doi:10.2307/1936256

Kampe, T., Johnson, B.R., Kuester, M., Keller, M., 2010. NEON: the first continental-scale ecological observatory with airborne remote sensing of vegetation canopy biochemistry

and structure. J. Appl. Remote Sens. 4, 43510. doi:10.1117/1.3361375

Kampe, T., Leisso, N., Musinsky, J., Petroy, S., Karpowicz, B., 2013. The NEON 2013 Airborne Campaign at Domain 17 Terrestrial and Aquatic Sites in California. NEON Technical Memo 005. doi:10.13140/2.1.1513.1529

Kane, V.R., Cansler, C.A., Povak, N.A., Kane, J.T., McGaughey, R.J., Lutz, J.A., Churchill, D.J., North, M.P., 2015. Mixed severity fire effects within the Rim fire: Relative importance of local climate, fire weather, topography, and forest structure. For. Ecol. Manage. 358, 62–79. doi:10.1016/j.foreco.2015.09.001

Karpowicz, B.M., Leissio, N., Kampe, T.U., 2014. A synergistic approach to atmospheric correction of NEON's airborne hyperspectral data utilizing airborne solar spectral flux radiometers, ground based radiometers, and airborne hyperspectral imagers. Int. Geosci. Remote Sens. Symp. 2695–2698. doi:10.1109/IGARSS.2014.6947030

Kelly, A.E., Goulden, M.L., 2008. Rapid shifts in plant distribution with recent climate change. Proc. Natl. Acad. Sci. U. S. A. 105, 11823–11826. doi:10.1073/pnas.0802891105

Keshava, N., Mustard, J.F., 2002. Spectral unmixing. IEEE Signal Process. Mag. 19, 44–57. doi:10.1109/79.974727

Key, C.H., Benson, N.C., 2006. Landscape assessment: Sampling and analysis methods. USDA For. Serv. Gen. Tech. Rep. RMRS-GTR-164-CD 1–55. doi:10.1002/app.1994.070541203

Khanna, S., Santos, M.J., Ustin, S.L., Koltunov, A., Kokaly, R.F., Roberts, D.A., 2013. Detection of salt marsh vegetation stress and recovery after the Deepwater Horizon Oil Spill in Barataria Bay, Gulf of Mexico using AVIRIS data. PLoS One 8. doi:10.1371/journal.pone.0078989

Kim, M.S., 1994. The use of narrow spectral bands for improving remote sensing estimation of fractionally absorbed photosynthetically active radiation (fAPAR). University of Maryland, College Park, MD.

Koetz, B., Sun, G., Morsdorf, F., Ranson, K.J., Kneubühler, M., Itten, K., Allgöwer, B., 2007. Fusion of imaging spectrometer and LIDAR data over combined radiative transfer models for forest canopy characterization. Remote Sens. Environ. 106, 449–459. doi:10.1016/j.rse.2006.09.013

Kokaly, R., Clark, R., 1999. Spectroscopic Determination of Leaf Biochemistry Using Band-Depth Analysis of Absorption Features and Stepwise Multiple Linear Regression. Remote Sens. Environ. 67, 267–287. doi:10.1016/S0034-4257(98)00084-4

Kokaly, R.F., Rockwell, B.W., Haire, S.L., King, T.V.V., 2007. Characterization of post-fire surface cover, soils, and burn severity at the Cerro Grande Fire, New Mexico, using hyperspectral and multispectral remote sensing. Remote Sens. Environ. 106, 305–325. doi:10.1016/j.rse.2006.08.006

Kolb, T.E., Agee, J.K., Fulé, P.Z., McDowell, N.G., Pearson, K., Sala, A., Waring, R.H., 2007. Perpetuating old ponderosa pine. For. Ecol. Manage. 249, 141–157. doi:10.1016/j.foreco.2007.06.002

Koltunov, A., Ben-Dor, E., Ustin, S., 2008. Image construction using multitemporal observations and Dynamic Detection Models. Int. J. Remote Sens. 30, 57–83. doi:10.1080/01431160802220193

Koltunov A., Ustin, S. L., Quayle, B., Schwind, B., 2012. GOES Early Fire Detection (GOES-EFD) System Prototype, in: ASPRS 2012 Annual Conference.

Kruse, F., Lefkoff, A.B., Boardman, J.W., Heidebrecht, K.B., Shapiro, A.T., Barloon, P.J., Goetz, A.F.H., 1993. The spectral image processing system (SIPS)—interactive visualization and analysis of imaging spectrometer data. Remote Sens. Environ. 44, 145–163. doi:10.1016/0034-4257(93)90013-N

Latifi, H., Fassnacht, F.E., Schumann, B., Dech, S., 2014. Object-based extraction of bark beetle (Ips typographus L.) infestations using multi-date LANDSAT and SPOT satellite imagery. Prog. Phys. Geogr. 38, 755–785. doi:10.1177/0309133314550670

Lausch, A., Heurich, M., Gordalla, D., Dobner, H.J., Gwillym-Margianto, S., Salbach, C., 2013. Forecasting potential bark beetle outbreaks based on spruce forest vitality using hyperspectral remote-sensing techniques at different scales. For. Ecol. Manage. 308, 76–89. doi:10.1016/j.foreco.2013.07.043

Lee, C.M., Cable, M.L., Hook, S.J., Green, R.O., Ustin, S.L., Mandl, D.J., Middleton, E.M., 2015. An introduction to the NASA Hyperspectral InfraRed Imager (HyspIRI) mission and preparatory activities. Remote Sens. Environ. 167, 6–19. doi:10.1016/j.rse.2015.06.012

Lefsky, M.A., Cohen, W.B., Parker, G.G., HardingG, D.J., 2002. Lidar Remote Sensing for

Ecosystem Studies. Bioscience 52, 19. doi:10.1641/0006-3568(2002)052[0019:LRSFES]2.0.CO;2

Lentile, L.B., Holden, Z.A., Smith, A.M.S., Falkowski, M.J., Hudak, A.T., Morgan, P., Lewis, S.A., Gessler, P.E., Benson, N.C., 2006. Remote sensing techniques to assess active fire characteristics and post-fire effects. Int. J. Wildl. Fire 15, 319–345. doi:10.1071/WF05097

Lentile, L.B., Smith, A.M.S., Hudak, A.T., Morgan, P., Bobbitt, M.J., Lewis, S.A., Robichaud, P.R., 2009. Remote sensing for prediction of 1-year post-fire ecosystem condition. Int. J. Wildl. Fire 18, 594–608. doi:10.1071/WF07091

Li, J., 2004. Wavelet-based feature extraction for improved endmember abundance estimation in linear unmixing of hyperspectral signals. IEEE Trans. Geosci. Remote Sens. 42, 644–649. doi:10.1109/TGRS.2003.822750

Liang, L., Chen, Y., Hawbaker, T.J., Zhu, Z., Gong, P., 2014. Mapping mountain pine beetle mortality through growth trend analysis of time-series landsat data. Remote Sens. 6, 5696–5716. doi:10.3390/rs6065696

Liaw, A., Wiener, M., 2002. Classification and Regression by randomForest. R news 2, 18–22.

Lim, K., Treitz, P., Wulder, M., St-Onge, B., Flood, M., 2003. LiDAR remote sensing of forest structure. Prog. Phys. Geogr. 27, 88–106. doi:10.13016/M2D626

Lutz, J.A., Larson, A.J., Swanson, M.E., Freund, J.A., 2012. Ecological importance of large-diameter trees in a temperate mixed-conifer forest. PLoS One 7. doi:10.1371/journal.pone.0036131

Lutz, J.A., Matchett, J., Tarnay, L., Smith, D., Becker, K., Furniss, T., Brooks, M., 2017. Fire and the Distribution and Uncertainty of Carbon Sequestered as Aboveground Tree Biomass in Yosemite and Sequoia & Kings Canyon National Parks James. Land 6, 10. doi:10.3390/land6010010

Lydersen, J.M., North, M.P., Collins, B.M., 2014. Severity of an uncharacteristically large wildfire, the Rim Fire, in forests with relatively restored frequent fire regimes. For. Ecol. Manage. 328, 326–334. doi:10.1016/j.foreco.2014.06.005

Martin, M.., Newman, S.., Aber, J.., Congalton, R.., 1998. Determining forest species composition using high spectral resolution remote sensing data. Remote Sens. Environ.

65, 249–254. doi:10.1016/S0034-4257(98)00035-2

McGregor, M.D., Cole, D.N., 1985. Integrating management strategies for the mountain pine beetle with multiple-resource management of lodgepole pine forests. USDA For. Serv. Gen. Tech. Rep. INT-174.

Mcintyre, P.J., Thorne, J.H., Dolanc, C.R., Flint, A.L., Flint, L.E., Kelly, M., Ackerly, D.D., 2015. Twentieth-century shifts in forest structure in California: Denser forests, smaller trees, and increased dominance of oaks. Proc. Natl. Acad. Sci. 112, 1458–1463. doi:10.1073/pnas.1410186112

Meddens, A.J.H., Hicke, J.A., Vierling, L.A., Hudak, A.T., 2013. Evaluating methods to detect bark beetle-caused tree mortality using single-date and multi-date Landsat imagery. Remote Sens. Environ. 132, 49–58. doi:10.1016/j.rse.2013.01.002

Merton, R.N., Huntington, J.F., 1999. Early simulation results of the aries-1 satellite sensor for multi-temporal vegetation research derived from AVIRIS, in: Proceedings of the Eighth Annual JPL Airborne Earth Science Workshop, NASA Jet Propulsion Lab., Pasadena, CA.

Merzlyak, M.N., Gitelson, A.A., Chivkunova, O.B., Rakitin, V.Y., 1999. Non-destructive optical detection of pigment changes during leaf senescence and fruit ripening. Physiol. Plant. 106, 135–141. doi:10.1034/j.1399-3054.1999.106119.x

Meyer, M.D., North, M.P., Gray, A.N., Zald, H.S.J., 2007. Influence of soil thickness on stand characteristics in a Sierra Nevada mixed-conifer forest. Plant Soil 294, 113–123. doi:10.1007/s11104-007-9235-3

Miao, X., Gong, P., Swope, S., Pu, R., Carruthers, R., Anderson, G.L., Heaton, J.S., Tracy, C.R., 2006. Estimation of yellow starthistle abundance through CASI-2 hyperspectral imagery using linear spectral mixture models. Remote Sens. Environ. 101, 329–341. doi:10.1016/j.rse.2006.01.006

Millar, C.I., Stephenson, N.L., 2015. Temperate forest health in an era of emerging megadisturbance. Science (80-.). 349, 823–826. doi:10.1126/science.aaa9933

Millard, K., Richardson, M., 2015. On the importance of training data sample selection in Random Forest image classification: A case study in peatland ecosystem mapping. Remote Sens. 7, 8489–8515. doi:10.3390/rs70708489

Miller, J.D., Safford, H.D., Crimmins, M., Thode, A.E., 2009. Quantitative evidence for

increasing forest fire severity in the Sierra Nevada and southern Cascade Mountains, California and Nevada, USA. Ecosystems 12, 16–32. doi:10.1007/s10021-008-9201-9

Miller, J.D., Thode, A.E., 2007. Quantifying burn severity in a heterogeneous landscape with a relative version of the delta Normalized Burn Ratio (dNBR). Remote Sens. Environ. 109, 66–80. doi:10.1016/j.rse.2006.12.006

Morgan, P., Keane, R.E., Dillon, G.K., Jain, T.B., Hudak, A.T., Karau, E.C., Sikkink, P.G., Holden, Z.A., Strand, E.K., 2014. Challenges of assessing fire and burn severity using field measures, remote sensing and modelling. Int. J. Wildl. Fire 23, 1045–1060. doi:10.1071/WF13058

Mueller, R.C., Scudder, C.M., Porter, M.E., Talbot Trotter, R., Gehring, C.A., Whitham, T.G., 2005. Differential tree mortality in response to severe drought: Evidence for long-term vegetation shifts. J. Ecol. 93, 1085–1093. doi:10.1111/j.1365-2745.2005.01042.x

Naidoo, L., Cho, M.A., Mathieu, R., Asner, G., 2012. Classification of savanna tree species, in the Greater Kruger National Park region, by integrating hyperspectral and LiDAR data in a Random Forest data mining environment. ISPRS J. Photogramm. Remote Sens. 69, 167–179. doi:10.1016/j.isprsjprs.2012.03.005

National Academies of Sciences, Engineering, and M., 2018. Thriving on Our Changing Planet: A Decedal Strategy for Earth Observation from Space. The National Academies Press, Washington, DC. doi:https://doi.ori.10.17226/24938

Nelson, T.A., Boots, B., Wulder, M.A., Carroll, A.L., 2007. Environmental characteristics of mountain pine beete infestation hot spots. BC J. Ecosyst. Manag. 8, 91–108.

Niemann, K.O., Quinn, G., Stephen, R., Visintini, F., Parton, D., 2015. Hyperspectral Remote Sensing of Mountain Pine Beetle with an Emphasis on Previsual Assessment. Can. J. Remote Sens. 41, 191–202. doi:10.1080/07038992.2015.1065707

Oliver, C.D., Larson, B.C., 1990. Forest Stand Dynamics.

Oliver, W.W., 1995. Is self-thinning in ponderosa pine ruled by Dendroctonus bark beetles? Gen. Tech. Rep. - US Dep. Agric. For. Serv. 213–218.

Olofsson, P., Foody, G.M., Herold, M., Stehman, S. V., Woodcock, C.E., Wulder, M.A., 2014. Good practices for estimating area and assessing accuracy of land change. Remote Sens. Environ. 148, 42–57. doi:10.1016/j.rse.2014.02.015

Pal, M., Foody, G.M., 2010. Feature Selection for Classification of Hyperspectral Data by

SVM. Geosci. Remote Sensing, IEEE Trans. 48, 2297–2307. doi:10.1109/TGRS.2009.2039484

Parente, M., Plaza, A., 2010. Survey of geometric and statistical unmixing algorithms for hyperspectral images. 2nd Work. Hyperspectral Image Signal Process. Evol. Remote Sensing, WHISPERS 2010 - Work. Progr. doi:10.1109/WHISPERS.2010.5594929

Paz-Kagan, T., Brodick, P., Vaughn, N., Das, A., Stephenson, N.L., Nydick, K., Asner, G.P., 2017a. What mediates tree mortality during drought in the southern Sierra Nevada? Ecol. Appl. doi:10.1111/ijlh.12426

Paz-Kagan, T., Caras, T., Herrmann, I., Shachak, M., Karnieli, A., 2017b. Multiscale mapping of species diversity under changed land use using imaging spectroscopy. Ecol. Appl. 27, 1466–1484. doi:10.1002/eap.1540

Penuelas, J., Baret, F., Filella, I., 1995. Semi-empirical indices to assess carotenoids/chlorophyll a ratio from leaf spectral reflectance. Photosynthetica.

Penuelas, J., Pinol, J., Ogaya, R., Filella, I., 1997. Estimation of plant water concentration by the reflectance Water Index WI (R900/R970). Int. J. Remote Sens. 18, 2869–2875. doi:10.1080/014311697217396

Peterson, D.A., Hyer, E.J., Campbell, J.R., Fromm, M.D., Hair, J.W., Butler, C.F., Fenn, M.A., 2015. The 2013 Rim Fire: Implications for predicting extreme fire spread, pyroconvection, smoke emissions. Bull. Am. Meteorol. Soc. 96, 229–247. doi:10.1175/BAMS-D-14-00060.1

Peterson, S.H., Roberts, D.A., Beland, M., Kokaly, R.F., Ustin, S.L., 2015. Oil detection in the coastal marshes of Louisiana using MESMA applied to band subsets of AVIRIS data. Remote Sens. Environ. 159, 222–231. doi:10.1016/j.rse.2014.12.009

Pontius, J., Hallett, R., Martin, M., 2005. Using AVIRIS to assess hemlock abundance and early decline in the Catskills, New York. Remote Sens. Environ. 97, 163–173. doi:10.1016/j.rse.2005.04.011

Quintano, C., Fernández-Manso, A., Roberts, D.A., 2013. Multiple Endmember Spectral Mixture Analysis (MESMA) to map burn severity levels from Landsat images in Mediterranean countries. Remote Sens. Environ. 136, 76–88. doi:10.1016/j.rse.2013.04.017

R5-PR-034, 2016 Aerial Survey Results: California, 2017.

Radoux, J., Bogaert, P., 2017. Good practices for object-based accuracy assessment. Remote Sens. 9. doi:10.3390/rs9070646

Raffa, K.F., Aukema, B.H., Bentz, B.J., Carroll, A.L., Hicke, J.A., Turner, M.G., Romme, W.H., 2008. Cross-scale Drivers of Natural Disturbances Prone to Anthropogenic Amplification: The Dynamics of Bark Beetle Eruptions. Bioscience 58, 501. doi:10.1641/B580607

Roberts, D.A., Alonzo, M., Wetherley, E.B., Dudley, K.L., Dennison, P.E., 2017. Multiscale Analysis of Urban Areas Using Mixing Models, in: Integrating Scale in Remote Sensing and GIS. pp. 247–282. doi:10.1201/9781315373720-10

Roberts, D.A., Dennison, P.E., Gardner, M.E., Hetzel, Y., Ustin, S.L., Lee, C.T., 2003. Evaluation of the potential of Hyperion for fire danger assessment by comparison to the airborne visible/infrared imaging spectrometer. IEEE Trans. Geosci. Remote Sens. 41, 1297–1310. doi:10.1109/TGRS.2003.812904

Roberts, D.A., Gardner, M., Church, R., Ustin, S.L., Scheer, G., Green, R.O., 1998. Mapping chaparral in the Santa Monica Mountains using multiple endmember spectral mixture models. Remote Sens. Environ. 65, 267–279. doi:10.1016/S0034-4257(98)00037-6

Roberts, D.A., Green, R.O., Adams, J.B., 1997. Temporal and spatial patterns in vegetation and atmospheric properties from AVIRIS. Remote Sens. Environ. 62, 223–240. doi:10.1016/S0034-4257(97)00092-8

Roberts, D.A., Quattrochi, D.A., Hulley, G.C., Hook, S.J., Green, R.O., 2012. Synergies between VSWIR and TIR data for the urban environment: An evaluation of the potential for the Hyperspectral Infrared Imager (HyspIRI) Decadal Survey mission. Remote Sens. Environ. 117, 83–101. doi:10.1016/j.rse.2011.07.021

Roberts, D.A., Roth, K., Perroy, R., 2011. Hyperspectral Vegetation Indices, in: Thenkabail, P.S., Lyon, J.G., Huete, A. (Eds.), Hyperspectral Remote Sensing of Vegetation. CRC Press, pp. 309–328. doi:10.1201/b11222-20

Roberts, D.A., Smith, M.O., Adams, J.B., 1993. Green vegetation, nonphotosynthetic vegetation, and soils in AVIRIS data. Remote Sens. Environ. 44, 255–269. doi:10.1016/0034-4257(93)90020-X

Roberts, D.A., Ustin, S.L., Ogunjemiyo, S., Greenberg, J., Dobrowski, S.Z., Chen, J.,

Hinckley, T.M., 2004. Spectral and Structural Measures of Northwest Forest Vegetation at Leaf to Landscape Scales. Ecosystems 7, 545–562. doi:10.1007/s10021-004-0144-5

Robeson, S.M., 2015. Revisiting the recent California drought as an extreme value. Geophys. Res. Lett. 42, 6771–6779. doi:10.1002/2015GL064593

Robichaud, P.R., Lewis, S.A., Laes, D.Y.M., Hudak, A.T., Kokaly, R.F., Zamudio, J.A., 2007. Postfire soil burn severity mapping with hyperspectral image unmixing. Remote Sens. Environ. 108, 467–480. doi:10.1016/j.rse.2006.11.027

Rock, B.N., Vogelmann, J.E., Williams, D.L., Vogelmann, A.F., Hoshizaki, T., 1986. Remote detection of forest damage. Bioscience 36, 439–445. doi:10.2307/1310339

Rogan, J., Franklin, J., 2001. Mapping Wildfire Burn Severity in Southern California Forests and Shrublands Using Enhanced Thematic Mapper Imagery. Geocarto Int. 16, 91–106. doi:10.1080/10106040108542218

Roth, K.L., Dennison, P.E., Roberts, D.A., 2012. Comparing endmember selection techniques for accurate mapping of plant species and land cover using imaging spectrometer data. Remote Sens. Environ. 127, 139–152. doi:10.1016/j.rse.2012.08.030

Roth, K.L., Roberts, D.A., Dennison, P.E., Alonzo, M., Peterson, S.H., Beland, M., 2015. Differentiating plant species within and across diverse ecosystems with imaging spectroscopy. Remote Sens. Environ. 167, 135–151. doi:10.1016/j.rse.2015.05.007

Rouse, J.W., Hass, R.H., Schell, J.A., Deering, D.W., 1973. Monitoring vegetation systems in the great plains with ERTS. Third Earth Resour. Technol. Satell. Symp. 309–317. doi:citeulike-article-id:12009708

Roy, D.P., Wulder, M.A., Loveland, T.R., C.E., W., Allen, R.G., Anderson, M.C., Helder, D., Irons, J.R., Johnson, D.M., Kennedy, R., Scambos, T.A., Schaaf, C.B., Schott, J.R., Sheng, Y., Vermote, E.F., Belward, A.S., Bindschadler, R., Cohen, W.B., Gao, F., Hipple, J.D., Hostert, P., Huntington, J., Justice, C.O., Kilic, A., Kovalskyy, V., Lee, Z.P., Lymburner, L., Masek, J.G., McCorkel, J., Shuai, Y., Trezza, R., Vogelmann, J., Wynne, R.H., Zhu, Z., 2014. Landsat-8: Science and product vision for terrestrial global change research. Remote Sens. Environ. 145, 154–172. doi:10.1016/j.rse.2014.02.001

Saeys, Y., Inza, I., Larranaga, P., 2007. A review of feature selection techniques in

bioinformatics. Bioinformatics 23, 2507–2517. doi:10.1093/bioinformatics/btm344

Savage, M., 1994. Anthropogenic and natural disturbance and patterns of mortality in a mixed conifer forest in California. Can. J. For. Res. Can. Rech. For. 24, 1149–1159.

Schaaf, A.N., Dennison, P.E., Fryer, G.K., Roth, K.L., Roberts, D.A., 2011. Mapping Plant Functional Types at Multiple Spatial Resolutions Using Imaging Spectrometer Data. GIScience Remote Sens. 48, 324–344. doi:10.2747/1548-1603.48.3.324

Senf, C., Pflugmacher, D., Wulder, M.A., Hostert, P., 2015. Characterizing spectral-temporal patterns of defoliator and bark beetle disturbances using Landsat time series. Remote Sens. Environ. 170, 166–177. doi:10.1016/j.rse.2015.09.019

Senf, C., Seidl, R., Hostert, P., 2017. Remote sensing of forest insect disturbances: Current state and future directions. Int. J. Appl. Earth Obs. Geoinf. 60, 49–60. doi:10.1016/j.jag.2017.04.004

Serrano, L., Penuelas, J., Ustin, S.L., 2002. Remote sensing of nitrogen and lignin in Mediterranean vegetation from AVIRIS data: Decomposing biochemical from structural signals. Remote Sens. Environ. 81, 355–364.

Settle, J., Campbell, N., 1998. On the errors of two estimators of sub-pixel fractional cover when mixing is linear. IEEE Trans. Geosci. Remote Sens. 36, 163–170. doi:10.1109/36.655326

Sheppard, S., Picard, P., 2006. Visual-quality impacts of forest pest activity at the landscape level: A synthesis of published knowledge and research needs. Landsc. Urban Plan. 77, 321–342. doi:10.1016/j.landurbplan.2005.02.007

Smith, A.M.S., Eitel, J.U.H., Hudak, A.T., 2010. Spectral analysis of charcoal on soils: Implications for wildland fire severity mapping methods. Int. J. Wildl. Fire 19, 976–983. doi:10.1071/WF09057

Somers, B., Asner, G.P., 2013. Multi-temporal hyperspectral mixture analysis and feature selection for invasive species mapping in rainforests. Remote Sens. Environ. 136, 14–27. doi:10.1016/j.rse.2013.04.006

Somers, B., Asner, G.P., Tits, L., Coppin, P., 2011. Endmember variability in Spectral Mixture Analysis: A review. Remote Sens. Environ. 115, 1603–1616. doi:10.1016/j.rse.2011.03.003

Somers, B., Delalieux, S., Verstraeten, W.W., van Aardt, J.A.N., Albrigo, G.L., Coppin, P.,

2010. An automated waveband selection technique for optimized hyperspectral mixture analysis. Int. J. Remote Sens. 31, 5549–5568. doi:10.1080/01431160903311305

Steel, Z.L., Safford, H.D., Viers, J.H., 2015. The fire frequency-severity relationship and the legacy of fire suppression in California forests. Ecosphere 6, 8. doi:10.1890/ES14-00224.1

Stefano, P., Angelo, P., Simone, P., Filomena, R., Federico, S., Tiziana, S., Umberto, A., Vincenzo, C., Acito, N., Marco, D., Stefania, M., Giovanni, C., Raffaele, C., Roberto, D.B., Giovanni, L., Cristina, A., 2013. The PRISMA hyperspectral mission: Science activities and opportunities for agriculture and land monitoring. Int. Geosci. Remote Sens. Symp. 4558–4561. doi:10.1109/IGARSS.2013.6723850

Stehman, S. V., 2009. Sampling designs for accuracy assessment of land cover. Int. J. Remote Sens. 30, 5243–5272. doi:10.1080/01431160903131000

Storer, T.I., Usinger, R.L., Lukas, D., 2004. Sierra Nevada Natural History, 2nd Editio. ed. University of California Press.

Streutker, D.R., Glenn, N.F., 2006. LiDAR measurement of sagebrush steppe vegetation heights. Remote Sens. Environ. 102, 135–145. doi:10.1016/j.rse.2006.02.011

Thompson, D.R., Gao, B.C., Green, R.O., Roberts, D.A., Dennison, P.E., Lundeen, S.R., 2015. Atmospheric correction for global mapping spectroscopy: ATREM advances for the HyspIRI preparatory campaign. Remote Sens. Environ. 167, 64–77. doi:10.1016/j.rse.2015.02.010

Tompkins, S., Mustard, J.F., Pieters, C.M., Forsyth, D.W., 1997. Optimization of endmembers for spectral mixture analysis. Remote Sens. Environ. 59, 472–489. doi:10.1016/S0034-4257(96)00122-8

Tucker, C.J., 1979. Red and photographic infrared linear combinations for monitoring vegetation. Remote Sens. Environ. 8, 127–150. doi:10.1016/0034-4257(79)90013-0

US Department of Agriculture, 2009. FUSION/LDV: Software for LIDAR data analysis and visualization.

USFS, 2016. Forest Health Protection Arial Detection Survey [WWW Document]. www.fs.usda.gov/detail/r5/forest-grasslandhealth/.

Ustin, S.L., Gamon, J.A., 2010. Remote sensing of plant functional types. New Phytol. 186, 795–816. doi:10.1111/j.1469-8137.2010.03284.x

Ustin, S.L., Roberts, D.A., Gamon, J.A., Asner, G.P., Green, R.O., 2004. Using imaging spectroscopy to study ecosystem processes and properties. Bioscience 54, 523–534.

van Aardt, J.A.N., Wynne, R.H., 2007. Examining pine spectral separability using hyperspectral data from an airborne sensor: An extension of field-based results. Int. J. Remote Sens. 28, 431–436. doi:10.1080/01431160500444772

Van Den Berg, A.K., Perkins, T.D., 2005. Nondestructive estimation of anthocyanin content in autumn sugar maple leaves. Hortic. Sci. 40, 685–686.

Van Gunst, K.J., Weisberg, P.J., Yang, J., Fan, Y., 2016. Do denser forests have greater risk of tree mortality: A remote sensing analysis of density-dependent forest mortality. For. Ecol. Manage. 359, 19–32. doi:10.1016/j.foreco.2015.09.032

Van Mantgem, P.J., Stephenson, N.L., 2007. Apparent climatically induced increase of tree mortality rates in a temperate forest. Ecol. Lett. 10, 909–916. doi:10.1111/j.1461-0248.2007.01080.x

van Mantgem, P.J., Stephenson, N.L., Byrne, J.C., Daniels, L.D., Franklin, J.F., Fule, P.Z., Harmon, M.E., Larson, A.J., Smith, J.M., Taylor, A.H., Veblen, T.T., 2009. Widespread Increase of Tree Mortality Rates in the Western United States. Science (80-.). 323, 521–524. doi:10.1126/science.1165000

van Wagtendonk, J.W., Root, R.R., Key, C.H., 2004. Comparison of AVIRIS and Landsat ETM+ detection capabilities for burn severity. Remote Sens. Environ. 92, 397–408. doi:10.1016/j.rse.2003.12.015

Veganzones, M.A., Grana, M., 2008. Endmember Extraction Methods: A Short Review. Knowledge-Based Intell. Inf. Eng. Syst. 12th Int. Conf. KES 2008 400–407. doi:10.1007/978-3-540-85567-5_50

Veraverbeke, S., Hook, S., 2013. Evaluating spectral indices and spectral mixture analysis for assessing fire severity, combustion completeness and carbon emissions. Int. J. Wildl. Fire 22, 707–720.

Veraverbeke, S., Lhermitte, S., Verstraeten, W.W., Goossens, R., 2010. The temporal dimension of differenced Normalized Burn Ratio (dNBR) fire/burn severity studies: The case of the large 2007 Peloponnese wildfires in Greece. Remote Sens. Environ. 114, 2548–2563. doi:10.1016/j.rse.2010.05.029

Veraverbeke, S., Stavros, E.N., Hook, S.J., 2014. Remote Sensing of Environment

Assessing fire severity using imaging spectroscopy data from the Airborne Visible / Infrared Imaging Spectrometer (AVIRIS) and comparison with multispectral capabilities. Remote Sens. Environ. 154, 153–163. doi:10.1016/j.rse.2014.08.019

Vogelmann, J.E., 1990. Comparison between two vegetation indices for measuring different types of forest damage in the north-eastern United States. Int. J. Remote Sens. 11, 2281–2297. doi:10.1080/01431169008955175

Waring, K.M., Reboletti, D.M., Mork, L.A., Huang, C.-H., Hofstetter, R.W., Garcia, A.M., Fulé, P.Z., Davis, T.S., 2009. Modeling the Impacts of Two Bark Beetle Species Under a Warming Climate in the Southwestern USA: Ecological and Economic Consequences. Environ. Manage. 44, 824–835. doi:10.1007/s00267-009-9342-4

White, J.C., Coops, N.C., Hilker, T., Wulder, M.A., Carroll, A.L., 2007. Detecting mountain pine beetle red attack damage with EO-1 Hyperion moisture indices. Int. J. Remote Sens. 28, 2111–2121. doi:10.1080/01431160600944028

Williams, A.P., Allen, C.D., Macalady, A.K., Griffin, D., Woodhouse, C.A., Meko, D.M., Swetnam, T.W., Rauscher, S.A., Seager, R., Grissino-Mayer, H.D., Dean, J.S., Cook, E.R., Gangodagamage, C., Cai, M., Mcdowell, N.G., 2013. Temperature as a potent driver of regional forest drought stress and tree mortality. Nat. Clim. Chang. 3, 292–297. doi:10.1038/nclimate1693

Williams, a. P., Seager, R., Abatzoglou, J., Cook, B., Smerdon, J., Cook, E., 2015. Contribution of anthropogenic warming to California drought during 2012 – 2014. Geophys. Res. Lett. 42, 6819–6828. doi:10.1002/2015GL064924.Received

Wilson, E.H., Sader, S.A., 2002. Detection of forest harvest type using multiple dates of Landsat TM imagery. Remote Sens. Environ. 80, 385–396. doi:10.1016/S0034-4257(01)00318-2

Wulder, M.A., Dymond, C.C., White, J.C., Leckie, D.G., Carroll, A.L., 2006. Surveying mountain pine beetle damage of forests: A review of remote sensing opportunities. For. Ecol. Manage. 221, 27–41. doi:10.1016/j.foreco.2005.09.021

Young, D.J.N., Stevens, J.T., Earles, J.M., Moore, J., Ellis, A., Jirka, A.L., Latimer, A.M., 2017. Long-term climate and competition explain forest mortality patterns under extreme drought. Ecol. Lett. 20, 78–86. doi:10.1111/ele.12711

Youngentob, K.N., Roberts, D.A., Held, A.A., Dennison, P.E., Jia, X., Lindenmayer, D.B.,

2011. Mapping two Eucalyptus subgenera using multiple endmember spectral mixture analysis and continuum-removed imaging spectrometry data. Remote Sens. Environ. 115, 1115–1128. doi:10.1016/j.rse.2010.12.012

Zhao, C.H., Cui, S.L., Qi, B., 2014. A sparse multiple endmember spectral mixture analysis algorithm of hyperspectral image, in: International Conference on Signal Processing Proceedings, ICSP. pp. 687–692. doi:10.1109/ICOSP.2014.7015091

Zuur, A.F., Ieno, E.N., Elphick, C.S., 2010. A protocol for data exploration to avoid common statistical problems. Methods Ecol. Evol. 1, 3–14. doi:10.1111/j.2041-210X.2009.00001.x

Appendix 1: Index of Acronyms

ADS – Aerial Detection Surveys

AOP – Airborne Observation Platform

ASD – Analytic Spectral Devices

ATCOR – Atmospheric and Topographic Correction

ATREM – Atmospheric Removal Porgram

AVIRIS – Airborne Visible / Infrared Imaging Spectrometer

AVIRIS-NG – Airborne Visible / Infrared Imaging Spectrometer – Next Generation

BCAL – Boise Center Aerospace Laboratory

BRDF – Bi-directional Reflectance Distribution Function

CBI – Composite Burn Index

CoB – Count-based endmember class

CT – Classification Trees

CWC – Canopy Water Content

DCM – Digital Canopy Model

DEM – Digital Elevation Model

dGV – Differenced Green Vegetation

dNBR - Difference Normalized Burn Ratio

dSMA – Differenced Spectra Mixture Analysis

DOQQ – Digital Othophot Quarter Quad

EAR – Endmember Average Root Mean Squared Error

EnMAP – Environmental Mapping and Analysis Program

EMC – A endmember reduction technique combining EAR, MASA, and CoB

EVI – Enhanced Vegetation Index

FACTS – Forest Service Activity Tracking System

FOV – Field of View

GeoCBI – Geo Composite Burn Index

GPS – Geographic Positioning System

GV – Green Vegetation

HyspIRI – Hypserspectral Infrared Imager

IES - Iterative endmember Selection

JPL - Jet Propulsion Lab

MAD – Multivariate Alteration Detection

MASA – Minimum Average Spectral Angle

MDA – Mean Decrease in Accuracy

MESMA – Multiple Endmember Spectral Mixture Analysis

MLC - Maximum Likelihood Classification

MNF – Maximum Noise Fraction

NASA – National Aeronautics and Space Administration

NBR – Normalized Burn Ratio

NDVI – Normalized Difference Vegetation Index

NEON – National Ecological Observation Network

NIST – National Institute of Standard and Technology

NPV – Non-Photosynthetic Vegetation

OA - Overall Accuracy

OCA – Overall Count Accuracy

OLI – Operational Land Imager

OOB – Out-of-Bag

PA – Producer's Accuracy

PCA – Principal Component Analysis

PDF – Probability Density Function

POS – Positioning and Orientation System

PWS – Progressive Water Stress

PRISM – Parameter-elevation relationships on independent slopes model

PRISMA - PRecursore IperSpettrale della Missione Applicativa

RdNBR – Relative Difference Normalized Burn Ratio

RMSE – Root Mean Square Error

RF - Random Forest

SD – Standard Deviation

SI - Stability Index

SMA - Spectral Mixture Analysis

SSCZO – Southern Sierra Critical Zone

SZU – Stable Zone Unmixing

UA – User's Accuracy

USGS – United States Geological Survey

uSZU – uncorrelated Stable Zone Unmixing

VIF – Variance of Inflation Facto

VSWIR – Visible to Shortwave Infrared

Appendix 2: Common and Scientific Names of Life Forms

Genus Names

Bark beetles - *Dendroctonus spp.*

California lilac – *Ceanothus spp.*

Manzanita – *Arctostaphylos spp.*

Oak – *Quercus spp.*

Pines - *Pinus spp.*

Species Names

Blue Oak – *Quercus douglasii*

California black oak – *Quercus kelloggii*

California buckeye – *Aesculus Californica*

Canyon live oak – *Quercus chrysolepis*

Incense-cedar – *Calocedrus decurrens*

Interior live oak – *Quercus wislizeni*

Lodgepole pine – *Pinus contorta*

Ponderosa pine – *Pinus ponderosa*

Red fir – *Abies magnifica*

Sugar pine – *Pinus lambertiana*

Valley oak – *Quercus lobate*

White fir – *Abies concolor*

Appendix 3: Pre-processing of the Aerial Detection Survey Data

Digitized mortality polygons from the aerial detection surveys (ADS) were first accessed from a government data repository (https://www.fs.usda.gov/detail/r5/forest-grasslandhealth/?cid=fsbdev3_046696) and used in accordance with the United States Forest Service Aerial Survey Handbook (https://www.fs.fed.us/foresthealth/technology/pdfs/GISHandbook_body_apndxA-C.pdf). After accessing the data, we first filtered out polygons which ADS indicated were primarily associated with oaks by removing polygons with data in columns "FOR TYPE1" and "HOSTS1" (associated with the polygon's forest type and the primary host type, respectively) that indicated they were oak dominated. We did not remove the few polygons (less than 10) with values in "HOSTS2" or "HOSTS3" that indicated oaks were a secondary or tertiary impacted species with the polygon.

In order to display the estimated number of red stage trees per ha in each polygon in Figure 3.6 of the main text, we used the "TPA1" column. The trees per acre estimate calculated in the "TPA1" column is obtained by using the ADS estimated number of dead trees divided by the calculated area of the polygon after digitization. For our study, we manually convert trees per acre to tree per ha.

Appendix 4: Inputs into the Monte Carlo Simulation

The Monte Carlo simulation, as described in Section 4.2.4, relied on a variety of inputs. Although all inputs were derived from the results presented in Section 4.3.1, in this appendix we summarize the precise inputs used in the Monte Carlo simulation. In Table 4.2, step 1 references two inputs needed in order to estimate the total number of misclassified trees by species. The first input, the total number of tree object in each species class, as identified by the uncorrected spatial model, is shown in Table A4.1. The other major input, the mean and standard error probability of a tree classified as being any given species actually being any other given species (derived from Table 4.4 in the main text), is shown in Table A4.2.

Table A4.1. Number of crown objects in the study area by species as identified in Figure 4.5.

	Incense-cedar	Oak	Ponderosa pine	Sugar pine	White fir
Number of Tree Objects	8,719	62,312	61,954	1,018	1,751

Table A4.2. Probability of a tree belonging to any given reference species, being classified as any given class as determined from Table 4.3. Standard error values are given in parentheses.

Class Ref	Incense-cedar	Oak	Ponderosa pine	Sugar pine	White fir
Incense-cedar	0.73 (0.19)		0.02 (0.02)		0.06 (0.06)
Oak		0.97 (0.03)	0.09 (0.04)	0.07 (0.11)	
Ponderosa pine	0.27 (0.11)	0.03 (0.03)	0.89 (0.04)	0.27 (0.11)	0.06 (0.06)
Sugar pine				0.67 (0.12)	
White fir					0.88 (0.08)

In Table 4.2 step 2, which has the objective of reassigning tree species in the object database to correct for species classification error, is based on the output of step 1. The exact values for this output of step 1 will vary with each iteration of the Monte Carlo simulation; however, a sample output is given in Table A4.3. Another input are tree height histograms for each species, which are derived from the spatial model. Figure A4.1, a) – e) displays each species specific height histogram used as an input to the Monte Carlo simulation.

Table A4.3. One sample stochastic outcome of the Monte Carlo simulation estimating the number of misclassified trees by species and the actual class of tree.

Input Class Output Class	Incense-cedar	Oak	Ponderosa pine	Sugar pine	White fir
Incense-cedar	4701		3878		24
Oak		56858	5407	6	
Ponderosa pine	1475	510	59979	4	135
Sugar pine				1020	
White fir					1755

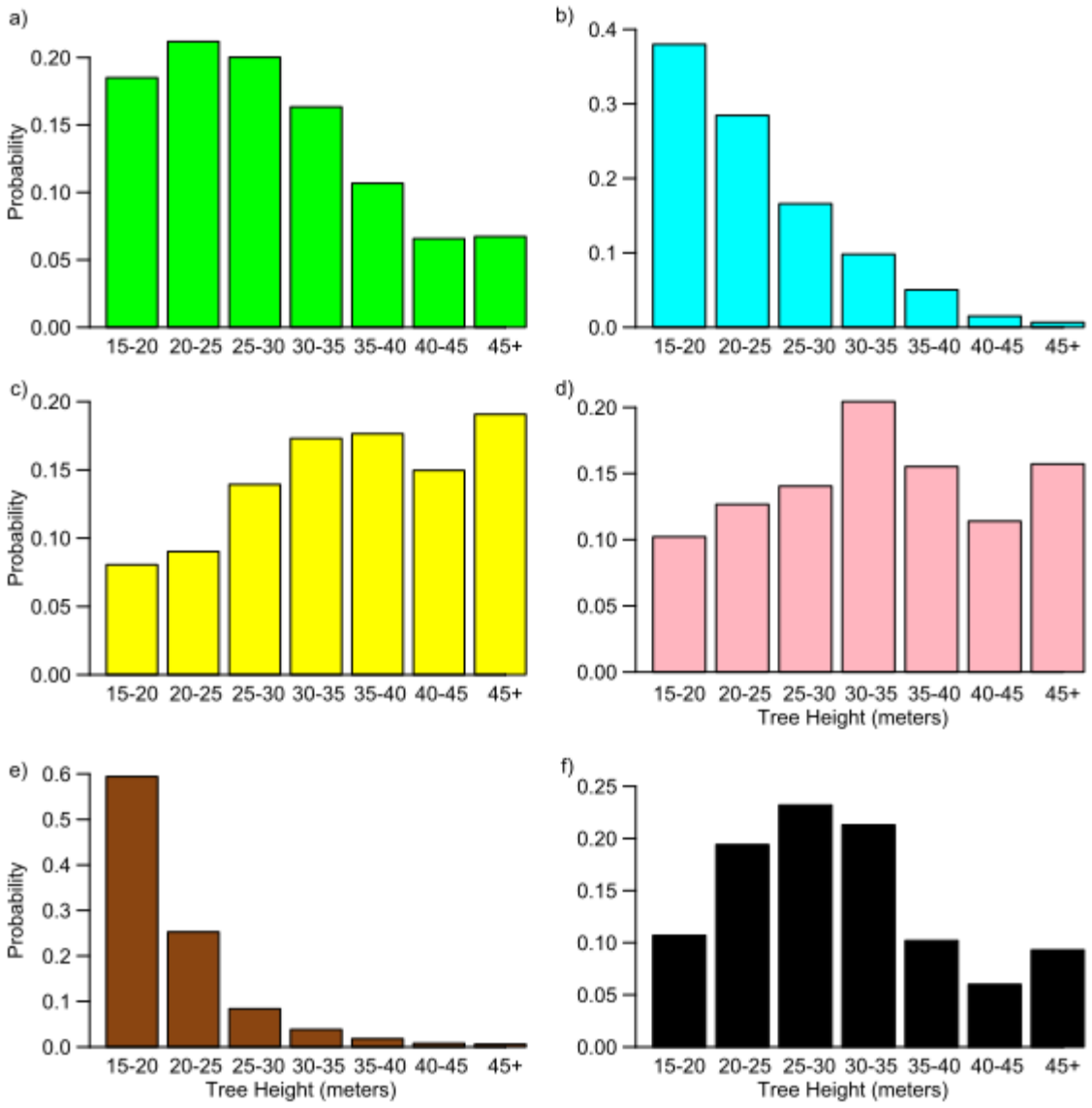

Figure A4.1. Histograms of the probability of a tree falling into one of seven height classes for a) ponderosa pine; b) incense-cedar; c) white fir; d) sugar pine; e) oak; and, f) trees missed by the crown object algorithm.

The goal of Table 4.2, step 3 is to update the crown object database to include the trees missed by the crown object identification algorithm. There were three inputs for this step. The first was the crown object database, after being stochastically updated to correct for species classification error in step 2. The second was a PDF that estimates the probably true OCA value, which is an estimate for the number of objects missed by the classification algorithm. The PDF was generated from a Gaussian distribution with parameters of a mean

of 1.093 and standard error of 0.013 (determined in Section 4.3.1.1 of the main text). The final input, a histogram of the distribution of the heights of missed crowns is shown in Figure A4.1, part f.

The final step of the Monte Carlo simulation requiring outside inputs, was, as outlined in Table 4.2, Step 4. The goal of this step was to make an initial estimate of the tree mortality rates by species and height class, which were corrected to account for species misclassification error in latter steps. The input for this step were pre-determined randomly selected tree crowns, each one of which had the crown's 2016 status manually identified. From this raw data, estimates of mean survival rate and standard error of survival rate were identified (Table A4.4), these values were used as parameters for a Gaussian distribution to create a PDF from which the Monte Carlo simulation drew values representing the estimates of the actual survival rate.

Table A4.4. Uncorrected by survival rates of trees between 2013 – 2016 by species and height class as generated from random sampling and manual classification of 2016 tree status.

Height Class	Incense-cedar	Oak	Ponderosa pine	Sugar pine	White fir
15 – 20 m	56% (4%)	85% (2%)	28% (2%)	19% (10%)	62% (13%)
20 – 25 m	64% (5%)	67% (4%)	22% (2%)	33% (10%)	50% (12%)
25 – 30 m	44% (6%)	44% (6%)	18% (2%)	42% (10%)	56% (10%)
30 – 35 m	46% (7%)	46% (8%)	15% (2%)	35% (8%)	48% (9%)
35 – 40 m	19% (6%)	19% (9%)	19% (3%)	54% (9%)	72% (8%)
40 – 45 m	18% (6%)	18% (12%)	20% (3%)	55% (12%)	64% (10%)
>45 m	20% (13%)	20% (18%)	22% (3%)	55% (8%)	77% (8%)

Appendix 5: Analysis of the Effects of Bias Corrections on the Monte Carlo Simulation

A5.1. Varied Assumptions and Simulations

A Monte Carlo simulation is used in the body of this chapter to correct for error, bias, and the potential for the propagation of error and bias from the various aspects of the spatially explicit crown model. Most of the corrections made by the Monte Carlo simulation are directly drawn from more accurate independent validation data. However, the model makes two adjustments beyond what could be directly drawn from independent validation data.

One of these assumptions relates to the conifer survival estimates made between 2013 and 2016 by species and height class. Since the species class used for these estimates are themselves determined by a species classification which has errors, these errors have the potential to bias the survival estimates. The Monte Carlo simulation used in the body of the chapter adjusts the original mortality rate for each species and height class. This was done by using the species and height class combination's estimated species misclassification rate combined with the estimated mortality rates of the other misclassified species. In this section, this will be referred to as assumption 1.

Another assumption made relates to the height distribution of the misclassified species. Although the independent validation data for the species classification gives insight into the overall error rate of the species classification by species, it does not give robust information with regards to the height of the misclassified trees. The Monte Carlo simulation used in the body of the chapter assumes that misclassified trees species distribution is similar to the

species distribution of their ‘true’ class. In this section, this will be referred to as assumption 2.

We test the strength of these assumptions by running Monte Carlo simulations which make different assumptions for these problems. For assumption 1, an altered Monte Carlo simulation is run that assumes that species misclassification does not bias survival rate by using the unadjusted 2013 – 2016 conifer survival rate by species and height class. For assumption 2, an altered Monte Carlos simulation is run that assumes that misclassified species have the same height distribution as the species they were incorrectly classified as. This Monte Carlo simulation therefore randomly picks trees from each species to be labeled as misclassified with no attention paid to tree height.

We analyze the results from four separate Monte Carlo simulations in this section: simulation 1 is the Monte Carlo simulation presented in Chapter 4; Simulation 2 uses altered assumption 1, as described in the previous paragraph, Simulation 3 uses altered assumption 2, as described in the previous paragraph; Simulation 4 uses both altered assumption 1 and altered assumption 2.

A5.2. Simulation Comparison

When comparing the mean and standard deviation of the Monte Carlo simulation results (Table A5.1 and Table A5.2, respectively), it is clear that both assumptions have major impacts on the simulation outcomes. Since ponderosa pine and incense-cedar are the two most common conifers on the landscape and misclassification of incense-cedars as ponderosa pine was found to be relatively common in the independent validation data (Table 4.3), the largest impact of the varying assumptions is on these two species of conifers. The height distribution of ponderosa pine and incense-cedar is quite different, which compounds

the effects of assumptions 1 and 2. Simulation 2 deviates from simulation 1 only in the way it estimates the mortality occurring by species and height class. Differences between simulation 1 and 2 seem to be greatest for the smallest height class trees and particularly impactful on ponderosa pine, with the effect generally being an increase in the number of living trees in 2016 for ponderosa pine and decreases of living trees for incense-cedar. Differences between simulation 1 and simulation 2 become minimal for trees above 35 m tall.

Simulation 3 varies from simulation 1 in the way that trees are selected to be identified as misclassified. The overall effect was to increase the number of small ponderosa pine and decrease the number of large ponderosa pine while having the opposite effect for incense-cedar. Even when only comparing the 2016 species and height class abundances simulation 3 appears to deviate from simulation 1 more strongly than simulation 2. For the less common species of white fir and sugar pine, varying the assumptions makes a substantial difference relative to the 2013 and 2016 estimated abundance of the species and height class, however, from the perspective of total conifer abundance across the study area the difference is minimal.

Table A5.1. Mean number of trees modeled in 2013 and 2016 by 1,000 iterations of four different version of Monte Carlo simulations by species and height class.

		Simulation #	15 – 20	20 - 25	25 -30	30 – 35	35 – 40	40 -45	45+
Ponderosa pine	**2013**	1	10845	13459	13185	10886	7183	4404	4415
		2	11303	14493	14531	12141	7782	4772	4977
		3	12679	13913	13013	10673	6717	4097	4374
		4	12722	13929	13014	10670	6722	4100	4353
	2016	1	2075	2473	2224	1536	1250	816	928
		2	3114	3197	2676	1906	1464	935	1090
		3	2738	2355	1946	1209	1165	740	910
		4	3519	3075	2392	1676	1262	801	960
Incense-cedar	**2013**	1	3817	2766	1505	810	340	62	17
		2	4016	2995	1668	909	368	67	19
		3	2937	2384	1550	1007	543	221	172
		4	2923	2370	1538	999	539	218	170
	2016	1	2219	1951	994	745	324	61	17
		2	2249	1948	963	721	309	59	17
		3	1889	1853	1069	939	523	215	160
		4	1640	1550	888	794	451	192	145
White fir	**2013**	1	161	181	280	354	368	297	364
		2	169	195	309	395	399	321	411
		3	126	147	233	294	291	246	327
		4	127	147	234	295	291	247	327
	2016	1	98	89	157	173	264	188	284
		2	105	97	172	192	285	205	320
		3	82	75	138	143	219	161	268
		4	77	73	132	144	210	158	255
Sugar pine	**2013**	1	140	173	193	283	215	155	209
		2	147	187	213	317	235	169	236
		3	71	91	104	154	113	83	119
		4	71	91	105	154	113	83	119
	2016	1	27	58	81	100	118	85	115
		2	27	62	88	114	130	93	130
		3	16	32	53	64	83	60	86
		4	14	31	43	54	61	45	66

Table A5.2. Standard deviation of the number of trees modeled in 2013 and 2016 by 1,000 iterations of four different version of Monte Carlo simulations by species and height class.

		Simulation #	15 – 20	20 - 25	25 -30	30 – 35	35 – 40	40 -45	45+
Ponderosa pine	**2013**	1	977	696	542	485	335	148	95
		2	1015	752	616	550	374	187	177
		3	1001	763	637	515	317	204	233
		4	1022	760	623	504	319	199	219
	2016	1	768	429	283	225	199	140	140
		2	384	339	298	239	210	152	158
		3	601	514	397	337	224	160	181
		4	420	318	262	211	182	127	140
Incense-cedar	**2013**	1	402	341	253	211	156	46	13
		2	413	365	277	232	170	50	14
		3	423	375	285	210	125	69	72
		4	429	377	283	208	124	68	70
	2016	1	270	230	146	172	142	45	12
		2	294	279	198	196	144	44	13
		3	224	230	176	181	113	66	67
		4	271	274	183	177	107	61	64
White fir	**2013**	1	11	12	19	35	39	25	21
		2	11	14	22	40	43	28	26
		3	12	14	21	27	26	22	31
		4	11	13	21	26	26	23	30
	2016	1	23	22	29	37	40	34	33
		2	24	24	32	39	44	38	39
		3	20	22	28	33	31	32	36
		4	18	19	25	27	29	29	36
Sugar pine	**2013**	1	14	17	19	30	24	17	21
		2	15	19	22	34	28	20	24
		3	15	19	21	31	23	17	25
		4	15	19	22	31	23	17	24
	2016	1	14	18	21	24	24	19	18
		2	15	21	24	29	26	22	23
		3	13	15	17	19	16	14	16
		4	8	12	14	17	16	13	17

Appendix 6: Variables Included and Eliminated from Chapter 5 Analysis

Table A6.1. Variables initially considered for the analysis at the entire southern Sierra Nevada scale. Variables that after the variance of inflation (VIF) based reduction were included in either the individual data categories or the combined categories data were marked with a "Y", if the cell was left blank it was not included. "Removed" indicates the variable was removed from analysis before variable reduction.

Name	Selected within category	Selected in combined categories
Biotic - fire		
Time since last fire	Y	Y
Time since second to last fire	Removed	Removed
Time since third to last fire	Removed	Removed
Biotic - PWS		
Progressive water stress	Y	Y
Vulnerability score	Y	Y
Biotic - VIs		
Spring 2013 ACI		
Spring 2013 ARI		
Spring 2013 CAI	Y	Y
Spring 2013 CARI		
Spring 2013 CI		
Spring 2013 CRI1	Y	
Spring 2013 CRI2		
Spring 2013 EVI		
Spring 2013 mARI		
Spring 2013 MCARI		
Spring 2013 MSI		
Spring 2013 NDII		
Spring 2013 NDLI		
Spring 2013 NDNI		
Spring 2013 NDVI		
Spring 2013 NDWI		
Spring 2013 PRI		
Spring 2013 PSND		
Spring 2013 PSRI		
Spring 2013 PSSR		
Spring 2013 RGRI		
Spring 2013 RVSI		
Spring 2013 SIPI		
Spring 2013 SR		
Spring 2013 VARI		
Spring 2013 VIgreen		
Spring 2013 WBI		
Summer 2013 ACI		
Summer 2013 ARI		
Summer 2013 CAI	Y	Y
Summer 2013 CARI		

Summer 2013 CI		
Summer 2013 CRI1		
Summer 2013 CRI2		
Summer 2013 EVI		
Summer 2013 mARI		
Summer 2013 MCARI		
Summer 2013 MSI		
Summer 2013 NDII		
Summer 2013 NDLI		
Summer 2013 NDNI		
Summer 2013 NDVI		
Summer 2013 NDWI		
Summer 2013 PRI		
Summer 2013 PSND		
Summer 2013 PSRI		
Summer 2013 PSSR		
Summer 2013 RGRI		
Summer 2013 RVSI	Y	Y
Summer 2013 SIPI		
Summer 2013 SR		
Summer 2013 VARI		
Summer 2013 VIgreen		
Summer 2013 WBI		
Summer 2014 ACI		
Summer 2014 ARI		
Summer 2014 CAI	Y	Y
Summer 2014 CARI		
Summer 2014 CI		
Summer 2014 CRI1	Y	Y
Summer 2014 CRI2		
Summer 2014 EVI		
Summer 2014 mARI		
Summer 2014 MCARI		
Summer 2014 MSI		
Summer 2014 NDII		
Summer 2014 NDLI		
Summer 2014 NDNI		
Summer 2014 NDVI		
Summer 2014 NDWI		
Summer 2014 PRI		
Summer 2014 PSND		
Summer 2014 PSRI		
Summer 2014 PSSR		
Summer 2014 RGRI		
Summer 2014 RVSI		
Summer 2014 SIPI		
Summer 2014 SR		
Summer 2014 VARI		
Summer 2014 VIgreen		
Summer 2014 WBI	Y	

Fall 2014 ACI		
Fall 2014 ARI		
Fall 2014 CAI		
Fall 2014 CARI		
Fall 2014 CI		
Fall 2014 CRI1	Y	Y
Fall 2014 CRI2		
Fall 2014 EVI		
Fall 2014 mARI		
Fall 2014 MCARI		
Fall 2014 MSI		
Fall 2014 NDII		
Fall 2014 NDLI		
Fall 2014 NDNI		
Fall 2014 NDVI		
Fall 2014 NDWI		
Fall 2014 PRI		
Fall 2014 PSND		
Fall 2014 PSRI		
Fall 2014 PSSR		
Fall 2014 RGRI		
Fall 2014 RVSI		
Fall 2014 SIPI		
Fall 2014 SR		
Fall 2014 VARI		
Fall 2014 VIgreen		
Fall 2014 WBI	Y	
Spring 2015 ACI		
Spring 2015 ARI		
Spring 2015 CAI		
Spring 2015 CARI		
Spring 2015 CI		
Spring 2015 CRI1	Y	
Spring 2015 CRI2		
Spring 2015 EVI		
Spring 2015 mARI		
Spring 2015 MCARI		
Spring 2015 MSI		
Spring 2015 NDII		
Spring 2015 NDLI		
Spring 2015 NDNI		
Spring 2015 NDVI		
Spring 2015 NDWI		
Spring 2015 PRI		
Spring 2015 PSND		
Spring 2015 PSRI		
Spring 2015 PSSR		
Spring 2015 RGRI		
Spring 2015 RVSI		
Spring 2015 SIPI		

Spring 2015 SR		
Spring 2015 VARI		
Spring 2015 VIgreen		
Spring 2015 WBI		
Summer 2015 ACI		
Summer 2015 ARI		
Summer 2015 CAI		
Summer 2015 CARI		
Summer 2015 CI		
Summer 2015 CRI1		
Summer 2015 CRI2		
Summer 2015 EVI	Y	Y
Summer 2015 mARI		
Summer 2015 MCARI		
Summer 2015 MSI		
Summer 2015 NDII		
Summer 2015 NDLI		
Summer 2015 NDNI		
Summer 2015 NDVI		
Summer 2015 NDWI		
Summer 2015 PRI		
Summer 2015 PSND		
Summer 2015 PSRI		
Summer 2015 PSSR		
Summer 2015 RGRI		
Summer 2015 RVSI		
Summer 2015 SIPI		
Summer 2015 SR		
Summer 2015 VARI		
Summer 2015 VIgreen		
Summer 2015 WBI		
Climatic		
Spring 2013 precipitation		
Fall 2013 precipitation		
Winter 2013 precipitation		
Water year 2013 precipitation		
Spring 2014 precipitation		
Fall 2014 precipitation		
Winter 2014 precipitation		
Water year 2014 precipitation		
Spring 2015 precipitation		
Winter 2015 precipitation		
Water year 2015 precipitation		
Cumulative 3-year precipitation	Y	Y
Spring 2013 temperature		
Summer 2013 temperature		

Fall 2013 temperature		
Winter 2013 temperature		
2013 temperature		
Spring 2014 temperature		
Summer 2014 temperature		
Fall 2014 temperature		
Winter 2014 temperature		
2014 temperature		
Spring 2015 temperature		
Summer 2015 temperature		
Winter 2015 temperature		
2015 temperature		
Cumulative 3-year deviation from average	Y	Y
Contagion		
Distance from 1 tree	Y	Y
Distance from 3 tree	Y	
Distance from 10 tree	Y	Y
Topographic		
Aspect	Y	Y
Elevation	Y	Y
Slope		
Solar Insolation		
Topographic Wetness Index	Y	Y

Table A6.2. Variables initially considered for the analysis at the Soaproot Saddle scale. Variables combinations explored were the individual data categories (Category), the analysis of all the canopy variables of varying buffer sizes (Canopy all), all the variables together (All), or the biotic canopy variables at 45 m combined with the contagion, individual, and topographic variables (All C45). Variables included in the category after VIF analysis were marked with a "Y", if the cell was left blank it was not included.

Name	Category	Canopy all	All	All C45
Biotic – canopy – 10 m				
Canopy density – 10 m				
Kurtosis – 10 m	Y	Y	Y	
Max height – 10 m	Y	Y		
Mean 5th percentile height – 10 m				
Mean 95th percentile height – 10 m				
Mean height – 10 m				
Median maximum height ratio – 10 m				
Min height – 10 m	Y	Y	Y	
25th quantile height – 10 m				
50th quantile height – 10 m				
75th quantile height – 10 m				
90th quantile height – 10 m				
95th quantile height – 10 m				
Rumble index – 10 m				
Surface area – 10 m				
Skewness – 10 m				
Standard deviation of height – 10 m				
Dead trees – 10 m	Y	Y	Y	
Hardwoods – 10 m	Y	Y	Y	
Incense-cedar – 10 m	Y	Y	Y	
Low canopy – 10 m				
Ponderosa pine – 10 m				
Sugar pine – 10 m	Y	Y	Y	
White fir – 10 m	Y	Y	Y	
Biotic – canopy – 20 m				
Canopy density – 20 m				
Kurtosis – 20 m	Y	Y	Y	
Max height – 20 m	Y			
Mean 5th percentile height – 20 m	Y			
Mean 95th percentile height – 20 m				
Mean height – 20 m				
Median maximum height ratio – 20 m				
Min height – 20 m	Y	Y		
25th quantile height – 20 m				
50th quantile height – 20 m				
75th quantile height – 20 m				
90th quantile height – 20 m				
95th quantile height – 20 m				
Rumble index – 20 m				
Surface area – 20 m				
Skewness – 20 m				
Standard deviation of height – 20 m				
Dead trees – 20 m	Y			

Hardwoods – 20 m	Y			
Incense-cedar – 20 m	Y			
Low canopy – 20 m				
Ponderosa pine – 20 m				
Sugar pine – 20 m	Y	Y	Y	
White fir – 20 m	Y			
Biotic – canopy – 30 m				
Canopy density – 30 m				
Kurtosis – 30 m	Y			
Max height – 30 m	Y			
Mean 5th percentile height – 30 m				
Mean 95th percentile height – 30 m				
Mean height – 30 m				
Median maximum height ratio – 30 m				
Min height – 30 m	Y			
25th quantile height – 30 m				
50th quantile height – 30 m				
75th quantile height – 30 m				
90th quantile height – 30 m				
95th quantile height – 30 m				
Rumble index – 30 m				
Surface area – 30 m				
Skewness – 30 m				
Standard deviation of height – 30 m				
Dead trees – 30 m	Y	Y	Y	
Hardwoods – 30 m	Y			
Incense-cedar – 30 m	Y			
Low canopy – 30 m				
Ponderosa pine – 30 m				
Sugar pine – 30 m	Y			
White fir – 30 m	Y			
Biotic – canopy – 45 m				
Canopy density – 45 m				
Kurtosis – 45 m	Y			Y
Max height – 45 m	Y			Y
Mean 5th percentile height – 45 m	Y	Y		Y
Mean 95th percentile height – 45 m				
Mean height – 45 m				
Median maximum height ratio – 45 m				
Min height – 45 m	Y			Y
25th quantile height – 45 m				
50th quantile height – 45 m				
75th quantile height – 45 m				
90th quantile height – 45 m				
95th quantile height – 45 m				
Rumble index – 45 m				
Surface area – 45 m				
Skewness – 45 m				
Standard deviation of height – 45 m				
Dead trees – 45 m	Y			Y

Hardwoods – 45 m	Y			Y
Incense-cedar – 45 m	Y			Y
Low canopy – 45 m				
Ponderosa pine – 45 m				
Sugar pine – 45 m				
White fir – 45 m	Y			Y
Biotic – canopy – 60 m				
Canopy density – 60 m				
Kurtosis – 60 m	Y	Y		
Max height – 60 m	Y			
Mean 5th percentile height – 60 m				
Mean 95th percentile height – 60 m				
Mean height – 60 m				
Median maximum height ratio – 60 m				
Min height – 60 m	Y	Y	Y	
25th quantile height – 60 m				
50th quantile height – 60 m				
75th quantile height – 60 m				
90th quantile height – 60 m				
95th quantile height – 60 m				
Rumble index – 60 m				
Surface area – 60 m				
Skewness – 60 m				
Standard deviation of height – 60 m				
Dead trees – 60 m	Y			
Hardwoods – 60 m	Y	Y	Y	
Incense-cedar – 60 m	Y			
Low canopy – 60 m				
Ponderosa pine – 60 m				
Sugar pine – 60 m	Y	Y	Y	
White fir – 60 m	Y			
Biotic – canopy – 100 m				
Canopy density – 100 m				
Kurtosis – 100 m				
Max height – 100 m	Y		Y	
Mean 5th percentile height – 100 m	Y	Y	Y	
Mean 95th percentile height – 100 m				
Mean height – 100 m				
Median maximum height ratio – 100 m				
Min height – 100 m	Y	Y	Y	
25th quantile height – 100 m	Y		Y	
50th quantile height – 100 m				
75th quantile height – 100 m				
90th quantile height – 100 m				
95th quantile height – 100 m				
Rumble index – 100 m				
Surface area – 100 m				
Skewness – 100 m				
Standard deviation of height – 100 m				
Dead trees – 100 m	Y	Y	Y	

Hardwoods – 100 m				
Incense-cedar – 100 m	Y	Y	Y	
Low canopy – 100 m				
Ponderosa pine – 100 m	Y			
Sugar pine – 100 m	Y			
White fir – 100 m	Y	Y	Y	
Contagion				
Distance from 1 tree				
Distance from 3 tree				
Distance from 10 tree	Y		Y	Y
Individual tree				
Crown size	Y		Y	Y
Height				
ACI				
ARI	Y		Y	Y
CAI				
CARI				
CI				
CRI1				
CRI2				
EVI	Y		Y	Y
mARI				
MCARI				
MSI				
NDII				
NDLI				
NDNI				
NDVI				
NDWI	Y		Y	Y
PRI				
PSND				
PSRI				
PSSR				
RGRI				
RVSI				
SIPI	Y		Y	Y
SR				
VARI				
VIgreen				
WBI	Y		Y	
Topographic				
Aspect	Y		Y	Y
Elevation	Y		Y	Y
Slope	Y		Y	Y
Solar Insolation	Y		Y	Y
Topographic Wetness Index 10 m	Y		Y	Y